MULTI GIGAHERTZ InGaAs/InP INVERTED MSM PHOTODETECTORS FOR PHOTORECEIVER AND WAVEGUIDE APPLICATIONS

Ph.D. Thesis

by

ZHAORAN HUANG

Thesis Advisor: Dr. Nan M. Jokerst

Submitted to Ph.D. Thesis Examination Committee
in Partial Fulfillment of the Requirement for the Degree of
Doctor of Philosophy in Electrical Engineering

School of Electrical and Computer Engineering
Georgia Institute of Technology
Atlanta, GA 30332

November 15, 2003

Multi Gigahertz InGaAs/InP Inverted MSM Photodetectors for Photoreceiver and Waveguide Applications

Approved by:

Dr. Nan M. Jokerst, Advisor

Dr. Phillip Allen

Dr. Gary May

Dr. Ian Ferguson

Dr. C. P. Wong

Date Approved: Nov. 17, 2003

Dedicated to my grandmother
Suping Li,

And in memory of my grandfather
Zhixue Sun.

ACKNOWLEDGEMENTS

I would like to thank my thesis advisor Dr. Nan M. Jokerst for her visionary guidance and constant encouragement throughout my years here. I wouldn't have had a chance to finish this work without her continuous support and endless patience. I would also like to thank my group members, Dr. Martin Brooke's team, Tomas Sarmiento, and Dr. Gary May for the collaborative work and many useful technical discussions in these years. I would like to particularly express my appreciation to Mike Vrazel and J.J. Shen for their train in the cleanroom and their detailed guidance which enabled me to work independently.

This is also a moment to express my love and gratitude to my family: my grandparents, ZhiXue Sun and SuPing Li, my parents, PengCheng Huang and HuiMing Sun, my sisters, ZhaoJie Huang and Yu Sun, and my husband, Kang Chen. Their love, support and encouragement are guides through those difficult days and made my Ph.D. work possible.

TABLE OF CONTENTS

LIST OF TABLES

LIST OF FIGURES

SUMMARY

In this work, the fabrication and integration process for both on-wafer metal-semiconductor-metal (MSM) PDs and thin film inverted MSM (I-MSM) PDs is discussed in detail. Both on-wafer MSM PDs and I-MSM PDs were investigated for the dark current, responsivity, impulse response, bandwidth, and capacitance variation as a function of varying finger width, spacing, active area size, and absorbing layer thickness. The responsivity, bandwidth, and capacitance of on-wafer MSM PDs were statistically modeled using a DOE matrix. The DOE modeling revealed that the finger width, active area size, and material thickness are not critical factors defining the bandwidth. However, the capacitance is sensitive to the active area of the MSM PDs. The I-MSM PDs were studied for the correlation to on-wafer MSM PDs for responsivity and impulse response. It shows that the MSM PDs fabricated in this work with typical structures are transit time limited, so the devices with 1 μm finger spacing have the best AC performance.

The thin film I-MSM PDs were integrated into photoreceiver and waveguide optical links. The photoreceiver integrated with I-MSM PDs demonstrated a bandwidth of 400 MHz with large size detectors, 200 μm × 200 μm square. An I-MSM PD with a 40 μm diameter was integrated onto a 10 Gbps CMOS chip and is under test. An optical link with an embedded thin film I-MSM PD in a channel waveguide showed a good eye diagram at 1 Gpbs on both Si/SiO_2 and ceramic substrates. Rectangular I-MSM PDs were also optimized and integrated onto ceramic substrates for an optical link at 10 Gbps.

CHAPTER 1

INTRODUCTION AND BACKGROUND

1.1 Motivation

The rapid growth of semiconductor technology has pushed electrical connections to their limits. The SIA Roadmap predicts that the speed and performance of electronic systems will ultimately be limited by the cost and performance of the interconnections[1]. Optoelectronic (OE) interfaces (such as photoreceivers and optical links with waveguides) are a possible solution to these foreseen electrical interconnection limitations.

Photodetectors are an essential component in optical communication for conversion of optical signals to electrical signals to be amplified by receiver circuits. Photodetector are being driven toward more and more stringent requirements with continued decreases in capacitance, increases in bandwidth, and larger size due to pressure from packaging. Photoreceivers integrated with MSM PDs have attracted attention from industry in recent years. The simple fabrication, lower capacitance than p-i-n photodiodes per unit area, and high alignment tolerance[2] may make the MSM photoreceiver more competitive as bandwidths rise, in contrast to the p-i-n photoreceivers, which are currently dominant in the market. Aphs GmbH® has reported InGaAs MSM PDs with FWHM of 18 ps, corresponding to a multi gigahertz bandwidth. OptoLynx® has a large area (80 μm diameter) GaAs MSM PD with a bandwidth of 5 GHz. However, the development of low cost, high speed, and reliable OE interconnections is still a limitation in many commercial applications, such as I/O interfaces to high density interconnection (HDI) substrates and fiber-to-the-home (FTTH). In this research, MSM PDs, separately

grown and independently optimized, are bonded to Si CMOS VLSI receiver circuitry, which is designed by Professor Martin Brooke's group (of Georgia Tech), to address these on-chip issues.

The electrical interconnection limitation predicted by the SIA Roadmap also finds possible solutions by using ultra short haul optical interconnect in the millimeter to centimeter range. These optical interconnections can offer benefits such as simplification of design, advantages in architecture, removal of timing skew, reduction of power dissipation, and voltage isolation [3].

In recent years, research into optical interconnections has begun to explore polymer waveguides deposited onto PDs for signal transport. Examples include a GaAs substrate using GaAs MSM PDs with polymer waveguides [4] and a Si substrate using Si PDs with polymer waveguides [5, 6]. To efficiently detect wavelengths of 1.3 μm to 1.55 μm, InGaAs PDs are necessary to integrate into polymer waveguide systems because Si PDs and GaAs PDs have very low quantum efficiency in this wavelength range. In this research, thin film InGaAs MSM PDs were separately grown, fabricated, and bonded to SiO_2-coated Si (Si/SiO_2) or ceramic interconnection substrates. Then, through collaboration with Kyocera, polymer waveguides were spin-coated and defined on top of the PDs to create channel waveguides for optical interconnection on the host substrate.

1.2 MSM PDs in Comparison to Other Types of PDs

As only one part of the whole optoelectronic receiver system, photodetectors must be compatible with the design of the rest of the system. This compatibility requires that the photodetector should have small capacitance, high bandwidth, high responsivity, and

low dark current. Among all the photodiodes, p-i-n photodiodes, Schottky barrier photodiodes, MSM photodetectors, and avalanche photodiodes are commonly designed and used for different applications. They are in general broadly classified as those without internal gain (p-i-n, MSM PDs, Schottky PDs) and those with gain (avalanche photodiodes).

In today's long distance, high-speed fiber optic communication, avalanche photodiodes (APDs) take advantage of an internal gain mechanism [7]. In an APD, a high electric field is established within the depletion region where impact ionization takes place, and this phenomenon leads to avalanche breakdown, which gives rise to the internal gain. This internal gain mechanism makes APDs a good candidate for long distance fiber transmission since every photon counts. However, impact ionization also gives the APDs the main drawback of additional noise due to the random nature of the gain mechanism. Another drawback which limites the use of APDs is the high cost, so that in applications of short to medium range, photodetectors without internal gain are usually used.

Photodetectors without gain can be divided into two classes: detectors with ohmic contacts and detectors with Schottky contacts. Among the detectors with ohmic contacts, p-i-n photodiodes are the most popular ones for use in fiber communication. The basic p-i-n photodiodes consists of three regions: the highly doped p-region, the intrinsic region and the highly doped n-region. In normal operation, the diodes are sufficiently reverse biased to cause the depletion region to punch through from the p-region to the n-region. Under illumination, the photocarriers are generated in this depletion region and collected at the corresponding electrical contacts. The speed of the response of the p-i-n photodiode

depends both on the circuit RC time constant and the intrinsic transit time. To reduce the capacitance of the photodiode, the active area size of the diode can be reduced without an impact on the quantum efficiency.

The advantages of p-i-n photodiodes include easy design of high quantum efficiency devices with high bandwidth, high reliability, and low noise. However, the high bandwidth is based on reducing the aperture dimensions of the diode for smaller capacitance, and this causes more difficult fiber alignment. To reduce the assembly cost, alternative designs of photodetectors with larger sizes are required.

Metal-semiconductor-metal (MSM) photodetectors have a much lower capacitance per unit area than p-i-n photodiodes, and thus offer a design alternative for high speed photodetectors. A MSM photodetector is composed of two back-to-back Schottky diodes and has interdigitated electrodes on the surface of the device, as shown in Figure 1. When a bias voltage is applied to the interdigitated electrodes, a depletion region extends into the semiconductor material. Under top illumination, photoexcited carriers are generated and accelerated in opposite directions by the internal electric field, as shown in Figure 2. These photogenerated electron-hole pairs (EHPs) are swept out by the electric field, and are then collected by the anode and cathode, respectively. How fast these carriers flow, and how many of them are collected by the electrodes per unit time, determine the speed and responsivity of the MSM PD. Therefore the transit time is related to the spacing between the interdigitated electrodes. The bandwidth of a PD is determined by the external RC time constant and by the intrinsic transit time, and can be expressed as:

$$f = \frac{1}{2\pi\sqrt{(RC)^2 + \tau_w^2}}, \tag{1.1}$$

where f is the bandwidth of a MSM PD, τ_{tr} is the transit time of the photogenerated carriers, and R and C are the resistance and capacitance of the MSM PD, respectively.

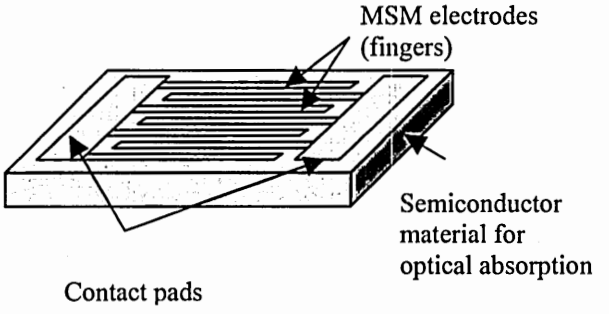

Figure 1: Basic structure of a MSM PD on semiconductor material.

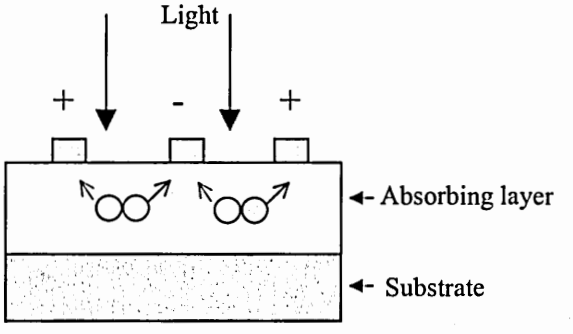

Figure 2: Photogenerated electron and hole pairs are in an electric field.

1.3 Fundamentals of MSM Physics

1.3.1 MSM Physics for DC Characteristics

Metals deposited onto semiconductors can form Schottky barriers. An energy band diagram of an MSM PD under bias and illumination is shown in Figure 3. The basic transport processes without illumination include (1) transport of electrons that have sufficient energy to overcome the potential barrier (thermionic emission); (2) tunneling of thermally activated carriers through the barrier (thermionic field-emission); (3)

generation of carriers from surface states[8]. Current generated without illumination is called dark current. To reduce dark current, a thin layer of lattice matched InAlAs (cap layer) is grown at the top of the PD structure to enhance the Schottky barrier height [9]. For a typical MSM (40 μm to 200 μm in diameter), the dark current is in the range from less than one nanoampere to tens of nanoamperes.

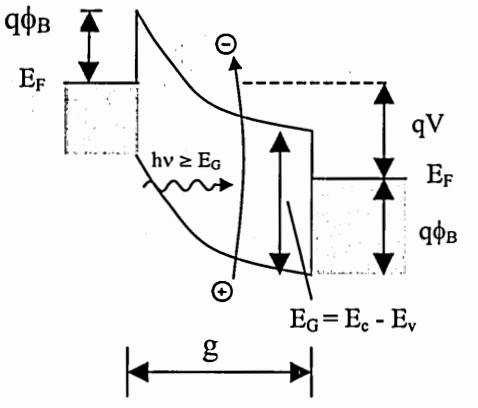

Figure 3: Energy band diagram of a MSM PD under bias and illumination.

Photocurrent is generated from the absorption of incident light having higher photon energy than the material bandgap. The cut-off wavelength for $In_{0.53}Ga_{0.47}As$ can be expressed as:

$$\lambda = \frac{hc}{Eg} = \frac{1.24\mu m.eV}{0.74eV} = 1.675\mu m \tag{1.2}$$

where h is Planck's constant, c is the speed of light, and E_g is the material bandgap.

The responsivity of PDs is defined as the ratio of photogenerated current to the incident light power at one wavelength:

$$R = \frac{Iph}{Popt} = \frac{q\eta}{h\nu} = \frac{\lambda\eta}{1.24\times10^{-6}}, \tag{1.3}$$

where η is the quantum efficiency of the device. The quantum efficiency for an MSM diode is expressed as:

$$\eta = \eta_i(1-r)(\frac{g}{g+w})(1-e^{-\alpha T}), \tag{1.4}$$

where η_i is the internal quantum efficiency, r is the reflection coefficient at the air-semiconductor interface, g is the finger gap, w is the finger width of the MSM PD, T is the thickness of the absorbing layer, and α is the absorption coefficient of the absorbing layer material ($In_{0.53}Ga_{0.47}As$). The absorption coefficient α is defined as:

$$\alpha = 4\pi k / \lambda, \tag{1.5}$$

where k is the extinction coefficient. The extinction coefficient of $In_{0.53}Ga_{0.47}As$ is approximately 0.25 in the wavelength range from 1.3 μm to 1.55 μm [10]. The incident illumination decays exponentially according to $e^{-\alpha x}$, where x is the distance measured from the surface of illumination. Thus, the penetration depth (d), where the energy of the incident light power has attenuated to e^{-1} is calculated as:

$$d = \frac{\lambda}{4\pi k} = \frac{1.3\mu m}{4\pi \times 0.25} = 0.4140\mu m = 414nm. \tag{1.6}$$

For a small bias voltage applied to the contacts, the electric fields and energy band profiles are shown in Figure 4 (a) and (b). In this figure, contact 1 of the MSM PD is biased at a negative voltage with respect to contact 2. Thus, contact 1 is reverse-biased (cathode), whereas contact 2 is forward-biased (anode). By increasing the voltage, the depleted area at the reverse biased cathode grows, while the depleted region is reduced at the forward biased anode [11]. A fully depleted area forms between the cathode and anode when the two areas touch. This condition is defined as the reach-through condition, and the bias voltage at this level is called the reach-through voltage V_{RT}. MSM PDs usually

are operated with a minimum DC bias at V_{RT}. Figure 4 (c) and (d) show the electric field and energy band diagram for the reach-through condition. With a further increase of bias voltage, the cathode depletion region extends more towards the anode, and the electric field reaches zero at the anode. This voltage is termed as the flat-band voltage V_{FB}. For voltage biases higher than V_{FB}, but before breakdown, the photocurrent remains constant. Photocarriers generated between the electrodes are swept by the electric field with the drift velocity in the transport region. Holes have a much slower drift velocity than electrons, so they have to travel a longer time to be collected by the cathode, which results in a long tail in the impulse response. Photocarriers generated behind electrodes for back illuminated MSM PDs (scattering for top illuminated MSM PDs) have to diffuse into the depleted region first, and then be swept out by the electrical field.

The maximum voltage that can be applied to the MSM PD is limited by the breakdown voltage V_{BD}. For biases over V_{BD}, impact ionization and tunneling occur, which result in a sharp increase of MSM PD current.

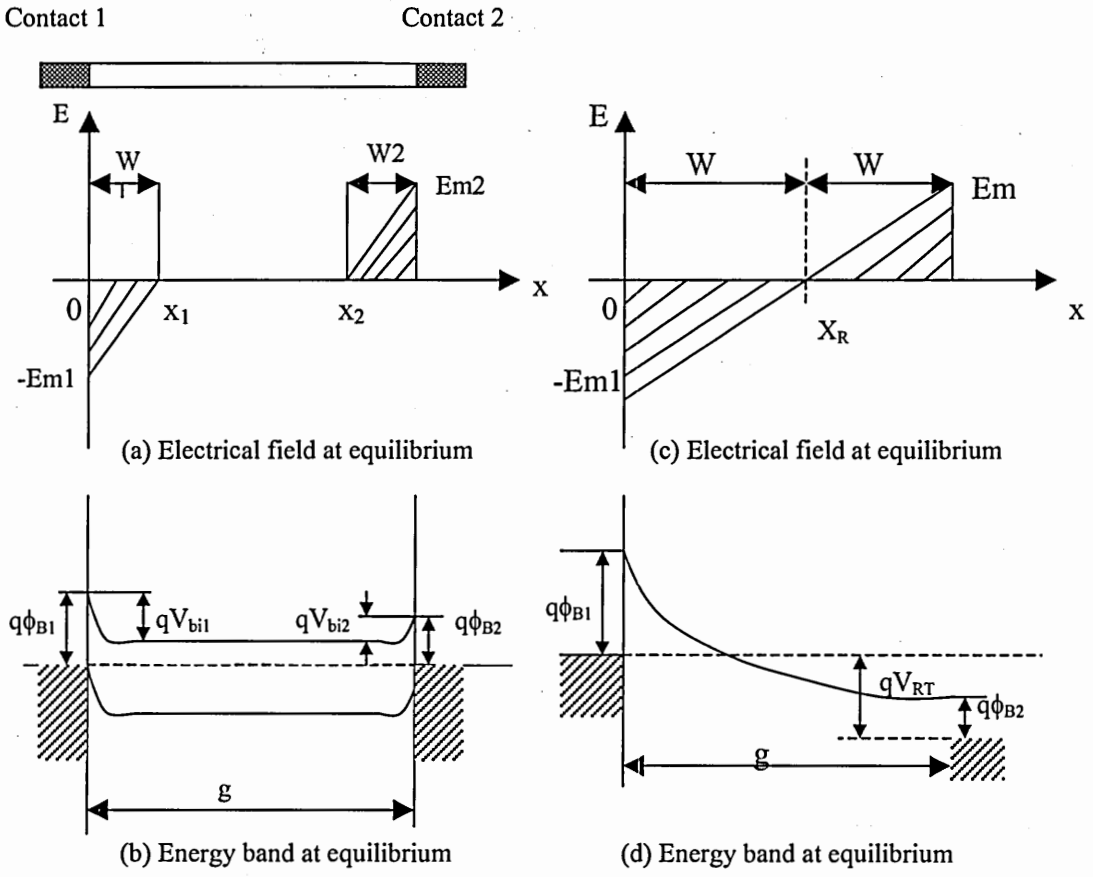

Figure 4: Electric field and energy band profiles (a) and (b) at a small bias voltage, (c) and (d) for reach through condition.

1.3.2 Intrinsic Cut-off Frequency of MSM PDs for High Speed Operation

The bandwidth of MSM PDs is determined by both the intrinsic response (transit time) and external response (RC time constant). In this research, the compound semiconductor materials are grown by molecular beam epitaxy (MBE). Trapping by recombination centers is negligible because of the high quality of the material. For a simple estimation, the average transit time of carriers can be expressed as:

$$\tau_{tr} = \frac{L_d}{v_d}, \tag{1.7}$$

where L_d is the carrier transit length between two fingers (i.e. finger gap g), and v_d is the combined drift velocity of the electrons and holes. The drift velocity of the holes is much slower than that of the electrons, so v_d can be simplified as the drift velocity of holes v_h [12]. The electric field decreases gradually from the electrode surface to the substrate. The transport velocity of carriers therefore also varies with the position inside the absorbing layer [13]. In a very simple estimation of transit time, a uniform electric field between electrodes is assumed for a MSM PD with 2 μm finger spacing and a 0.2 μm InGaAs absorbing layer with 0.06 μm cap layer and superlattice layer at bias of 5V:

$$E = \frac{(bias\ voltage)}{(finger\ spacing)} = \frac{5V}{2\mu m} = 25KV/cm. \tag{1.8}$$

At low electric fields, the drift velocity is proportional to the electric field strength E:

$$v_d = \mu E, \tag{1.9}$$

where μ is the mobility of InGaAs material, and μ can be approximated by:

$$\mu = (m^*)^{-3/2} T^{1/2}, \tag{1.10}$$

where m^* is the effective mass of carriers, and T is the temperature. In a high electric field, carriers move at a saturation velocity that is no longer proportional to the electrical field. The drift velocity of electrons at 25 kV/cm is 8.5×10^6 cm/sec. The saturation velocity of holes is 4.8×10^6 cm/sec [14]. The longest transit length for holes can be calculated as:

$$L_d = \sqrt{(2\mu m)^2 + (0.26\mu m)^2} = 2.017\mu m. \tag{1.11}$$

So the transit time τ_{tr} is calculated as:

$$\tau_{tr} = \frac{2.017\mu m}{4.8\times10^{6} cm/\sec} = 42p\sec \tag{1.12}$$

For a transit time limited PD, using Equation (1.1), the corresponding intrinsic cut-off bandwidth is the inverse of the transit time τ:

$$f = \frac{1}{2\pi\tau tr} = 3.79 \ \ GHz. \tag{1.13}$$

This simplified approximation uses a 1-dimensional calculation for the electric field, and ignores the RC time delay on the bandwidth. Usually, a 2-dimensional Monte Carlo simulation is involved for more accurate modeling [15].

1.3.3 External Response of MSM PDs for High Speed Operation

The charge-up time (RC time constant) of a MSM PD determines the external cut-off bandwidth, where R is approximately equal to the load resistance, and C is the capacitance of the PD. If the RC time constant of a PD is much longer than the carrier transit time, the bandwidth of the PD is limited by this RC constant, i.e. the capacitance of the MSM PD. The capacitance of a MSM PD can be calculated using the conformal mapping technique [16]. The unit capacitance as a function of finger width and gap is calculated as:

$$C_0 = \frac{\varepsilon_0(1+\varepsilon_r)K}{K'} \tag{1.14}$$

where C_0 is the capacitance per finger length, ε_0 is the dielectric constant in vacuum, and ε_r is the relative effective dielectric constant of the semiconductor. K and K' are elliptic integrals defined as:

$$K = K(k) = \int_0^{\pi/2} \frac{d\phi}{\sqrt{1-k^2 \sin^2 \phi}} \tag{1.15}$$

$$K' = K(k'), k' = \sqrt{1-k^2} \tag{1.16}$$

$$k = \tan^2\left(\frac{\pi w}{4p}\right), \tag{1.17}$$

where w is the finger width and p is the finger pitch, i.e. the sum of width (w) and gap (g). The total detector capacitance is then given by:

$$C = \frac{C_0 A}{P} \tag{1.18}$$

where A is the active detection area of a MSM PD.

1.4 Approaches for Multi Gigahertz MSM PDs with Thin Film I-MSM PDs

As shown in Equation (1.1), to realize broadband MSM PDs, both the RC time constant and the carrier transit time need to be minimized. In recent years, most research has focused on reducing the transit time. General methods of reducing carrier transit time include using nanotechnology to get submicron fingers and spacings [17,18], recessed cathode structures [19], low temperature grown materials [20,21,22], ion-implantation in the absorbing layer [23,24], and ultra-thin absorbing layer MSM PDs [25].

Using nanotechnology, submicron electrodes for MSM PDs can greatly reduce the transit time, but the fabrication is beyond the resolution limit of standard contact photolithography, and requires e-beam lithography that has low manufacturing

throughput. Recessed structures can slightly compress the pulse tail caused by slow carriers, but greatly increases the fabrication complexity of the MSM PDs.

In addition to shrinking the spacing to reduce the transit time, recombination centers can be purposely introduced in the absorbing layer to trap and recombine carriers with a long transit time. However, the responsivity is reduced in these recombination-limited MSM PDs. Low-temperature grown InGaAs material introduces point defects and microclusters to form midgap defect bands to capture both types of carriers, which then recombine[26]. MSM PDs fabricated with low-temperature grown InGaAs demonstrated improved bandwidth, but with very low responsivity. Growth of material at low temperatures is a relatively new research area, and has not yet been fully investigated. Ion-implantation (mainly Fe atoms) into the absorbing layer is another effective way to increase the device bandwidth by introducing recombination centers. MSM PDs fabricated with ion-implanted material suffer from very high dark current associated with the high-energy ion bombardment.

Besides reducing the transit time laterally (smaller finger spacing), thin absorbing layer MSMs can reduce the carrier transit time longitudinally to achieved high bandwidth. A MSM PD fabricated with thin absorbing layer material has produced a bandwidth of 12 GHz with standard photolithography. The tradeoff in thin absorbing layer MSM PDs is the increase in bandwidth with decreasing responsivity, because few photocarriers are generated with a fixed illumination power.

In this research, MSM PDs fabricated on varying absorbing layer thicknesses will be investigated towards a bandwidth of 10 GHz while optimizing the devices for the highest responsivity and largest area using standard contact photolithography fabrication

techniques. To improve the responsivity, a MSM PDs can be inverted for backside illumination, which is an effective way to improve the device responsivity[27, 28] by eliminating the finger shadowing effect. In this research, thin absorbing layer, inverted MSM PDs with back side illumination are fabricated and integrated for both photoreceiver and waveguide applications.

1.5 Statistical Analysis of Electrical Devices Using DOE

Design of experiments (DOE) was invented by a British scientist, Sir R. A. Fisher, in the 1920s as a method to maximize the knowledge gained from experimental data. It has evolved for over 70 years and became a popular statistical technique in the 1990s. In DOE analysis, a design matrix is prepared first, then statistical analysis is applied by linear, non-linear, or screening methods for modeling with different regression techniques [29].

Statistical analysis with a DOE matrix became popular first in chemical engineering and semiconductor manufacturing for process optimization. Nowadays, research on electrical device modeling using statistical analysis has started to emerge. For example, in the area of microwave research, multiplayer-packaged inductors and solenoid embedded inductors were statistically modeled [30, 31, 32] using a DOE matrix to obtain high Q devices. DOE modeling has also demonstrated usefulness in switch noise analysis[33], device process integration, optimization for opto-electronics integrated circuits (OEIC)[34], and circuit performance analysis[35].

In this work, numerous MSM PDs with varying structures were fabricated in array format and tested individually. Then, the measured data was statistically analyzed

to obtain models of responsivity, bandwidth and capacitance. Finally, the models were used to study the trend of the characteristics as a function of different photodetector physical structures to predict performance optimization.

CHAPTER 2

FABRICATION AND PROCESS OPTIMIZATION

The MSM PDs used in this research were fabricated in the Microelectronics Research Center cleanroom at Georgia Tech. The material was either purchased from a commercial vendor (Bandwidth®) or grown by Prof. April Brown's group. The material structures used for this research are shown in Table 1. Each wafer was given a sequence number shown in the parentheses. All materials have a thin InAlAs cap layer on the top, which is used to reduce the dark current. The Bandwidth® material has a composition alloy graded layer; the material grown by Prof. Brown's group has a superlattice graded layer. Both of these graded layers are designed to smooth the bandgap discontinuity between the cap layer interface and absorbing layer for a faster impulse response [36,37].

Table 1: I-MSM material structures: Bandwidth® and Prof. Brown's group.

	Thickness of Bandwidth® material	Thickness of Prof. April's grown material
InAlAs (cap)	400 Å	400 Å or 300 Å
InAlGaAs (graded layer)	500 Å	200 Å
InGaAs (Absorbing layer)	7400 Å	1000 Å (# 217), 2000 Å (# 218), 3000 Å (# 219), or 5000 Å (# 109)
InAlGaAs (graded layer)	500 Å	None
InAlAs (buffer layer)	400 Å	7000 Å or 1 μm
InGaAs (stop etching layer)	2000 Å	2000 Å
InP (substrate)	~ 550 μm	~ 550 μm

2.1 I-MSM PD Fabrication and Process Optimization

The fabrication and integration of the I-MSMs includes photolithography to define the fingers and contact pads of MSM PDs, e-beam evaporation and lift-off for metalization, mesa etch to separate the MSM devices, substrate removal to realize thin film devices, and transferring and bonding of devices to host substrates. Figure 5 outlines the process flow of the I-MSM fabrication process.

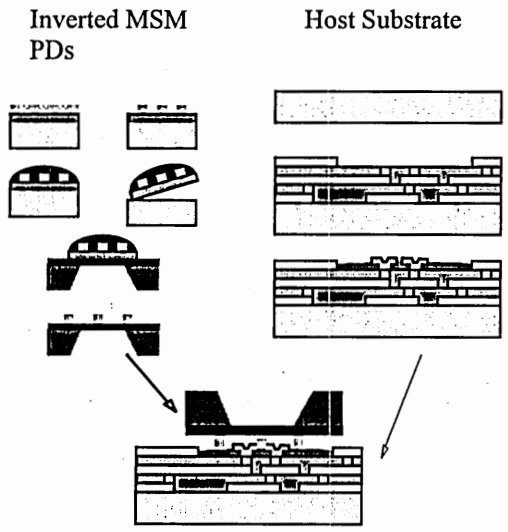

Figure 5: Process flow for I-MSM PD fabrication.

2.1.1 Photolithography

Negative photolithography was used to define interdigitated finger electrodes and contact pads for the MSM PDs. Because III-V compound semiconductor material is quite expensive, a small piece of material was cut from the whole wafer and processed each time. The size of each piece is around 5 mm by 5 mm. During photolithography, a fragment of scrap material was bonded along two edges of the sample. In this way, the edge bead fell mostly on the scrap materials during spin coating of photoresist. The scrap

material was then removed during the photoresist soft bake process step. Using this technique, the edge bead can be significantly reduced on the semiconductor samples.

2.1.2 Metallization and Lift-off

The metallization structure used for the MSM PDs was Ti (300 Å)/Pt (350 Å~ 500 Å)/Au (2500 Å~3000 Å). The Ti layer is deposited on the top of the sample first as an adhesion improvement layer, followed is a thin Pt layer for a diffusion barrier. Finally, Au is deposited as the top layer for good electrical conductivity. When the devices were heated above 200 °C, Au atoms could diffuse into the semiconductor (InAlAs cap layer), resulting in an ohmic contact or a leaky Schottky contact instead of a low leakage Schottky contact. Hence, the platinum diffusion barrier layer is necessary to maintain a good Schottky contact, to keep the dark current low in spite of any subsequent heating processes. To further reduce the dark current caused by diffusion of Ti atoms into the semiconductor at high temperature, a very thin Pt (around 40 Å to 50 Å) layer can be deposited prior to the Ti layer. However, Pt has a very high melting temperature, and requires high power to evaporate in the e-beam vacuum chamber. Heating of the photoresist during deposition results in over-heated photoresist, which is very undesirable in the lift-off process. Therefore, the thin Pt layer before Ti deposition is excluded if the dark current can be maintained in a satisfactory range for a particular application.

2.1.3 Mesa Etch and Substrate Removal

A mesa etch was used to separate MSM material into individual devices. Citric acid and H_2O_2 (10:1) were used for the mesa etch, with an etch rate of roughly 1000 Å/min. The etching stops at the top of stop etch layer (2000 Å InGaAs).

After the mesa etch, the sample is covered with Apiezon W for substrate removal. Apiezon W protects the top surface during the InP substrate removal, which uses HCl or HCl:H_3PO_4 (3:1). After the InP substrate is removed, the InGaAs stop etch layer is etched by citric acid and H_2O_2 (1:1) for around 2 minutes. The resulting MSM PDs are approximately 1 μm thick. Wet etchant of HCl or HCl: H_3PO_4 for InP is a well-known selective etchant over InGaAs (the stop etch layer). However, this etchant shows strong anisotropic effects [38]: a higher etch rate on [001] and [010] crystal directions than on [011] and [01$\bar{1}$]. It takes around 45 minutes to remove all of the InP substrate using HCl, resulting in highlighted defects, as shown in Figure 6 (a). In this research, different compositions of HCl to H_3PO_4 have been investigated for wet etching. A small portion of H_3PO_4 in the mixture will result in a slower etch rate than pure HCl. The best result has been achieved using HCl:H_3PO_4 (1:1) at 50 °C on a hotplate, resulting no highlighted defects as shown in Figure 6 (b).

2.1.4 Integration of Individual Devices to Host Substrates

After substrate removal, the MSM PDs are bonded onto a tight thin Mylar® polymer sheet, and the Apiezon W is removed using TCE. The thin film MSM PDs are transferred individually onto host substrates. The bonding material on the host substrate

is Ti (300 Å)/Au (5000 Å) for photoreceiver integration, and Ti (1000 Å)/Pt (500 Å)/Au (5000 Å) on SiO_2/Si or ceramic substrates for waveguide applications.

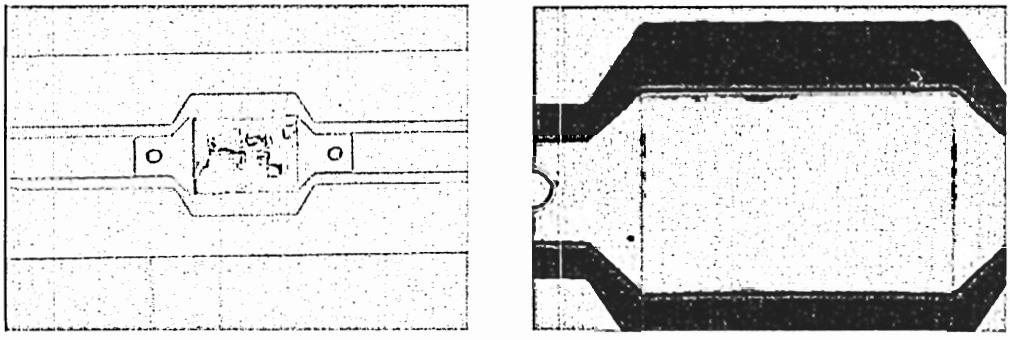

(a) (b)

Figure 6: I-MSM PD after substrate removal using different etchants. (a): InP substrate removed by HCl. (b): InP substrate removed by HCl:H_3PO_4 (1:1) on hotplate at 50°C.

2.1.5 Calibration Structure Fabrication

A Ni/Cr resistor was fabricated to calibrate the HP Lightwave Component Analyzer (LCA) using a SOL (short-open-load) method. The Ni/Cr had a ratio of 80:20 with a sheet resistance of 10 Ω to 400 Ω [39]. In this research, a Ni/Cr film of 1600 Å was deposited onto a thick glass substrate (1.2 mm thick) using an e-beam evaporator and negative photolithography. Then Ti/Au probing pads were photolithography defined and e-beam deposited onto the Ni/Cr resistor, as shown in Figure 7. Finally, the Ni/Cr resistor with size of 70 μm/100 μm (roughly 20 Ω) was laser trimmed to 50 Ω, as measured by a network analyzer.

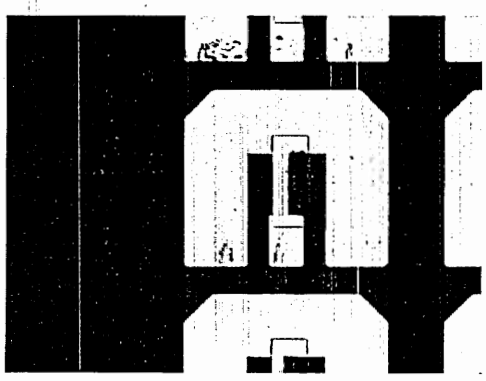

Figure 7: A Ni/Cr 50 Ω resistor with probing pads on a glass substrate.

2.2 On-Wafer MSM PD Fabrication and Process Optimization

On-wafer MSM PDs were fabricated on all materials with thin absorbing layer (# 217, # 218, # 219, # 109) in array format as shown on Figure 8. The fabrication included MSM metallization, benzocyclobutene (BCB) coating, BCB patterning, and probing pads deposition. A Ni/Cr resistor of 50 Ω was also fabricated on the same substrate as the on-wafer MSM PDs as a calibration structure for bandwidth and capacitance measurements.

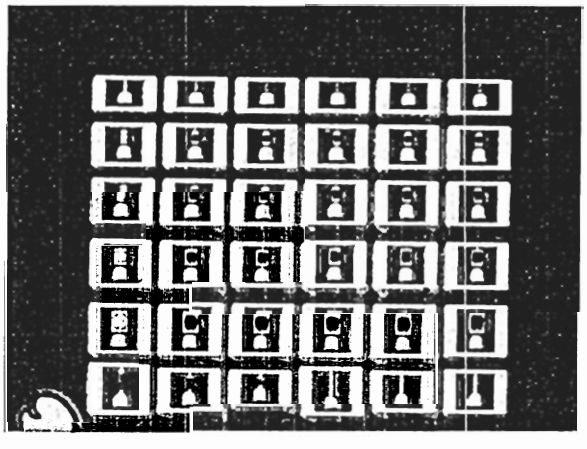

(a)

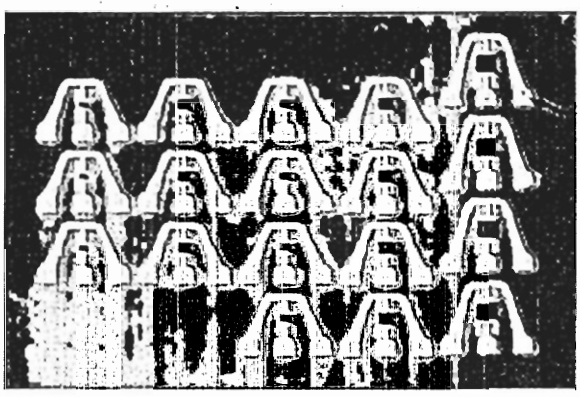

(b)

Figure 8: Arrays of on-wafer MSM PDs for (a) circular MSM PDs, and (b) square MSM PDs.

2.2.1 On-Wafer MSM PD Fabrication

For on-wafer MSM PDs, the metal fingers and electrical contacts were directly deposited on the compound semiconductor, and the probing pads were fabricated separately on dielectric material. The probing pads for the impulse response and bandwidth measurements were designed to match the shape of the ground-signal-ground (GSG) micro probing tips with 100 μm or 150 μm pitch. The area of the probing pads is much larger than that of MSM PDs, resulting in high parasitic capacitances if probing pads are directly deposited onto the semiconductor. To decouple the capacitance that arises from the probing pads, an isolation layer (low dielectric constant material) was used under the probing pads. In this research, conventional benzocyclobutene (BCB, Cyclotene 35) and photodefinable BCB (Cyclotene 4000 series) were explored as the isolation material.

First, the photolithography and metallization of the interdigitated electrodes and contact pads were fabricated in the same way as I-MSM PDs. The metallization for the

square MSM PDs was Ti/Pt/Au (300 Å/400 Å/2500 Å). The curing temperature for conventional BCB is as high as 220°C to 245°C, so the Pt layer is necessary to prevent diffusion of gold atoms into the semiconductor. After deposition of the MSM fingers, conventional BCB (3022-35) was spin-coated onto the surface of the square MSM arrays, resulting in a BCB thickness of approximately 1.6 μm. This BCB layer served as dielectric isolation between the probing pads and the compound semiconductor surface. The samples were cured at 220 °C~245 °C in a nitrogen flow oven for 1 hour. To avoid any loss of incident optical power due to BCB layer reflection and to minimize induced parasitic capacitance between the fingers of the MSM PDs, a window on each MSM active area was opened by reactive ion etching (RIE) with SF_6 and O_2. The final thickness of the BCB after RIE etching was approximately 1.1 μm. Finally, probing pads of Ti/Au (300 Å/5000 Å) were deposited to form electrical connections between the testing pads on the BCB layer and the MSM PD metallization on the compound semiconductor. Figure 9 (a) shows a photomicrograph of an on-wafer square MSM with 1/3 μm finger width/gap and an absorbing area of 50 μm by 50 μm.

The metallization of the interdigitated electrodes for circular on-wafer MSM PDs was Ti (300 Å)/Au (3000 Å). Photosensitive BCB (4022-35) was used as dielectric isolation for on-wafer circular MSMs. After electrode metallization, the photosensitive BCB was spin-coated onto the sample. The windows for the active MSM PD areas were defined by photolithography with exposure at a wavelength of 365 nm. The BCB window was opened with an immersion developer (Cyclotene™ DS3000). Then the samples were cured in a nitrogen flow oven for 1 hour at 200 °C. The resulting BCB thickness was approximately 3 μm. Figure 9 (b) is a photomicrograph of an on-wafer circular MSM

with finger width and gap of 1/3 μm and an absorbing region diameter of 50 μm. The photosensitive BCB process offers thicker isolation and fewer fabrication steps (omitting masking and dry etch steps) compared to the conventional polymer isolation processing.

(a) (b)

Figure 9: On-wafer MSM PDs with BCB isolation layers: (a) Square MSM PD with 1/3μm finger spacing and a 50 μm/50 μm active area and (b) Circular MSM PD with 1/3 μm finger spacing and active region diameter of 50 μm.

2.2.2 Calibration Structures for On-Wafer MSM PDs

A 50 Ω Ni/Cr resistor was fabricated on the isolation layer as a calibration structure for on-wafer MSM PD measurements. The fabrication followed the same process as the Ni/Cr resistor for I-MSM calibration. Figure 10 shows the Ni/Cr resistor for on-wafer MSM PD measuring calibration.

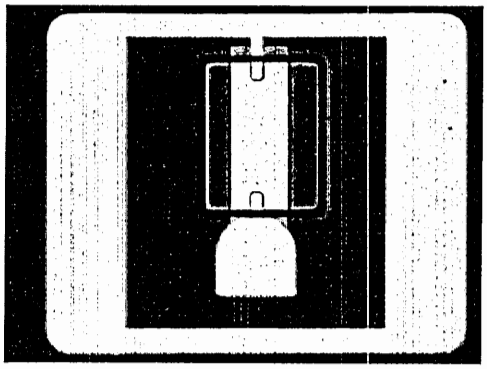

Figure 10: Resistor on the same substrate.

CHAPTER 3

ON-WAFTER MSM PD TESTING RESULTS

The measurements for on-wafer MSM PDs include dark current, responsivity, impulse response, bandwidth, and capacitance. First, the measured results were used as inputs for statistical analysis and modeling. Then the measured results of MSM PDs which were not used in the model construction were used to compare the predicted values to the measurements. The model construction and prediction will be discussed in the next chapter. In this chapter, the measured results of on-wafer MSM PDs will be presented for varied finger width and spacing, active area size, and absorbing layer thickness. For the AC analysis, measurement results are also given for different bias voltages.

3.1 Measurement Setup

The DC characterization and impulse response measurements were performed on the Cascade Microtech probe station. The responsivity of the MSM PDs were measured using a lensed single mode fiber (minimum spot size of 5 μm) with surface normal illumination at wavelengths of 1.3 μm and 1.55 μm. Both the photocurrent and dark current data were taken with a Labview acquisition program. The impulse response was measured with surface normal illumination of an IMRA fiber laser with 500 fs pulse width at a wavelength of 1.55 μm, and displayed on a Tektronix 50 GHz sampling oscilloscope (TDS 8000 series). Figure 11 shows the diagram of the impulse response measurement setup. The bias tee and ground-signal-ground (GSG) microprobe used for

the high speed measurement were an INMET® 8810EM with a 40 GHz bandwidth and a Cascade MicroTech® ACP 65 with a 65 GHz bandwidth, respectively.

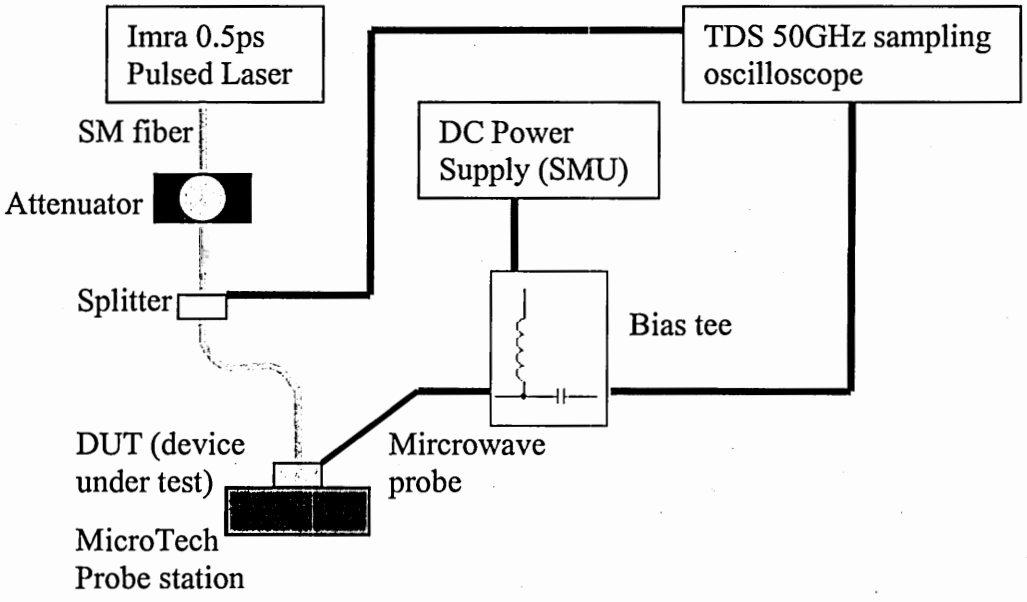

Figure 11: Diagram of the test setup for the impulse response.

The bandwidth of the MSM PDs was measured using a HP8703A Lightwave Component Analyzer (LCA) at a wavelength of 1.3 μm in conjunction with a Microtech probe station. The single mode lensed fiber was used again for better coupling of light to the MSM PDs because misalignment of the input fiber to the MSM PDs will result in power loss and significant frequency response degradation if the low electric field regions outside the active area are illuminated. The lightwave component analyzer was calibrated with on-wafer calibration structures using the Short-Open-Load (SOL) method [40]. The load in the calibration utilized a Ni/Cr thin film resistor of 50 Ω. Data was gathered for each test run between 1 GHz and 20 GHz using BenchLink data acquisition software.

3.2 DC Characteristics

3.2.1 Dark Current Measurement and Analysis

The dark current of MSM PDs comes from the leakage of the Schottky contact electrical fingers at the metal/semiconductor interface. It increases with bias voltage and saturates at high bias before break down. In this measurement, all dark currents were taken at a bias of 5 V, and in general, they were less than 20 nA for PDs with size smaller than 80 μm in diameter. Because material 109 has a thinner InAlAs cap layer, the dark current of PDs fabricated from material 109 was higher than PDs on material 219. Dark currents taken from other thin absorbing layer MSM PDs are similar to PDs on material 219 due to the same thickness of the InAlAs cap layer. Table 2 compares the dark current for MSM PDs on material 219 and material 109. The dark currents were measured using a Keithley 236 Source Measure Unit (SMU).

Table 2: The dark currents for a variety of MSM PDs on material 109 and material 219. The average currents are taken exclude the PD of D80/1/2 on 219 and D40/1/2 on 109, which are anomalously high.

Material	MSM diameter	Finger width/spacing in units of μm					Average
		1/1	1/2	1/3	2/2	2/3	
Material 219 (400 Å InAlAs)	D80 μm	5.2 nA	224 nA	1.2 nA	2.2 nA	2.0 nA	2.65 nA
	D60 μm	3.0 nA	2.6 nA	2.4 nA	1.8 nA	2.0 nA	2.4 nA
	D40 μm	1.2 nA	1.4 nA	0.9 nA	1.2 nA	0.9 nA	1.1 nA
Material 109 (300 Å InAlAs)	D80 μm	40.3 nA	28.6 nA	40.3 nA	47.3 nA	48.1 nA	40.9 nA
	D60 μm	24.6 nA	24.2 nA	24.0 nA	24.8 nA	33.4 nA	26.2 nA
	D40 μm	12.4 nA	33.6 nA	9.8 nA	12.0 nA	9.5 nA	10.9 nA

In general, dark currents are a good indication of the quality of the wafer: any localized defects in one area of the material may cause a high dark current of that MSM PD, and this explains the dark currents of PD D80/1/2 on material 219 and D40/1/2 on material 109, which are much higher than adjacent MSM PDs. However, from Table 2, the trend of dark current with varying size, finger width and spacing is clear: (1) MSM PDs on material 109 have a higher dark current, probably due to the thin InAlAs cap layer; (2) dark currents are higher for PDs with larger size; and (3) dark current is not sensitive to varying finger widths and gaps.

Low values of the dark current are extremely sensitive to the contact of the probing tips to the electrical contacts of the MSM PDs and fluctuation (noise) from the testing equipment (SMU). While measuring higher currents, the dark current curve as a function of voltage bias is smoother and the testing result is more accurate. So the dark currents from material 109 at higher average values are more precisely recorded than dark currents for PDs on material 219.

A careful evaluation of the average dark currents for PDs on material 109 reveals that the dark current is roughly proportional to the PD size. The ratio for the active area size for PDs with diameter of 80 μm, 60 μm, and 40 μm is 4 : 2.25 : 1, while the ratio for the corresponding dark current is 3.75 : 2.40 : 1 on material 109.

For applications such as MSM PDs integrated onto CMOS photoreceivers, the dark current of PDs is not a major source of noise because receiver noise dominates if the MSM dark current is less than 1 μA. In this research, the PDs on material 109 have the highest dark current (several tens of nanoamperes), which is much lower than the circuit

requirement, thus the research herein focuses on other critical characteristics of MSM PDs, such as responsivity, speed, and capacitance.

3.2.2 Responsivity Measurement for Square On-Wafer MSM PDs

The responsivity of PDs increases with increasing of absorbing layer thickness, and decreases with the finger shadowing percentage for on-wafer MSM PDs. Herein, responsivity was first investigated in relation to the finger gap and photoactive area size on square MSM PDs. These MSM PDs were fabricated from Bandwidth® material with a 7400 Å absorbing layer thickness. The finger width was set at 1 μm with a varying finger gap of 2 μm and 3 μm. The sizes of these MSM PDs were 20 μm × 20μm, 40 μm × 40 μm, and 50 μm × 50 μm square. The measured responsivities are shown in Table 3. The PDs with the same finger gap and width (shadowing percentage) have similar responsivity for different sizes. A detailed modeling for responsivity as a function of size and finger gap will be presented in the next chapter.

Table 3: Responsivity measurement results for square on-wafer MSM PDs with varying finger gap and photoactive area size.

Measurement	Finger gap (G)	Size (S)	Responsivity (A/W)
1	2 μm	40 μm	0.4153
2	3 μm	40 μm	0.4646
3	2 μm	50 μm	0.4216
4	3 μm	50 μm	0.4695
5	1 μm	20 μm	0.4438
6	2 μm	20 μm	0.4060
7	3 μm	20 μm	0.3883

3.2.3 Responsivity Measurement for Circular On-Wafer MSM PDs.

The responsivity measurements of on-wafer square MSM PDs shows that the size of the MSM PDs has little effect on the PDs responsivity unless the input fiber is misaligned. In this section, a more complex analysis of the responsivity for circular on-wafer MSM PDs was investigated to ascertain the relationships between material thickness, finger width, and finger gap. The responsivity was measured under 1.3 μm laser illumination at a 5 V bias for MSM PDs. The results are shown in Table 4. The modeling of responsivity as a function of finger width, spacing, and absorbing layer thickness will be discussed in the next chapter.

Table 4: The responsivity of on-wafer MSM PDs on different materials. The first row shows the finger width/gap of PDs. The responsivity has units of A/W.

Wafer # (absorbing layer thickness	1/1 μm	1/2 μm	1/3 μm	2/2 μm	2/3 μm
217 (0.1μm)	0.03545	0.04158	0.05362	0.03972	0.0441
218 (0.2μm)	0.07894	0.10557	0.11491	0.08552	0.09642
219 (0.3μm)	0.10444	0.14728	0.16542	0.12123	0.14351
109 (0.5μm)	0.16027	0.21933	0.25567	0.17458	0.2125

3.3 Impulse Response

The impulse responses were measured with the test setup discussed in section 3.1. The system was calibrated with a commercial photodetector with a 45 GHz bandwidth from New Focus®. The measured pulse for this commercial PD is shown in Figure 12, and has a full width at half maximum (FWHM) of 20 ps. The impulse responses of on-

wafer MSM PDs arrays were measured for varying absorbing layer thickness, finger width and finger spacing and voltage bias.

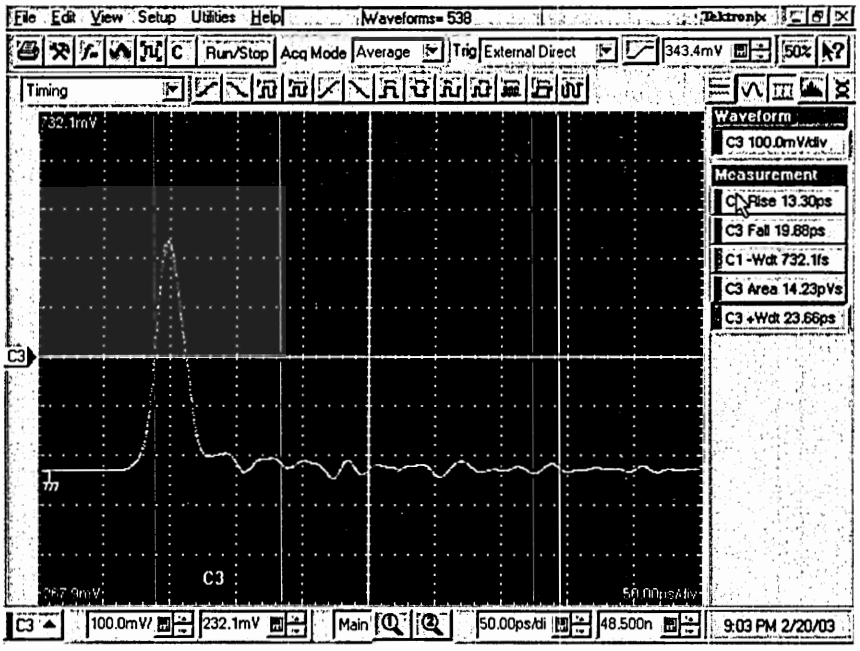

Figure 12: The measured impulse response of a New Focus 45 GHz photodetector.

3.3.1 Impulse Response of Varying Finger Width and Spacing

The transit time of carriers varies with the finger width and spacing due to the nonlinear distribution of the electric field in the MSM PDs. In Figure 13, the impulse response is plotted as a function of varying finger width and spacing for PDs with active area diameter of 80 μm on material 219 (3000 Å absorbing layer thickness) at a bias of 9 V. The PDs with 80 μm active area were selected because the fiber misalignment can be eliminated (since this is a large size PD). The impulse responses of PDs on other materials and with smaller active area size displayed similar behavior.

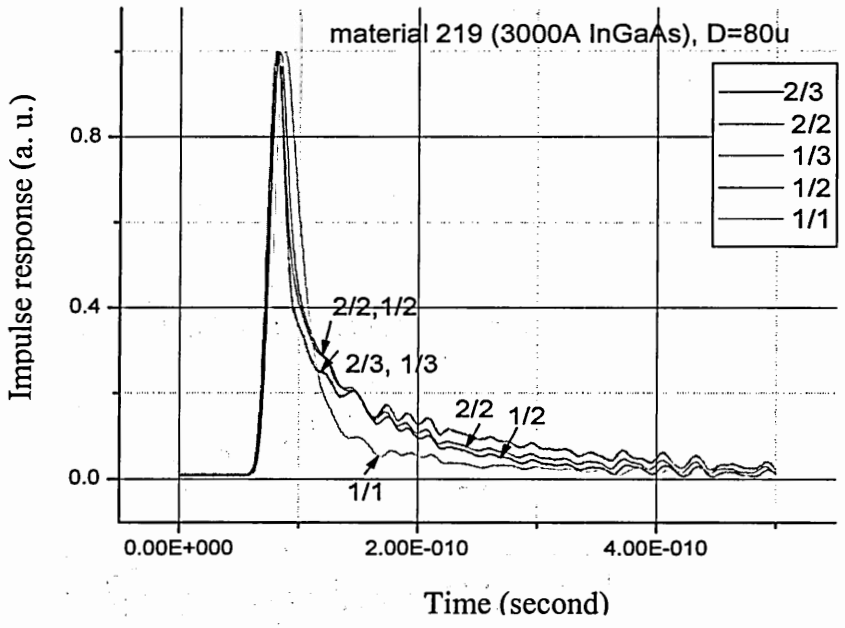

Figure 13: Impulse response with varying finger width/spacing for on-wafer MSM PDs at size of 80 μm on material 219.

In Figure 13, the 1/1 μm device has a much more compressed tail than the other MSM PDs. The MSM PDs with 1/2 μm and 2/2 μm have very similar responses to each other, and the impulse responses of MSM PDs with 1/3 μm and 2/3 μm finger width/spacing are almost identical to each other. The electric field distribution between electrodes is similar for MSM PDs with the same finger spacing but different finger width. Therefore, the finger width has little effect on the impulse response of on-wafer MSM PDs since most carriers are generated between electrodes and will experience the same acceleration by the electric field. The impulse response can be roughly divided into two regions: the "pulse part" which can be examined as the FWHM, and the "tail part" which can be studied as the fall time of the pulse. It is interesting to note that the FWHM of the 1/1 μm finger width/spacing PD (26.30 ps) is wider than other PDs with wider finger spacing. The "pulse part" of the response mainly comes from electron current, and

the "tail part" mainly comes from the slow motion carriers (holes). Since the tail of the impulse is dominated by the holes, the PD with 1 μm finger spacing has more carriers collected in the time period of the "pulse part", resulting in a wider FWHM, and fewer carriers to collect in the tail, resulting in a compressed tail. In contrast, for MSM PDs with 2 μm and 3 μm spacings, there are fewer holes collected in the "pulse part" and therefore more holes have to be collected in the "tail part", and this leads to a narrower pulse width but longer tail. The heavy dependence of the impulse response on finger spacing indicates that these MSM PDs are transit time limited.

3.2.2 Impulse Responses at Different Bias Voltage

The drift velocity of the electrons increases with the electric field, and then decreases with increasing electric field as the voltage bias continue to increase (the Gunn effect). The drift velocity of holes increases monolithically with electric field and saturates at a high voltage bias. Thus, the impulse response of MSM PDs also displays strong voltage bias dependence, as shown in Figure 14. In this figure, the impulse responses of MSM PDs fabricated on material 219 at a size of 80 μm with finger width/spacing of 1/1 μm is plotted for voltage biases from 2 V to 11 V. The tail is bigger at a lower bias and compressed significantly at biases higher than 5 V. The impulse response changes only slightly from biases of 7 V to 11 V, which indicates that most of the holes travel at their saturation velocity at biases higher than 7 V for PDs with finger spacing of 1 μm for this material structure.

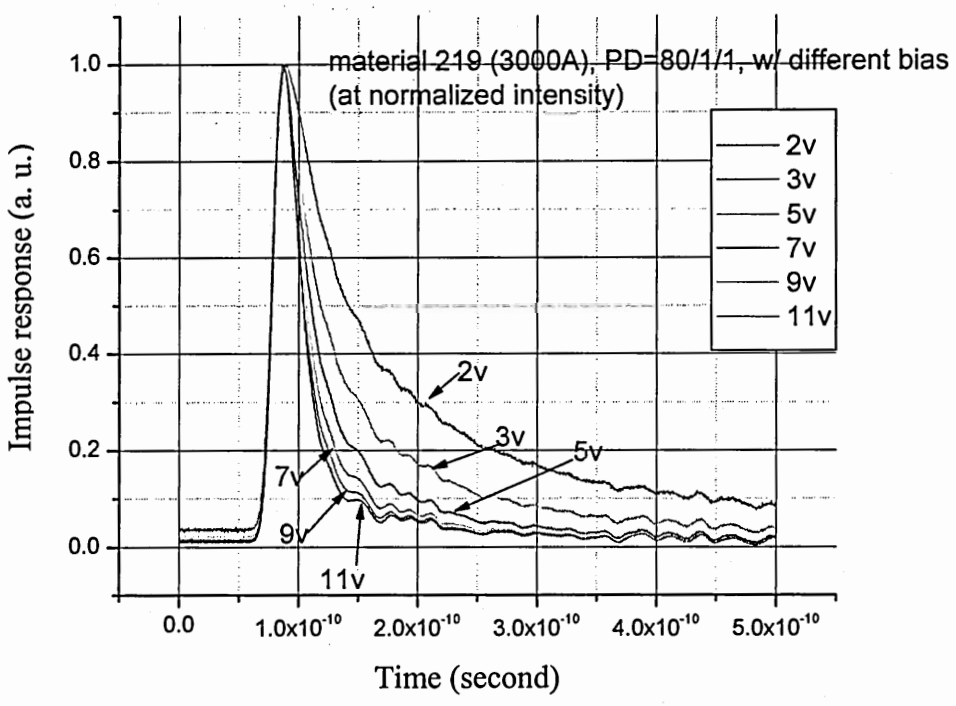

Figure 14: The impulse responses of circular MSM PDs with 1 μm finger spacing at voltage biases from 2 V to 11 V.

3.2.3 Impulse Response with Different Absorbing Layer Thickness

The analysis of the non-linear distribution of the electric field in MSMs with different absorbing layer thicknesses is rather complex. The electric field strength decreases rapidly as a function of depth in the absorbing layer. The photogenerated carriers near the surface have a faster drift velocity than carriers generated deep in the absorbing layer. Also, carriers generated deep in the absorbing layer have a longer transit distance to the electrodes. Therefore, reducing the absorbing layer thickness is an effective way to shorten the transit time of slow carriers. The improvement in speed performance for thin absorbing layer MSM PDs is at the sacrifice of the PDs responsivity due to fewer photogenerated carriers. Figure 15 shows a plot of PD impulse responses

with absorbing layer thicknesses of 1000 Å, 2000 Å, and 5000 Å at bias of 9 V. In Figure 15 (a), the impulse amplitude of the PD on material 109 (5000 Å InGaAs) has the highest value and the impulse amplitude on material 217 (1000 Å InGaAs) has the lowest. This agrees with expectation, since material 217 has thinnest absorbing layer thickness. In Figure 15 (b), the normalized impulse plot reveals that the tail of the impulse is compressed with decreasing absorbing layer thickness. The fastest response of PD on material 217 among all comes from the reduced transit time of carriers due to thin absorbing layer thickness.

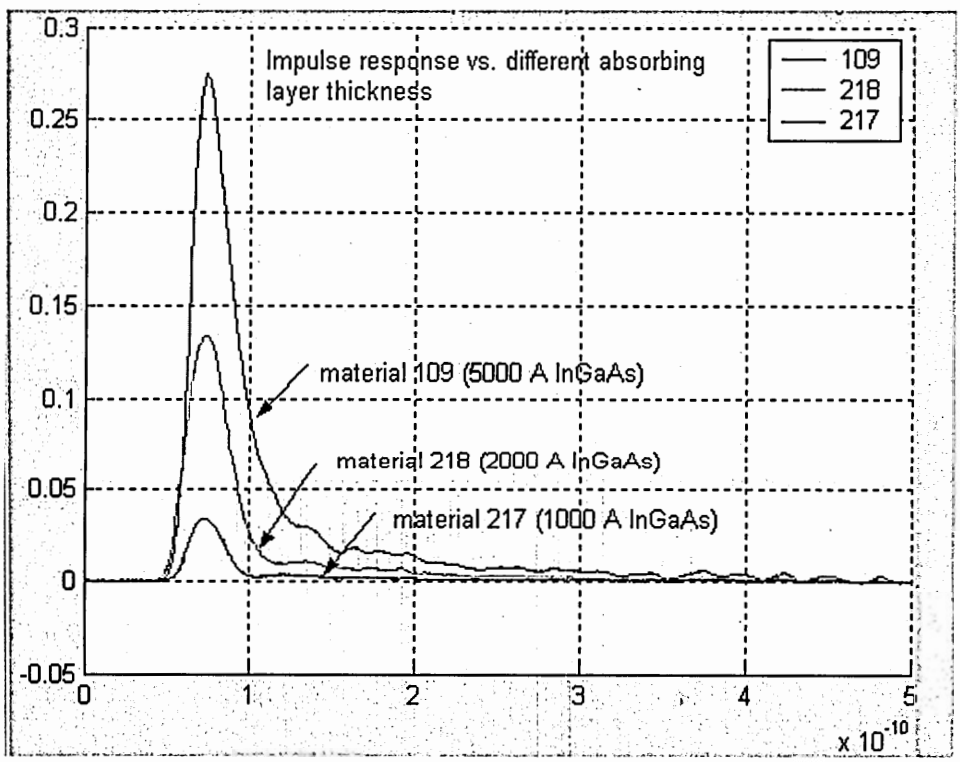

(a)

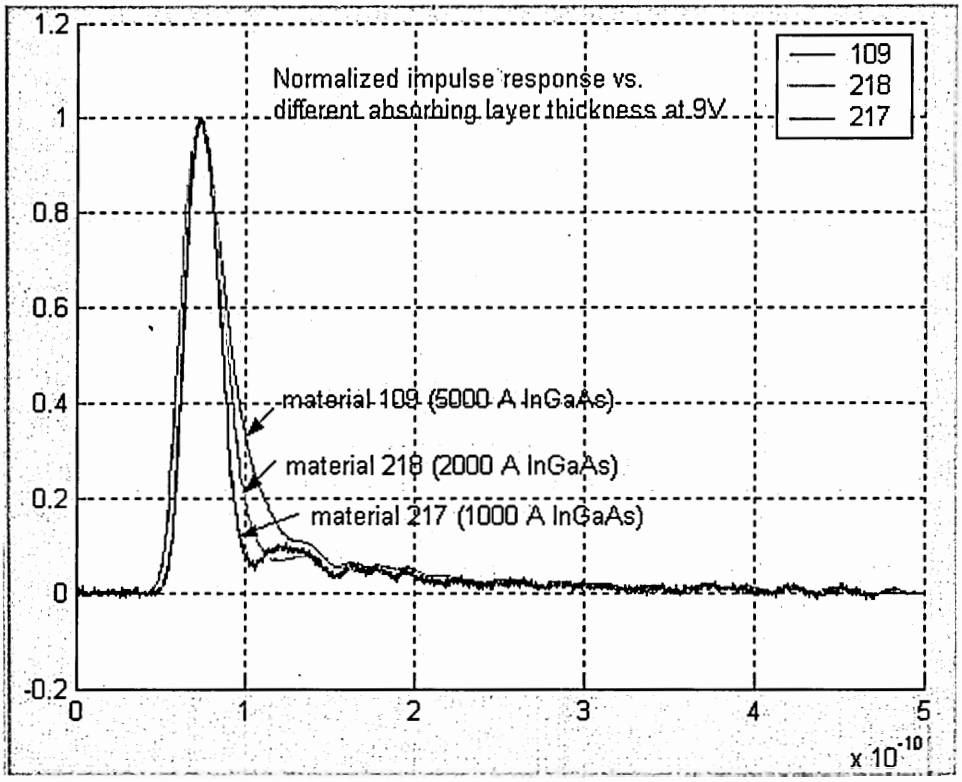

(b)

Figure 15: Impulse response of on-wafer circular MSM PDs with different absorbing layer thickness, where (a) is the impulse response without normalization and (b) is the normalized impulse response.

3.2.4 PD Impulse Responses with Different Absorbing Areas

The external RC time delay also has an impact on the speed performance of the MSM PDs. Although the capacitance of the MSM PD is a function of finger width, finger spacing, and PD size, the active area size is the most significant term. Thus, it is worthwhile to study the impulse response variation with PD size. The measurement results for MSM PDs with active area diameters of 40 μm, 60 μm, and 80 μm with finger width/spacing of 1/1 μm on material 219 are shown in Figure 16. The impulse response of the MSM PD with a diameter of 80 μm has a slightly longer tail than MSM PDs of smaller sizes. The fall-time of the tails (from 90% to 10%) for MSM PDs of diameter of

80 μm, 60 μm, and 40 μm are 49 ps, 41 ps and 45 ps, respectively. The differences in the fall times are moderate, although the capacitance of the 80 μm PD is 4 times larger than 40 μm PD, as calculated from Equation (1.18). This means that the external RC time delay is less dominant than the transit time of the PDs on material with 3000 Å absorbing layer of InGaAs with a diameter of 80 μm or less.

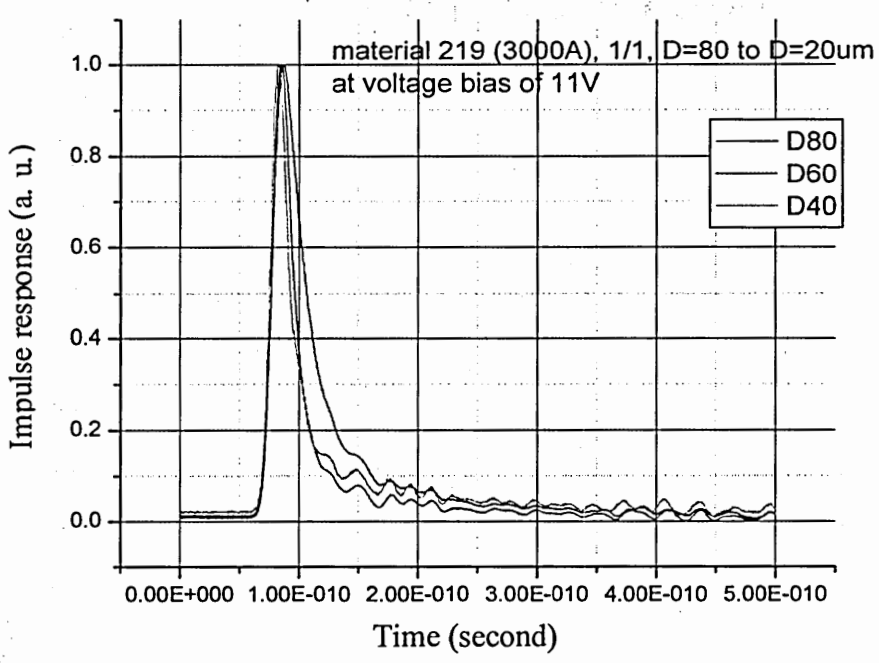

Figure 16: The impulse responses for on-wafer circular MSM PDs with varied active area.

3.4 Bandwidth

Circular MSM PDs generate a high level of interest because they match the shape of the light emission from typical optical fibers. The bandwidth (s-parameter s21, optical to electrical) was measured using a HP 8701A Lightwave Component Analyzer which has a bandwidth of 20 GHz. The test setup was discussed in Section 3.1. Figure 17 shows

a typical plot of bandwidth (s21 in units of db) as a function of frequency in a semi-log scale for MSM PDs with varying finger widths and spacings. Other MSM PDs have bandwidth plots of similar shape but different -3 dB frequencies. Table 5 lists a summary of the bandwidth of MSM PDs with varying absorbing layer thicknesses, finger widths, finger spacings, and active area sizes at a bias of 11 V.

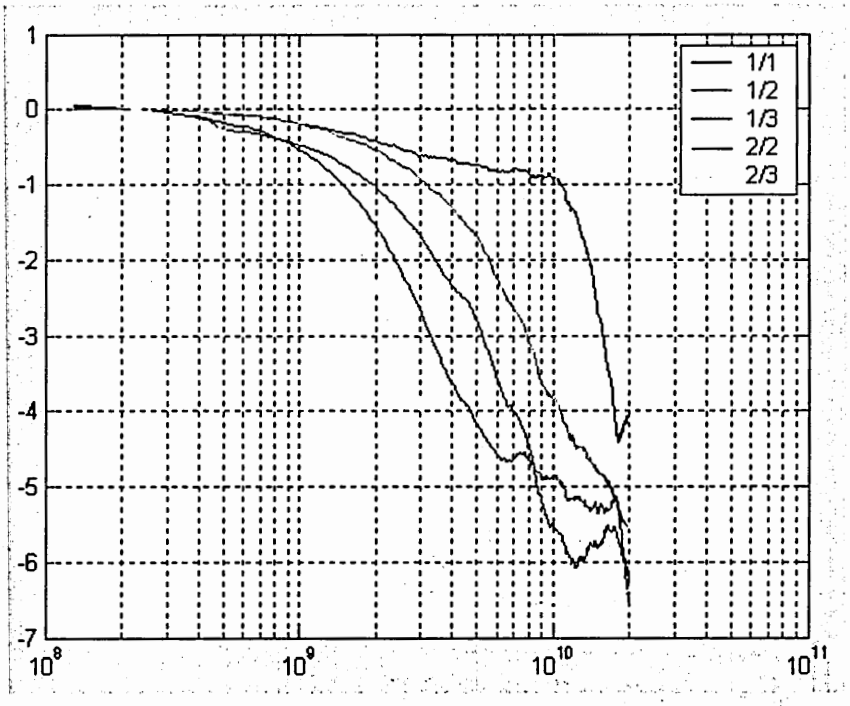

(a)

Figure 17: Bandwidth measurement of PDs with active area diameter of 80 μm on material 219 with varying finger width/spacing.

Ten MSM PDs with the same size, finger width, and finger spacing on the same material measured from two different fabrications runs differed by less than 10% in bandwidth. Multiple measurements were also conducted on the same detector several times to test the repeatability of the measurement, and resulted in less than 5% deviation. In Table 5, bandwidth (-3 dB frequency) is summarized for PDs on different materials

with different finger widths and gaps in the first row, and diameter size of the active area of the MSM PDs in the first column.

Table 5: Measured bandwidths (Hz) of circular MSM PDs. The left column lists the MSM PD diameter and the first row lists the finger width/finger gap.

	1/2 μm	1/3 μm	2/2 μm	2/3 μm
Devices fabricated on wafer with 0.1μm InGaAs absorbing thickness				
D40 μm	7.30G	4.05G	7.48G	3.50G
D50 μm	7.02G	3.43G	7.15G	3.32G
D60 μm	6.66G	2.91G	6.55G	3.07G
Devices fabricated on wafer with 0.2μm InGaAs absorbing thickness				
D40 μm	7.03G	3.85G	7.20G	3.14G
D50 μm	6.88G	3.25G	6.86G	3.02G
D60 μm	6.52G	2.64G	5.36G	2.70G
Devices fabricated on wafer with 0.3μm InGaAs absorbing thickness				
D40 μm	N/A	3.36G	7.13G	3.06G
D50 μm	6.79G	2.99G	6.22G	2.8G
D60 μm	6.35G	2.53G	6.13G	2.45G
Devices fabricated on wafer with 0.5μm InGaAs absorbing thickness				
D40 μm	6.97G	2.77G	7.02G	2.61G
D50 μm	6.65G	2.61G	6.11G	*2.39G*
D60 μm	6.04G	2.15G	5.73G	2.22G

3.5 Capacitance

The capacitances of MSM PDs were measured using the HP LCA in collaboration with Dr. Martin Brooke's group. The LCA was calibrated with on-wafer structures of open, short, and a 50 Ω Ni/Cr resistor. The scatter matrix of s22 data was taken for both amplitude and phase, and then converted to capacitance as a function of

frequency. The measured capacitance was high at low frequency and saturated quickly with increasing frequency at roughly 2 GHz. The high capacitance value at low frequency is due to LCA calibration optimized at high frequency, not at low frequency. Table 6 lists the calculated capacitance at 10 GHz for circular MSM PDs with different sizes, finger widths, and finger spacings. The capacitance of MSM PDs is determined by the geometry and material dielectric constant and do not sensitive with the absorbing layer thickness. The capacitances of circular on-wafer MSM PDs were then fit into a statistical model, which will be discussed in the next chapter.

Table 6: The capacitance values of circular on-wafer MSM PDs (units of fF). The first row is the finger width/gap, and the first column is the diameter size of MSM PDs.

	1/1 μm	1/2 μm	1/3 μm	2/2 μm
D 40 μm	59.7	44.5	35	42.8
D 50 μm	83	64.5	52	66.5
D 60 μm	130.3	84	75.7	106
D 80 μm	197.5	143.3	107	160.5

CHAPTER 4

STATISTICAL ANALYSIS OF ON-WAFER MSM PDS USING A DOE MATRIX

4.1 Statistical Modeling of MSM PDs Using a DOE Matrix

In this research, a two-level, multi-parameter DOE model [41] was developed for MSM PD modeling. One objective of this thesis is to explore whether DOE modeling is a valid prediction tool for MSM design, and in the case of capacitance, whether DOE is superior to theoretical conformal mapping for MSM capacitance prediction. The input variables are A, B, C, and the output is Y. To have a two-level DOE analysis, each input must have two different values: low and high. The total number of runs for full factorial DOE is calculated as:

$$total\ \#\ of\ runs = (\#\ of\ levels)^{\#\ of\ parameters}. \tag{4.1}$$

A total of 8 runs are required for a 3-parameter, 2-level DOE system analysis. In Table 7, a list shows how high and low values are assigned to each parameter. After the tests are set up according to Table 7, a design matrix is constructed in order to build a model based on these data. In this research, a linear model is used to keep the calculation simple. Table 8 shows the design matrix for the experimental design for a 3-input, 2-level analysis.

Table 7: Runs required for a 3-parameter 2-level DOE analysis.

Run	A (input)	B (input)	C (input)	Y (output)
1	Low	Low	Low	
2	Low	Low	High	
3	Low	High	Low	
4	Low	High	High	
5	High	Low	Low	
6	High	Low	High	
7	High	High	Low	
8	High	High	High	

Table 8: Experimental design matrix for 3-input, 2-level analysis

	Effect of single input			Effect of interaction of 2 inputs			Effect of interaction of 3 inputs	Output
Run	A	B	C	AB	BC	AC	ABC	Y
1	-1	-1	-1	1	1	1	-1	
2	-1	-1	1	1	-1	-1	1	
3	-1	1	-1	-1	1	-1	1	
4	-1	1	1	-1	-1	1	-1	
5	1	-1	-1	-1	-1	1	1	
6	1	-1	1	-1	1	-1	-1	
7	1	1	-1	1	-1	-1	-1	
8	1	1	1	1	1	1	1	
Avg (+1)	A_{-1}	B_{-1}	C_{-1}	AB_{-1}	BC_{-1}	AC_{-1}	ABC_{-1}	Y_{avg}
Avg (-1)	A_{+1}	B_{+1}	C_{+1}	AB_{+1}	BC_{+1}	AC_{+1}	ABC_{+1}	
Delta	ΔA	ΔB	ΔC	ΔAB	ΔBC	ΔAC	ΔABC	

In the two-level case, the average (+1) is obtained by summing all Y values with high value inputs, and the average (-1) is obtained by summing all Y values with low value inputs. The delta value in the last row of Table 8 is the result of the difference between Avg (+) and Avg (-), which can be expressed as:

$$\Delta X = \sum Y(+X) - \sum Y(-X), \tag{4.2}$$

where X is any input variable (A, B, C) or a combination of the input variables.

A least squares regression model is used herein, which can be simplified as:

$$\hat{Y} = Y_{avg} + \frac{\Delta A \times A_c}{2} + \frac{\Delta B \times B_c}{2} + \frac{\Delta C \times C_c}{2} + \frac{\Delta AB \times AB_c}{2} + \frac{\Delta BC \times BC_c}{2} + \frac{\Delta AC \times AC_c}{2} + \frac{\Delta ABC \times ABC_c}{2}. \quad (4.3)$$

The above equation includes the effect from independent variables (A, B, C), and effects from interactions between independent variables (AC, BC, AC, ABC). Variables with subscript c are coded setting variables, which relate to the actual values denoted with subscript a as:

$$X_a = \frac{X_H + X_L}{2} + \frac{(X_H - X_L)}{2} \times X_c, \quad (4.4)$$

where X_a is the setting value of each independent variable. X_H and X_L are the experimental high value and low value, respectively. From this equation, it is possible to calculate the expression for the coded setting variables:

$$X_c = \frac{2X_a - (X_H + X_L)}{X_H - X_L}. \quad (4.5)$$

The predicted model for $\hat{Y}$ is expressed with coded values. Thus, we can insert Equation (4.5) into Equation (4.3), and get the expression for $\hat{Y}$ as a function of the setting values of each variable.

4.2 Responsivity Analysis and Modeling Using DOE

4.2.1 Responsivity modeling for Square MSM PDs

In this section, the responsivity of square MSM PDs will be studied with respect to finger gap and active area size. The high and low setting levels are 3 μm and 2 μm for finger gap, and 60 μm and 40 μm for active area size. Table 3 lists the measured responsivity a 2-level, 2-parameter DOE matrix construction, and Table 9 shows the DOE design matrix.

Table 9: DOE matrix for responsivity analysis of MSM PDs.

Run	G	S	GS	Responsivity (R) (A/W)
1	-1	-1	+1	0.4153
2	+1	-1	-1	0.4646
3	-1	+1	-1	0.4216
4	+1	+1	+1	0.4695
Avg (+1)	0.46705	0.44555	0.4424	0.44275
Avg (-1)	0.41845	0.43995	0.4413	
Delta	0.0486	0.0056	0.0007	

From Equation (4.3), we can express the responsivity of the MSMs as the following:

$$\begin{aligned}\hat{R} &= \overline{R} + \frac{\Delta G}{2} Gc + \frac{\Delta S}{2} Sc + \frac{\Delta GS}{2} GcSc \\ &= 0.44275 + \frac{0.0486}{2} Gc + \frac{0.0056}{2} Sc + \frac{-0.0007}{2} GcSc\end{aligned}, \tag{4.6}$$

and

$$\begin{aligned}Ga &= \frac{G_H + G_L}{2} + \frac{G_H - G_L}{2} Gc \\ &= \frac{2+3}{2} + \frac{1}{2} Gc\end{aligned}. \tag{4.7}$$

So,

$$Gc = \frac{Ga - 2.5}{0.5} = 2Ga - 5. \tag{4.8}$$

Similarly,

$$Sa = \frac{S_H + S_L}{2} + \frac{S_H - S_L}{2} Sc = \frac{40+50}{2} + \frac{10}{2} Sc. \tag{4.9}$$

So,

$$S_c = \frac{Sa - 45}{5} = 0.2S_a - 9. \tag{4.10}$$

Substituting Equations (4.8) and (4.10) into Equation (4.6), results in:

$$\hat{R}= 0.44275 + 0.0243\ (2Ga-5) + 0.0028\ (0.2Sa-9) - 0.00035\ (2Ga-5)(0.2Sa-9)\ .(4.11)$$

Equation (4.11) then is simplified as:

$$\hat{R}= 0.2803+0.0549Ga+0.000091Sa-0.00014GaSa\ . \qquad (4.12)$$

Equation (4.12) is the regression equation for responsivity for the square MSM PDs derived directly from measured data. The coefficients of the size of the MSM PDs and the interaction term are much smaller than the coefficient of the finger gap. So, the responsivity is dominated by the finger gap for a particular material structure. This agrees with the expectation from the empirical analysis of responsivity. Equation (4.12) is then used to compare the predicted results with the measured results for other MSM PDs that were not used to formulate the regression, as shown in Table 10. The MSM PDs all have a size of 20 μm × 20 μm and finger width of 1 μm, but varied finger spacing of 1 μm, 2 μm and 3 μm. The average prediction error is 4.36%.

Table 10: The calculated responsivity in comparison to measured results.

Finger width/gap (μm)	Responsivity predicted (A/W)	Responsivity measured (A/W)	Prediction Error
1/3 μm	0.4548	0.4438	2.5%
1/2 μm	0.4024	0.4060	0.88%
1/1 μm	0.3506	0.3883	9.7%

4.1.2 Responsivity Modeling Using Rs/Discover for Circular MSM PDs

Based on the analysis in the previous section that the responsivity is independent of the PD size, the modeling of responsivity for circular MSMs will focus on finger width, finger gap, and absorbing layer thickness. To obtain the necessary data for modeling the

MSM PD responsivity, a 2^3 full factorial experimental design was employed. The input variables were finger width, finger gap, and material absorbing layer thickness. The low and high levels for the input variables are 1 μm and 2 μm for the finger widths, 2 μm and 3 μm for the finger gaps, and 0.1 μm and 0.5 μm for the absorbing layer thicknesses. The experiment consisted of 8 runs. The commercial statistical software package RS/Discover[42] was used to analyze the results of the experiment and to generate a linear model for the responsivity. The coefficients in the model and the level of significance of each of the main effects and the two-factor interactions are summarized in Table 11. The terms are in coded format (with subscript c) where *FW*, *FG*, and *MT* represent finger width, finger gap, and material absorbing thickness, respectively.

Table 11: DOE table for responsivity analysis.

Term	Coefficient	Significance level (p-value)
Constant	*0.130137*	
FW_c	*-0.012412*	*0.0591*
FG_c	*0.011335*	*0.0646*
MT_c	*0.085383*	*0.0086*
$FW_c \times FG_c$	*-0.000760*	*0.6295*
$FW_c \times MT_c$	*-0.009567*	*0.0765*
$FG_c \times MT_c$	*0.007230*	*0.1008*

The significance level (p-value) is a measure of the impact of a term on the response. The smaller the p-value the more significant the term is. As indicated by the smallest p-value, the most significant term is the thickness of the absorbing layer (as expected). A simpler and yet accurate model can be obtained by eliminating some of the terms of the model based on the p-value. The typical criterion for including a term in the

model is that the p-value for that term should be less than or equal to 0.1, leading to less than 1% error in the output. Using this criterion, all of the main effects are retained in the model as well as the interaction between the thickness of the absorbing layer and the finger width. The statistical model equation for the responsivity is:

$$\hat{R} = 0.130137 - 0.012412 \times \frac{FW_a - 1.5}{0.5} + 0.011335 \times \frac{FG_a - 2.5}{0.5} + 0.085383 \times \frac{MT_a - 0.3}{0.2} + 0.0007323 \times \frac{FW_a - 1.5}{0.5} \times \frac{MT_a - 0.3}{0.2}, \quad (4.13)$$

where FW_a, FG_a, and MT_a are the physical values of the input variables. Equation (4.13) can be rewritten in a concise format as:

$$\hat{R} = -0.0174 - 0.02248FW + 0.0227FG + 0.4269MT + (0.0146FW - 0.022) \times (5MT - 0.6667). \quad (4.14)$$

The measured responsivity data from MSM PDs that were not used to construct the statistical model were then compared to the output of Equation (4.14). Table 12 shows the measured and predicted values for these MSM PDs. The average prediction error is 10.35%.

This analysis indicates that the material thickness dominates the responsivity of the MSM PDs, and that the finger width and finger gap have a similar, smaller influence on the responsivity. This is as expected, as the incident optical power is absorbed by the InGaAs material, which decays exponentially from the surface of semiconductor. This was shown in Equation (1.6) in Chapter 1. For the very thin absorbing layer material, only a fraction of the incident optical power is absorbed by the PD absorbing layer, and thus, the responsivity is small. The ratio of finger width to finger gap determines the percentage of the incident optical power reflected. Thus, the finger width and finger gap

are expected to have the same order of significance for responsivity, as are verified by the similarity of the significance level of these two terms.

Table 12: Comparison of measured responsivity with the predicted responsivity by Equation (4.14). The first column lists the MSM PDs in a format of absorbing layer thickness/finger width/finger gap in units of μm.

	Responsivity Measured (A/W)	Responsivity Predicted (A/W)	Prediction Error
PD #1 (0.1/1/1)	0.0355	0.0305	14.01%
PD #2 (0.2/1/1)	0.0789	0.0695	11.94%
PD #3 (0.3/1/1)	0.1044	0.1085	3.93%
PD #4 (0.5/1/1)	0.1603	0.1865	16.43%
PD #5 (0.2/1/2)	0.1056	0.0922	12.68%
PD #6 (0.2/1/3)	0.11485	0.1149	0.48%
PD #7 (0.3/2/3)	0.0964	0.0827	14.22%
PD #8 (0.3/1/2)	0.1473	0.1312	10.9%
PD #9 (0.3/1/3)	0.1654	0.1539	6.97%
PD #10 (0.3/2/2)	0.1212	0.1064	12.24%
PD #11 (0.3/2/3)	0.1435	0.1291	10.07%

4.3 Bandwidth Modeling for Circular MSM PDs Using DOE

The bandwidth analysis for circular MSM PDs includes a 2^4 full factorial analysis of 4 variables on 2 levels. The input variables are finger width from 1 μm to 2 μm, finger gap from 2 μm to 3 μm, detector diameter from 40 μm to 60 μm, and InGaAs absorbing layer thicknesses from 0.1 μm to 0.5 μm, where the smaller physical values were assigned as the low input levels and the larger physical values were assigned as the high

input levels. The statistical analysis for bandwidth was conducted using Rs/Discover for a full factorial DOE.

Table 13 lists the simulated results with least square coefficients and significance of variances for each term and interaction of two terms. The subscript "c" denoted the terms were in coded format where *FW*, *FG*, *S*, and *MT* represent finger width, finger gap, active area diameter, and the material absorbing thickness, respectively. All variables have the units of micrometers.

Table 13: Bandwidth analysis with DOE table for circular MSM PDs.

Term	Coefficients	Significance of variances
Constant	*4.811875*	
FW_c	*-0.044375*	*0.5136*
FG_c	*-1.903125*	*0.0001*
S_c	*-0.399375*	*0.0015*
MT_c	*-0.378125*	*0.0019*
$FW_c \times FG_c$	*-0.016875*	*0.8000*
$FW_c \times S_c$	*0.016875*	*0.8000*
$FW_c \times MT_c$	*-0.004375*	*0.9474*
$FG_c \times S_c$	*0.078125*	*0.2709*
$FG_c \times MT_c$	*-0.095625*	*0.1904*
$S_c \times MT_c$	*-0.006875*	*0.9175*

It is noteworthy that the independent variables with the exception of the finger width have a higher level of significance of variance for smaller values than the interaction terms (combinations of two independent variables). Using a significance of variance cut off of 0.5200 for an estimated error less than 1%, the least square regression equation was calculated as:

$$\hat{BW} = 4.811875 - 0.044375 \times \frac{FW_a - 1.5}{0.5} - 1.903125 \times \frac{FG_a - 2.5}{0.5} - 0.399375 \times \frac{S_a - 50}{10} - 0.378 \frac{MT_a - 0.3}{0.2} + 0.078125 \times \frac{FG_a - 2.5}{0.5} \times \frac{S_a - 50}{10} - 0.095625 \times \frac{FG_a - 2.5}{0.5} \times \frac{MT_a - 0.3}{0.2} \quad (4.15)$$

Combining terms, Equation (4.15) can be simplified as:

$$\hat{BW} = 17.0247 - 0.0888 \times FW - 3.8063 \times FG - 0.0399 \times S - 1.8906 \times MT + (0.15625 \times FG - 0.390625) \times (0.1S - 5) - (0.19125 \times FG - 0.478125) \times (5 \times MT - 0.6667) \quad (4.16)$$

Equation (4.16) was then used to predict the bandwidth of other MSM PDs that were not used in the DOE model construction, as shown in Table 14. The average prediction error was 3.31% for MSM PDs (30 PDs) with variable values that were between the high and low values of the input parameters.

The bandwidths of PDs are determined by the intrinsic transit time and external RC time constants. The significance of variances from the DOE tables indicates that the finger gap is the dominant factor for bandwidth. This implies that the bandwidths of these MSM PDs are transit-time limited. The minimum finger gap used in the DOE modeling is 2 μm, while the absorbing layer thickness varied from 0.1 μm to 0.5 μm. Thus, the lateral distance for photogenerated carriers to travel is much longer than the longitudinal distance. Through the DOE analysis, it is clear that the RC time delay is not as significant as the transit time delay for these MSM PDs to determine the bandwidth. However, the RC time delay may eventually become comparable to the transit time delay if the finger gap is reduced continuously [16].

Table 14: Measured bandwidth compared to the predicted values.

	Bandwidth Measured	Bandwidth Predicted	Prediction Error
PD #1 (0.1/50/1/2)	7.07 GHz	7.04 GHz	0.4%
PD #2 (0.1/50/1/3)	3.43 GHz	3.42 GHz	0.09%
PD #3 (0.1/50/2/2)	7.15 GHz	6.95 GHz	2.75%
PD #4 (0.5/50/2/3)	3.32 GHz	3.33 GHz	0.55%
PD #5 (0.2/40/1/2)	7.03 GHz	7.37 GHz	4.95%
PD #6 (0.2/40/1/3)	3.85 GHz	3.51 GHz	8.79%
PD #7 (0.2/40/2/2)	7.20 GHz	7.28 GHz	1.24%
PD #8 (0.2/40/2/3)	3.14 GHz	3.42 GHz	8.99%
PD #9 (0.2/50/1/2)	6.88 GHz	6.90 GHz	0.29%
PD #10 (0.2/50/1/3)	3.25GHz	3.19 GHz	1.84%
PD #11 (0.2/50/2/2)	6.86 GHz	6.81 GHz	0.70%
PD #12 (0.2/50/2/3)	3.00 GHz	3.10 GHz	3.37%
PD #13 (0.2/60/1/2)	6.52 GHz	6.42 GHz	1.49%
PD #14 (0.2/60/1/3)	2.64 GHz	2.86 GHz	8.67%
PD #15 (0.2/60/2/2)	5.36 GHz	6.33 GHz	18.17%
PD #16 (0.2/60/2/3)	2.70 GHz	2.78 GHz	2.96%
PD #17 (0.3/40/1/3)	3.36 GHz	3.27 GHz	2.54%
PD #18 (0.3/40/2/2)	7.13 GHz	7.14 GHz	0.25%
PD #19 (0.3/40/2/3)	3.06 GHz	3.18 GHz	4.11%
PD #20 (0.3/50/1/2)	6.79 GHz	6.76 GHz	0.45%
PD #21 (0.3/50/1/3)	2.99 GHz	2.95 GHz	1.23%
PD #22 (0.3/50/2/2)	6.13 GHz	6.19 GHz	1.03%
PD #23 (0.3/50/2/3)	2.8 GHz	2.86 GHz	2.30%
PD #24 (0.3/60/1/2)	6.35 GHz	6.28 GHz	1.07%
PD #25 (0.3/60/1/3)	2.53 GHz	2.63 GHz	4.03%
PD #26 (0.3/60/2/2)	6.13 GHz	6.19 GHz	1.03%
PD #27 (0.3/60/2/3)	2.45 GHz	2.54 GHz	3.80%
PD #28 (0.5/50/1/2)	6.65 GHz	6.48 GHz	2.6%
PD #29 (0.5/50/1/3)	2.61 GHz	2.48 GHz	5.0%
PD #30 (0.5/50/2/2)	6.10 GHz	6.39 GHz	4.72%

4.4 Capacitance Modeling for Circular MSM PDs Using DOE

The capacitance statistical model of circular on-wafer MSM PDs include a 2^3 full factorial experiment design with input variables of finger width, finger gap, and active area diameter. The low and high levels are 1 μm and 2 μm for finger width, 2 μm and 3 μm for finger gaps, and 40 μm and 80 μm for the active area diameter sizes. The experiment consisted of 8 runs and is listed in Table 15.

Table 15: The input matrix for Rs/Discover analysis.

Run #	Finger width (μm)	Finger gap (μm)	Size (μm)	Capacitance (fF)
1	1 (-1)	3 (+1)	80 (+1)	107.5
2	2 (+1)	3 (+1)	40 (-1)	35.5
3	1 (-1)	2 (-1)	80 (+1)	143.3
4	2 (+1)	3 (+1)	80 (+1)	121.0
5	2 (+1)	2 (-1)	40 (-1)	42.8
6	1 (-1)	2 (-1)	40 (-1)	35.0
7	1 (-1)	3 (+1)	40 (-1)	44.5
8	2 (+1)	2 (-1)	80 (-1)	160.5

The measured data was entered to Rs/Discover as inputs for the MSM PD analysis and modeling. The simulated results of least square coefficients and the p-value for the significance of variances are listed in Table 16 for individual variables and two-term interactions.

Table 16: Capacitance analysis with DOE table for circular on-wafer MSM PDs.

Term	Coefficients	Significance of variances
Constant	*86.2*	
FW_c	*3.75*	*0.1134*
FG_c	*46.75*	*0.0371*
S_c	*-11.575*	*0.0092*
$FW_c \times FG_c$	*4.05*	*0.8834*
$FW_c \times S_c$	*-0.125*	*0.1051*
$S_c \times FG_c$	*-7.375*	*0.0581*

As shown from Table 16, the most significant term affecting the value of the capacitance is the size of the MSM PDs, which agrees with empirical analysis. The least square regression equation for capacitance with the calculated coefficients by Rs/Discover is shown as:

$$\hat{cap} = 86.2 + 3.75 \times \frac{FW-1.5}{0.5} + 46.75 \times \frac{FG-2.5}{0.5} - 11.575 \times \frac{S-60}{20} + 4.05 \times \frac{FW-1.5}{0.5} \times \frac{FG-2.5}{0.5} - 0.125 \times \frac{FW-1.5}{0.5} \times \frac{S-60}{20} - 7.375 \times \frac{FG-2.5}{0.5} \times \frac{S-60}{20}, \quad (4.17)$$

Combining terms, Equation (4.17) can be simplified as:

$$\hat{cap} = -7.425 + 7.5FW - 23.15FG - (0.25FW - 0.375)(FG - 5) + (8.1FW - 12.15)(0.05S - 3) - (0.37S - 22.125)(2FG - 5). \quad (4.18)$$

Equation (4.18) was then used to predict the capacitance of other MSM PDs that were not used in the model construction, as shown in Table 17. The average prediction error is 7.8% using the DOE calculation. The capacitance is also calculated using the conformal mapping method described in Chapter 1, which gives an average prediction error of 25.3%. The prediction of capacitance using the DOE method is thus much more accurate than the conformal mapping method.

Table 17: The measured capacitance in comparison to the predicted values.

PD # (size/finger width/gap)	Capacitance Measured (fF)	Capacitance Predicted by DOE (fF)	DOE Prediction Error	Conformal mapping Prediction (fF)	Conformal mapping calculation error
PD #1 (40/1/1)	59.7	51.9	12.9%	53.4	10.5%
PD #2 (50/1/1)	83	84.4	1.08%	76.9	7.3%
PD #3 (50/1/2)	64.5	68.9	6.8%	40.1	31.7%
PD #4 (50/1/3)	52	53.3	2.57%	26.1	49.7%
PD #5 (50/2/2)	66.5	72.6	9.17%	38.4	30.7%
PD #6 (60/1/1)	130.3	116.8	10.3%	114.9	11.8%
PD #7 (60/1/2)	84	93.9	11.8%	59.9	28.7%
PD #8 (60/1/3)	75.7	71	6.2%	39.1	48.3%
PD #9 (60/2/2)	106	101.7	9.6%	57.4	29.1%
PD #10 (80/1/1)	197.5	181.6	8.03%	186.2	5.7%

CHAPTER 5

I-MSM TESTING RESULTS

A variety of thin film circular I-MSM PDs were fabricated and bonded onto glass substrates for measurements. The fabrication and integration details were given in Chapter 2. Ti (300Å)/Au (3000Å) metallization was used for I-MSM electrodes and Ti (300Å)/Au (3500Å) for the probing pads. The thick probing pads metallization was designed for multiple probes. The I-MSM PDs were characterized for dark current, responsivity, impulse response, bandwidth, and capacitance. The correlation of I-MSM PDs to on-wafer MSM PDs will be reported in the next chapter. I-MSM PDs studied in this Chapter have varying finger widths (1 to 2 μm), finger spacings (1 to 2 μm), active area diameters (20 to 80 μm), and material thicknesses (1000 to 5000 Å).

5.1 Dark Current and Responsivity

5.1.1 Dark Current Measurements

The dark currents of MSM PDs were defined by the Schottky contact to the InAlAs cap layer. The Schottky barrier height of Au to 30 nm InAlAs on bulk n type InGaAs is reported to be 0.5 to 0.55 eV [43, 44]. The increase of InAlAs layer thickness will increase the Schottky barrier height, and leads to a reduction of the dark current. For the same InAlAs thickness, the dark current of on-wafer MSM PDs was roughly proportional to the metallization area of PDs, which was discussed in Chapter 3. Dark currents for I-MSM PDs on material 219 with 40 nm InAlAs and 109 with 30 nm InAlAs are reported

in Table 18. Multiple samples (2 to 6 samples) were fabricated and measured to use average dark currents.

Table 18: Dark current of I-MSM PDs on material 219 and 109.

Material (InAlAs layer thickness)	Active area diameter/finger width/spacing (μm)	Dark current (nA)
219 (InAlAs 400 Å)	D80/1/1	9.8 nA
	D80/1/2	6.4 nA
	D80/1/3	1.5 nA
	D80/2/2	6.1 nA
	D60/1/1	7.55 nA
	D40/1/1	4.4 nA
109 (InAlAs 300 Å)	D80/1/1	81.3 nA
	D60/1/1	28.7 nA

5.1.2 Responsivity Measurements

The photocurrents of I-MSM PDs were measured with a single mode fiber at a wavelength of 1.55 μm. The responsivity measurement was calibrated using a Newport Multi-Function Optical Meter 1835-C in conjunction with a Newport 818-IG broadband photodetector. Figure 18 plots the photocurrent of I-MSM PDs fabricated on material 219 (3000 Å absorbing layer) for varying finger widths and spacings as a function of voltage bias. The measured responsivity at a 5 V bias for PDs with finger width/spacing of 1/1, 1/2, 1/3, 2/2 μm is 0.1524, 0.1651, 01612, and 0.1510 A/W, respectively. The responsivity is similar for all I-MSM PDs despite the differences in finger width and spacing. This result agrees with expectation, since all of the PDs have the same absorbing

layer thickness with back side illumination (with complete elimination of the finger shadowing effect).

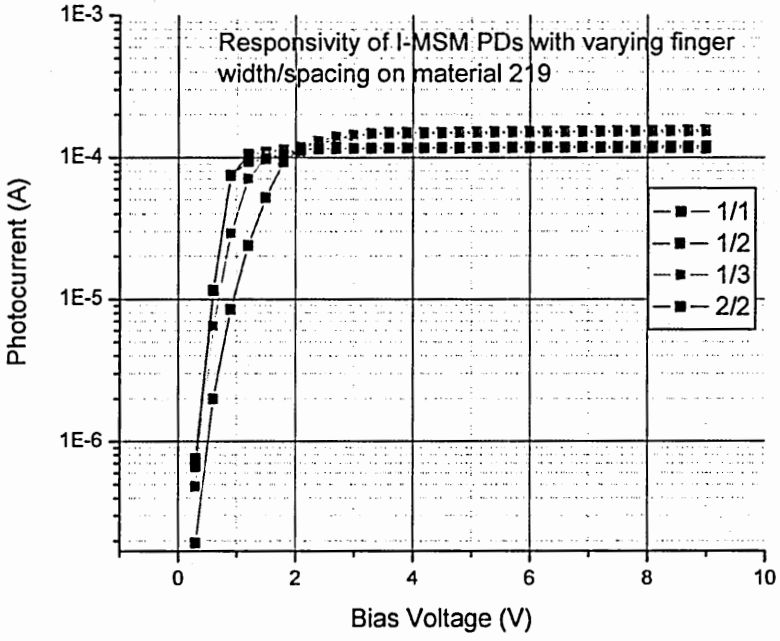

Figure 18: Responsivity of I-MSM PDs with varying finger width/spacing (μm) as a function of bias voltage from 0 V to 9 V.

In addition to the responsivity plots with varying finger width and spacing, the responsivity of the I-MSM PDs was also investigated as a function of material thickness, and the results are shown in Figure 19. The responsivity for I-MSM PDs with absorbing layer thickness of 1000 Å, 2000 Å, 3000 Å, and 5000 Å are 0.05392, 0.1319, 0.1524, and 0.2673 A/W, respectively, at 5 V bias. This increase in responsivity with increasing absorbing layer thickness is in good agreement with the responsivity analysis of on-wafer MSM PDs. The quantitative correlation analysis will be presented in the next chapter.

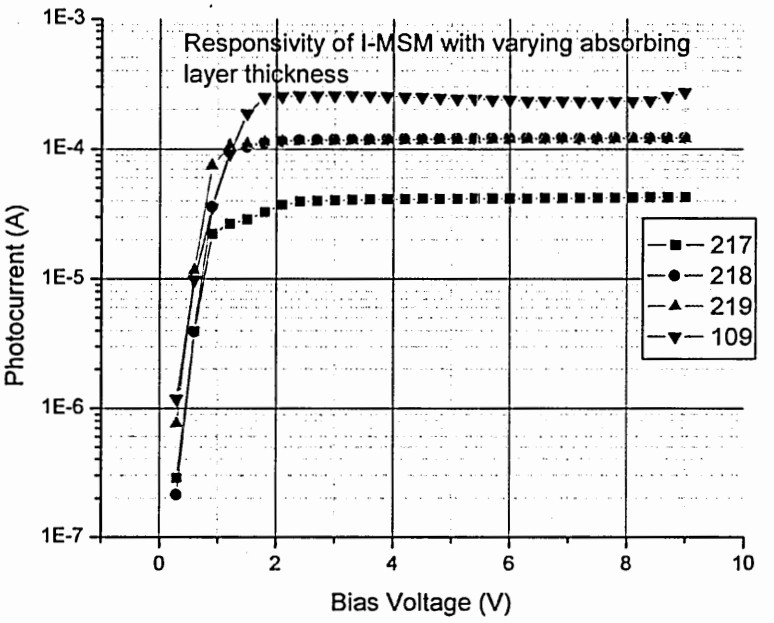

Figure 19: Photocurrent of I-MSM PDs of 1/1 μm with varying absorbing layer thickness.

5.2 Impulse Response

The impulse response was investigated as a function of finger width, finger spacing, active area size, voltage bias, and absorbing layer thickness. The same measurement setups were used as those for on-wafer MSM PDs.

5.2.1 Impulse Response at Varying Bias Voltages

The impulse response of the I-MSM PDs compressed with increasing bias voltage. As shown in Figure 20 for the InGaAs carrier velocity plot [45], the drift velocity of electrons increases linearly with voltage at low bias, then decreases dramatically with further increase in voltage, while the drift velocity of holes increases monolithically with voltage until it is saturated at high bias. In Figure 21, a plot is given for PDs with finger

width/spacing of 1/1 μm on material 219 at biases from 2 V to 11 V. The impulse response of I-MSM PDs with wider finger widths and spacings on other materials displayed similar voltage dependent characters. The tail of the impulse is compressed significantly with increasing bias voltage and displays no significant difference for bias higher than 9 V.

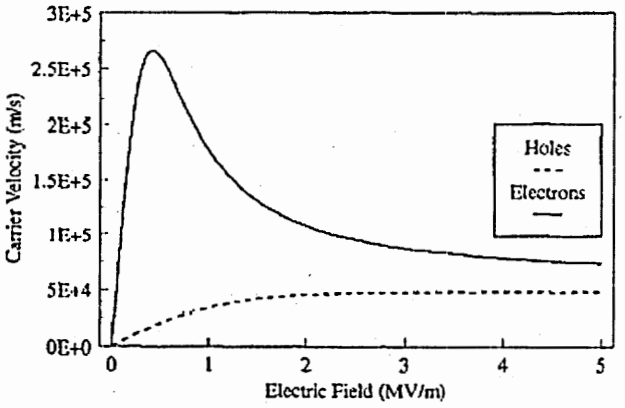

Figure 20: The carrier velocity of electrons and holes in InGaAs as a function of electric field after Bowers et al [45].

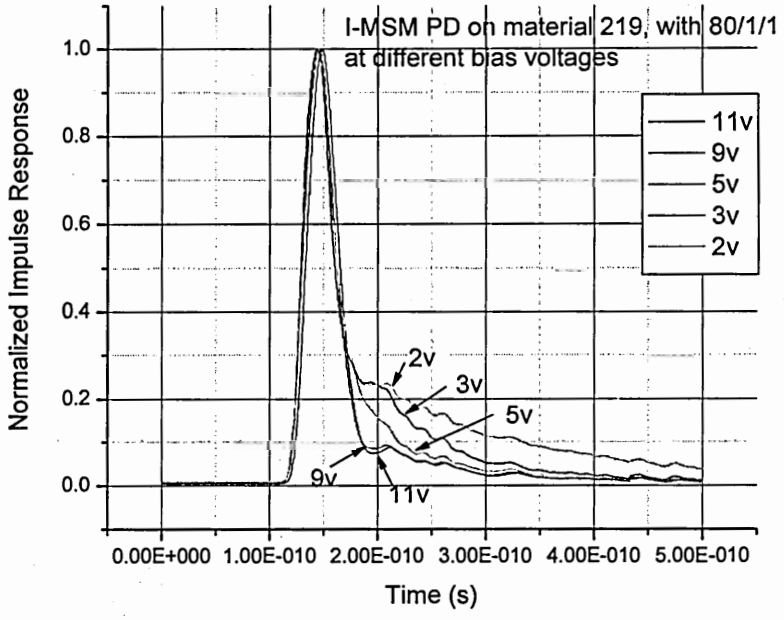

Figure 21: Impulse response of I-MSM PDs with 1 μm finger spacing at different biases.

5.2.2 Impulse Response with Varying Finger Width and Spacing

The measured results of MSM PD impulse response with varying finger widths and spacings are plotted in Figure 22. The impulse response for 1/1 μm devices is much more compressed than that of other PDs with wider finger spacings. It is clear that these PDs are transit-time limited rather than capacitance limited because wider finger spacings result in smaller capacitance. The I-MSM with finger width/spacing with 1/2 μm has a better impulse than the I-MSM with 1/3 μm, and the 2/2 μm finger width/spacing has the slowest impulse response. This is different from the impulse measurement of on-wafer MSM PDs, of which the 2/2 μm device had a better impulse than the 1/3 μm device. The slow behavior of the 2/2 μm device is due to a high percentage (50%) of carriers generated behind the electrodes where the electric field is the weakest. A detail

discussion of impulse correlation of I-MSM PDs to on-wafer MSM PDs will be presented in the next chapter.

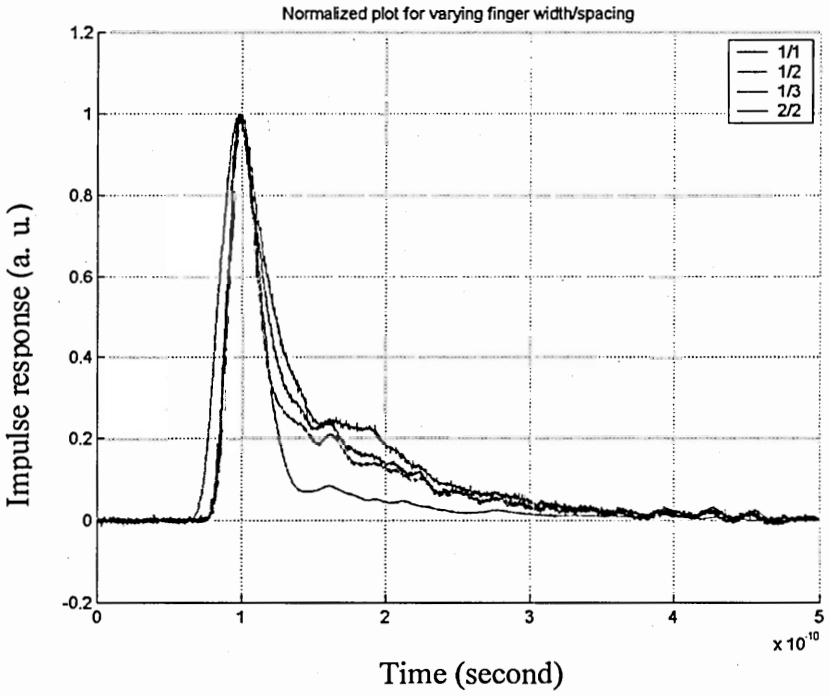

Figure 22: Normalized impulse response of I-MSM PDs on material 219 with 80 μm diameter absorbing area.

5.2.3 Impulse Response with Varying Active Area Size

I-MSM PDs with varying active area size were investigated to ascertain the effect of the RC time constant on impulse response. Figure 23 plots the impulse response of PDs with active area diameters of 80 μm, 60 μm, and 40 μm.

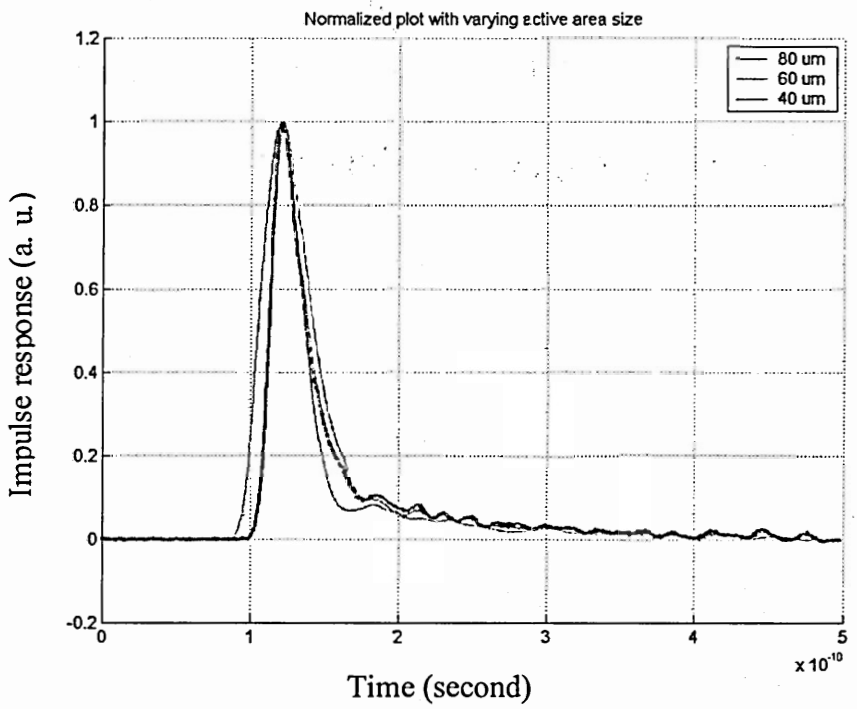

Figure 23: The impulse responses of I-MSM PDs on material 219 with 1 μm finger spacing and varied active area diameter from 40 μm to 80 μm.

From Figure 23, it can be seen that the impulse responses are similar for all three PDs despite the difference in active area size. Table 19 lists the pulse width (FWHM) and fall time (tail length from 90% to 10%) of these three I-MSMs. The PD with 40 μm active area diameter has a slightly compressed tail length and narrower FWHM than the other PDs. The lack of difference in the impulse response due to the difference in active area demonstrates again that the transit time is the dominant factor in these devices, and not the RC time constant for determining the speed performance of these PDs.

Table 19: The pulse width and fall-time of I-MSM PDs with varying active area size.

	Pulse width (FWHM)	Fall time (tail length)
Active area of 80 μm	30 ps	53 ps
Active area of 60 μm	31 ps	47 ps
Active area of 40 μm	27 ps	46 ps

5.2.4 Impulse Response with Varying Absorbing Layer Thickness

I-MSM PDs with thin absorbing layers can lead to faster speed response by shortening the transit distance. However, the thin absorbing layer will reduce the responsivity of the photodetectors. In Figure 24 below, the impulse responses of four I-MSM PDs on material 109, 219, 218 and 217 at a bias of 9 V are plotted. All these PDs were 1/1 μm finger width and spacing with 60 μm diameter active area. It is clear from the plot that the responsivity decreases with the reduction in absorbing layer thickness, which is exhibited as a reduced peak and integrated area underneath the impulse.

In Table 20, the pulse width (FWHM) and tail length are listed for the four I-MSM PDs. All I-MSM PDs have similar FWHM and tails except the one fabricated on material 109 (5000 Å InGaAs). The similarity again demonstrates that the size (capacitance) is not the dominant factor in the speed performance of the I-MSM PDs. This measurement results agrees with the statistical analysis of bandwidth for on-wafer MSM PDs in Chapter 4. The I-MSM PDs on material 109 has a better impulse than the other materials. This could be explained due to the fact that the width precision of narrow (1 μm) fingers is much more variable using contact photolithography than is the precision of wider fingers. Compared to MSMs with finger spacings of 2 μm and 3 μm, the I-MSM PDs with 1 μm spacing demonstrates a much better speed response on all of the materials.

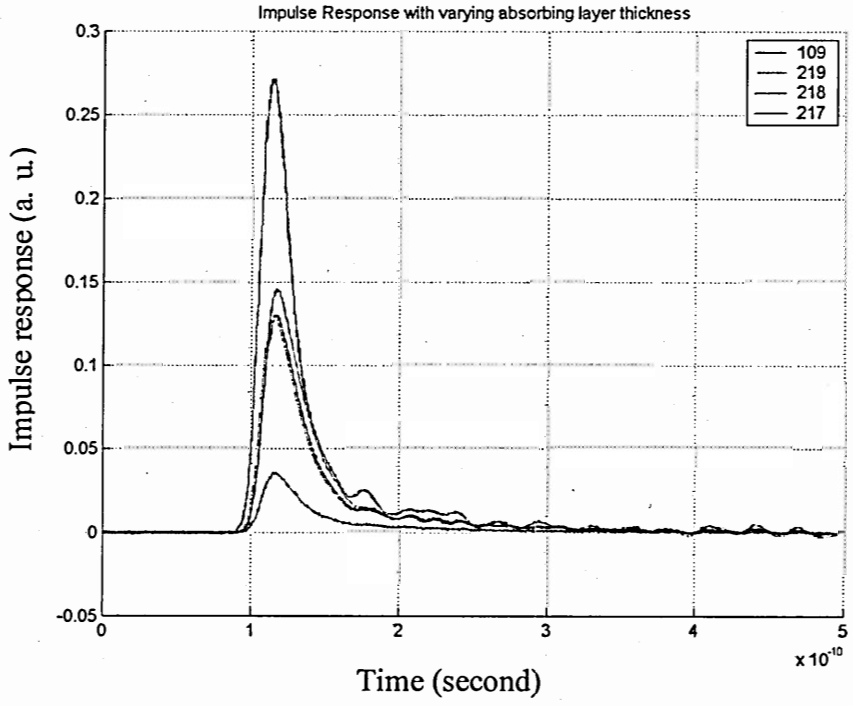

Figure 24: Impulse response of I-MSM PDs on varying absorbing layer thickness.

Table 20: The pulse width and tail length of I-MSM PDs with varying absorbing layer thickness and 1/1 μm finger widths and spacings.

	FWHM	Tail length
I-MSM PD with 5000 Å InGaAs	24.5 ps	38.5 ps
I-MSM PD with 3000 Å InGaAs	31 ps	46 ps
I-MSM PD with 2000 Å InGaAs	30 ps	46.5 ps
I-MSM PD with 1000 Å InGaAs	27 ps	47 ps

5.3 Bandwidth

The bandwidth of the MSM PDs is related to the impulse response by a Fourier transform from the time domain to the frequency domain. Therefore, the measured bandwidth results should be consistent with the measuring impulse response. The bandwidth measured herein is the scatter matrix component of s21 (optical to electrical)

using the LCA. The bandwidth of the I-MSM PDs is high for PDs with 1μm finger spacing, and decreases for wider finger spacings. These transit-time limited characteristics also account for the increase in bandwidth with the increase in voltage bias. Figure 25 plots the bandwidth of I-MSM PDs of 80 μm diameter active area on material 219 with varying finger width/spacing. These large size MSM PDs avoid fiber misalignment.

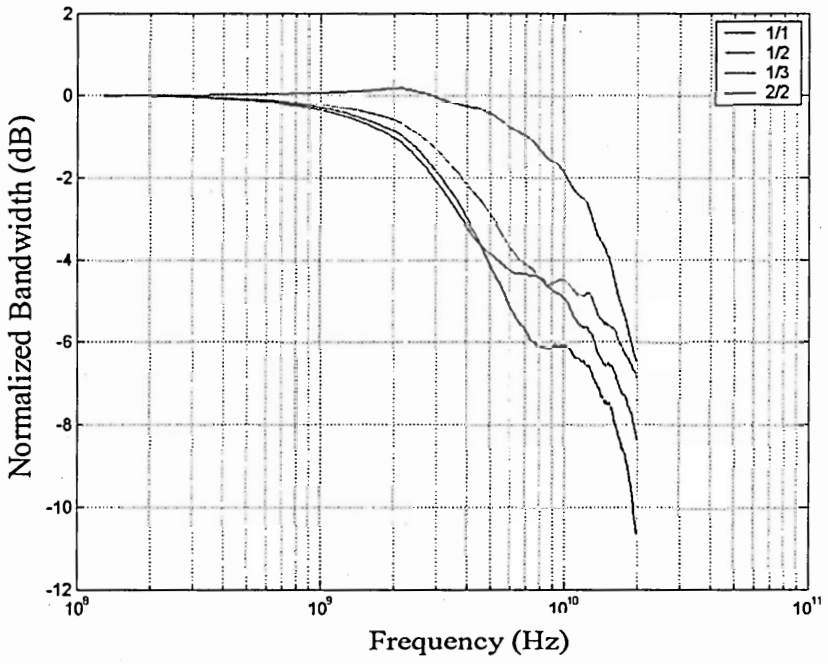

Figure 25: Bandwidth as a function of finger width and spacing for I-MSM PDs with an 80 μm active area.

The –3db frequency for finger width and spacing of 1/1 μm, 1/2 μm, 1/3 μm, and 2/2 μm are 13.16 GHz, 5.14 GHz, 4.04 GHz, and 3.85 GHz, respectively. The I-MSM PD with wider spacing has lower bandwidth because the electrical field is weaker compared to those with narrower finger spacings. The finger width/spacing of the 2/2 μm

device results in a smaller bandwidth than the 1/2 μm device because more carriers are generated underneath the electrodes, and these carriers must diffuse to the high electrical field region first, and then travel at saturation velocity. The bandwidth measurement clearly implies that the narrower finger width for I-MSM PDs results in higher bandwidth.

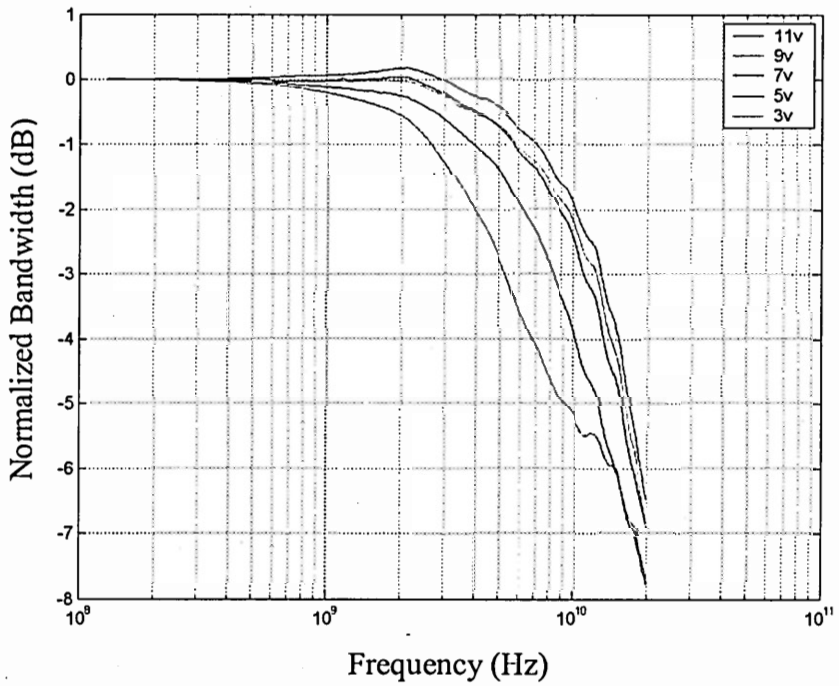

Figure 26: The voltage dependence of bandwidth for I-MSM PD with 1/1 finger width/spacing on material 219 (3000 Å InGaAs). The PD has a size of 80μm diameter of active area.

The voltage dependant bandwidth behavior is shown in Figure 26 for I-MSM PDs with 1/1 finger width/spacing on material 219. The –3db frequency of the I-MSM PD (1 μm finger spacing) at a voltage bias of 11 V, 9 V, 7 V, 5 V and 3 V are 13.2 GHz, 12.5 GHz, 11.08 GHz, 8.2 GHz, and 5.3 GHz, respectively. The bandwidth only increased slightly at biases higher than 7 V, indicating that most photogenerated carriers could drift at their saturation velocity at this electrical field strength. Therefore, for finger

width/spacing of 1/1 μm with 3000 Å absorbing layer thickness, a bias voltage of 7 V is high enough to have the I-MSM PD saturate in speed performance.

The bandwidth doesn't change much with the absorbing layer thickness from 5000 Å to 1000 Å for PDs with finger spacings of 1 μm since the lateral transit distance between fingers is more than 2 times longer than the longitudinal transit distance for carriers. This measurement results agrees with the measured impulse response. To further increase the bandwidth of the I-MSM PDs and maintain good responsivity, the reduction of finger spacing is the right approach. However, the increase of finger density per unit area will increase the capacitance of the PD. Therefore, there is an optimized value of the finger spacing for a target speed.

5.4 Capacitance

The s-parameters of I-MSM PDs were measured using a HP lightwave component analyzer. The capacitance was then calculated from s-parameters in the frequency range from 130 MHz to 20 GHz. The capacitance was studied for PDs with the same finger/gap structure but on different materials, as shown in Table 21. The slight difference in capacitance values with varying absorbing layer thickness indicates that the capacitance of the PDs is nearly independent of material thickness. The capacitance is also investigated for PDs with varying active area size, and finger spacing as shown in Table 22. It is clear that the capacitance goes up with an increase in active area size and an increase in finger pairs per unit area.

Table 21: Capacitance values with material thickness of I-MSM PDs.

Active area diameter	Finger width/spacing	Material thickness	Capacitance
60 μm	1/1 μm	5000 Å	130 fF
60 μm	1/1 μm	3000 Å	131.5 fF
60 μm	1/1 μm	1000 Å	131 fF

Table 22: Capacitance of I-MSM PDs with varying finger width/spacing and active area size.

Active area diameter	Finger width/spacing	Material thickness	Capacitance
80 μm	2/2 μm	3000 Å	150 fF
80 μm	1/1 μm	3000 Å	199 fF
60 μm	1/1 μm	3000 Å	131.5 fF
40 μm	1/1 μm	3000 Å	62.5 fF

The measured results for dark current, responsivity, bandwidth, and capacitance for I-MSM PDs are reported in this Chapter. The dark currents of the majority of the I-MSMs are 10 nA or less except the PDs fabricated from material 109, with a 300 nm cap layer. The responsivity of the I-MSM PDs are reported for voltage biases from 0 to 9 V, and the maximum responsivity of 0.2673 A/W was achieved for the I-MSM on material 109. The AC characteristics of the I-MSM PDs are reported as a function of finger width, finger spacing, absorbing layer thickness, absorbing area, and bias voltage. The measured results suggests that these MSM PDs are transit time limited. The capacitance of the I-MSM PDs are measured in this Chapter for varying material thickness, finger width/spacing, and absorbing area. The maximum tested capacitance of 199 fF was for

the PD with 80 μm diameter and 1/1 μm finger/width. Detailed analysis and modeling of both DC and AC characteristics of I-MSM PDs will be reported in the next chapter.

CHAPTER 6

CORRELATION OF I-MSM PDS TO ON-WAFER MSM PDS

The purpose of this Chapter is to try to correlate on-wafer MSM PD measurement results to I-MSM PD results. Since I-MSMs are advantageous from a responsivity point of view, they are often a preferred implementation. However, on-wafer MSMs are much easier to fabricate than I-MSMs. Thus, if a certain specification for I-MSMs must be met, and some experiments need to be conducted to fabricate appropriate devices, if MSMs can be fabricated and tested to predict I-MSM device performance, this would be of greet interest.

6.1 Correlation of DC Characteristics

6.1.1 Comparison of Dark Current of I-MSM PDs to On-Wafer MSM PDs

Dark currents of MSM PDs are determined by the Schottky barrier height of the semiconductor to Au contact. Compared to the on-wafer MSM PD process, additional fabrication steps (mesa etch and substrate removal) were added for I-MSM fabrication. Mesa etching utilized photoresist as a mask and separates each individual detector using chemical etching through the absorbing layer. In substrate removal, the electrodes of the MSM PDs were protected by Apiezon Wax from the HCl etchant. In the ideal situation, the mesa etch and substrate removal steps do not alter the physics of the contact of the electrodes to the semiconductor. Thus, the dark current of I-MSM PDs should be the same as on-wafer MSM PDs. In Table 23, dark currents for PDs with 80 μm active areas

with 1/1, 1/3, and 2/2 μm finger widths and spacings for I-MSM PDs were compared to on-wafer MSM PDs. Multiple samples (2 to 6 samples) were fabricated and measured to report an average dark current for each I-MSM PD structure.

Table 23: Dark currents of I-MSM PDs in comparison to on-wafer MSM PDs.

Diameter/finger width/finger spacing	80/1/1 μm	80/1/3 μm	80/2/2 μm
I-MSM PDs	9.8 nA	1.5 nA	6.1 nA
On-wafer MSM PDs	5.2 nA	1.2 nA	2.2 nA

The dark currents of the I-MSM PDs are slightly higher than on-wafer MSM PDs. This is probably due to the mesa etch process. The mesa etch mask for the I-MSM PDs was designed with a slightly larger size than the finger area, but no protection mask for the metal contact, as shown in Figure 27. The absence of mask protection for the metal contact of the I-MSM PD was designed for ease of alignment of the I-MSM PD onto the host substrate metal contact, with the clear shape contour viewed from backside.

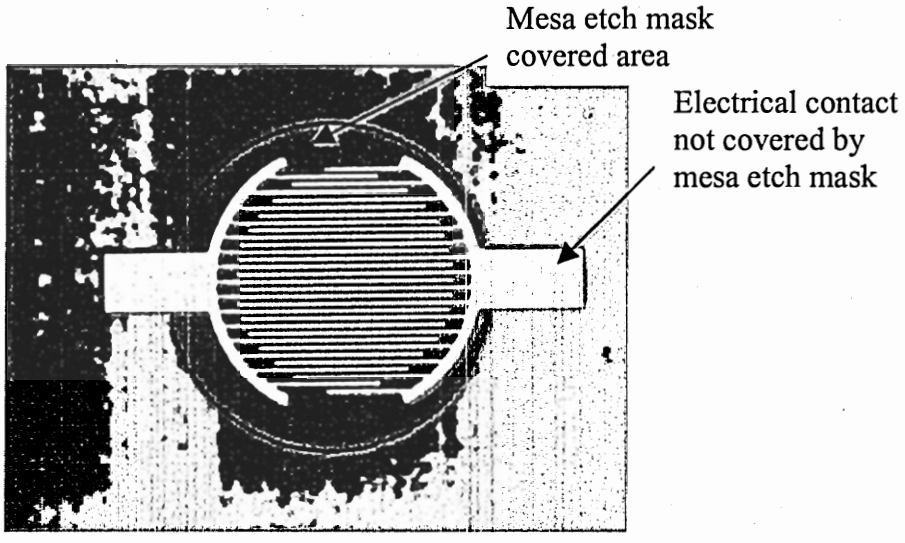

Figure 27: An individual photodetector after mesa etch.

6.1.2 Correlation of Responsivity

Back illumination of MSM PDs is an effective way to improve the device responsivity by eliminating the finger shadowing effect [46]. In Chapter 1, the quantum efficiency, as discussed in Equation (1.4), was determined by the percentage of shadowing area, reflection from the surface, and absorbing layer thickness. It is usually an effective assumption for high quality materials that the internal quantum efficiency η_i is 100% for conversion from absorbed photons to electron-hole pairs. The responsivity R at one wavelength, given the definition in Equation (1.3), is:

$$R = \frac{I_{ph}}{P_{opt}} = \frac{nq}{P_{opt}}, \tag{6.1}$$

where n is total number of photogenerated carriers. Therefore, the ratio of responsivity of on-wafer MSM PDs to I-MSM PDs can be written as:

$$\frac{R_{imsm}}{R_{omsm}} = \frac{n_i \times q / P_{opt}}{n_o \times q / p_{opt}} = \frac{n_i}{n_o} \tag{6.2}$$

where R_{omsm} and R_{imsm} are responsivity of on-wafer MSM PDs and I-MSM PDs, respectively, and n_o and n_i are the number of photogenerated carriers inside the absorbing layer of the on-wafer MSM and I-MSM, respectively. Figure 28 provides a schematic plot of MSM PD structure to illustrate the two illumination situations. For on-wafer MSM PDs, part of the optical power is lost due to the reflection from the opaque metal electrodes, and a fraction of light also experiences partial reflection from the air/semiconductor (InAlAs) interface. For I-MSM PDs, the partial reflection of the input power takes place at the air/InAlAs interface.

$In_{0.52}Al_{0.48}As$ has a similar lattice constant (5.8672 Å) as $In_{0.53}Ga_{0.47}As$ (5.8687 Å), but much wider bandgap (1.450 eV). The cutoff wavelength for InAlAs is 855 nm, which means that the InAlAs layer is transparent to light of wavelength from 1.3 μm to 1.55 μm. The refractive index for InAs and AlAs are 3.52 and 3.17, respectively. The refractive index of $In_{0.52}Al_{0.48}As$ is calculated from interpolating parameters of binary alloy, and the calculated refractive index is 3.35. At normal incidence, the reflectivity r_0 at air/semiconductor interface is

$$r_0 = \left(\frac{n-n'}{n+n'}\right)^2 = \left(\frac{1-3.35}{1+3.35}\right)^2 = 0.2918, \tag{6.3}$$

where n and $n`$ are the refractive indices of air and InAlAs.

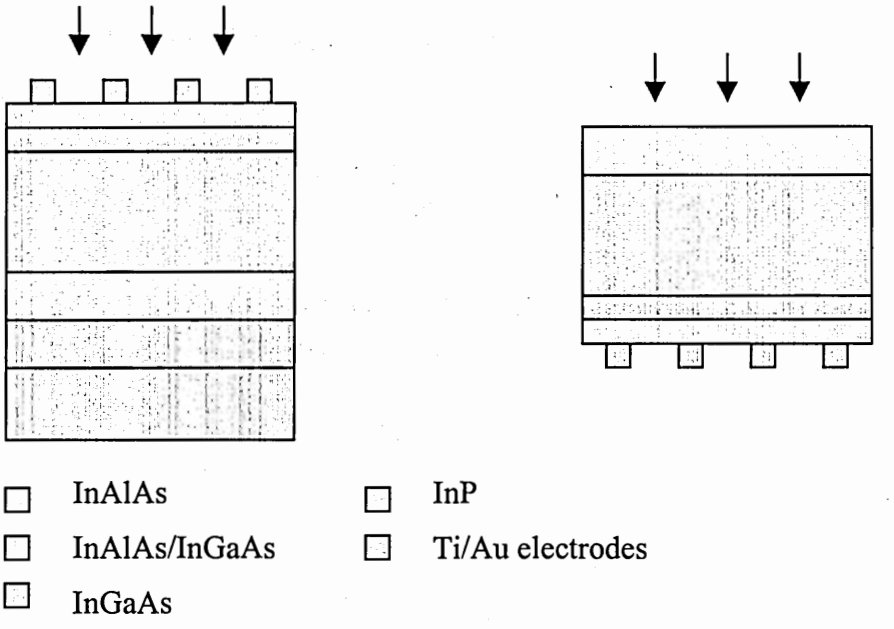

Figure 28: Schematic of on-wafer MSM PDs and I-MSM PDs with normal incidence illumination.

The incident optical power decays exponentially inside the material. In MSM front illumination, part of the incident wave is reflected by the electrodes and only part of the incident wave penetrates into the absorbing material through the cap layer (InAlAs). The InAlAs refractive index (3.35) is very similar to the refractive index of InGaAs (3.76), leading to a reflectivity of 0.0033 at the InAlAs/InGaAs interface. This reflection is considered negligible. The optical wave which is not absorbed in the absorbing layer will be absorbed by the stop-etch layer (2000 Å InGaAs), as shown in Figure 28. The on-wafer MSM PDs were mounted on black wax on a glass substrate. The optical wave which is not absorbed by the stop-etch layer will continue to propagate and eventually will be absorbed by the black wax. The reflection from the substrate is neglected. Carriers generated in the stop-etch layer will not be collected by the electrodes because the wide

bandgap InAlAs will present a barrier to the drift of carriers at moderate bias voltages. Therefore, the total power absorbed by the absorbing layer for an on-wafer MSM is

$$P_{omsm} = (1-r_0)\frac{g}{g+w} \times P_{opt} \times (1-e^{-\alpha T_x}), \tag{6.4}$$

where the subscript of "omsm" is a notation for on-wafer MSM PDs, T_x is the thickness of the absorbing layer, and r_0 is the reflectivity of air to InAlAs layer.

The optical power absorption for I-MSM PDs is rather complex. Usually, uniform illumination is assumed for uniform generation of carriers across the whole area. For I-MSM PDs, the optical power is partially reflected at the buffer layer (InAlAs) first, then penetrates into the absorbing layer. The optical power absorbed by the InGaAs layer , P_{imsm}', can be expressed as:

$$\begin{aligned} P_{imsm}' &= (1-r_0)P_{opt}e^{-\alpha T_x} \\ &= P_0 e^{-\alpha T_x} \end{aligned}, \tag{6.5}$$

where P_0 is the optical power just inside the semiconductor layers. The optical power which is not absorbed by the absorbing layer will be reflected at the semiconductor-air interface between fingers or reflected at the semiconductor-metal electrodes interface as illumination behind the fingers. The reflection between fingers (at the semiconductor/air interface) will be analyzed first. The optical power reflected back into the InGaAs layer from the semiconductor/air interface is r_0P_1, where P_1 is the optical power between the fingers. The reflected wave will be absorbed again by the absorbing layer and the power not absorbed in the second absorption pass will be reflected at the semiconductor (buffer layer)/air interface on the opposite side. The total absorbed optical power between electrodes with multiple absorption and reflection is

$$P_{tl} = P_0(1-e^{-\alpha T_x}) + r_1 P_0 e^{-\alpha T_x}(1-e^{-\alpha T_x}) + r_1^2 P_0 (e^{-\alpha T_x})^2 (1-e^{-\alpha T_x}) + \ldots$$
$$= P_0(1-e^{-\alpha T_x}) \times (1 + r_1 P_0 e^{-\alpha T_x} + (r_1 P_0 e^{-\alpha T_x})^2 + \ldots) \quad , \tag{6.6}$$

where P_{tl} is the total optical power absorbed in the areas between fingers. The first term in Equation (6.6) is the first order absorption, and the second term is the second absorption of the reflected optical wave, and so on. Equation (6.6) can be simplified as a sum of polynomials:

$$P_{tl} = P_0 \times (1-e^{-\alpha T_x}) \times \frac{1}{1-r_1 e^{-\alpha T_x}} . \tag{6.7}$$

By substituting in Equation (6.5), Equation (6.7) can be rewritten as:

$$P_{tl} = (1-r_0) \times \frac{g}{g+w} \times P_{opt} \times (1-e^{-\alpha T_x}) \times \frac{1}{1-r_1 e^{-\alpha T_x}} . \tag{6.8}$$

The reflection at the metal electrodes for illumination behind the fingers is similar to that at the semiconductor/metal interface. The metallization of electrodes for the I-MSM PDs is Ti (300Å)/Au (3000Å) in this work. The refractive index of the metal electrodes (Ti/Au) has a large imaginary component, which will cause heavy absorption in the metal. The complex refractive index is defined as:

$$\tilde{n} = n - ik \tag{6.9}$$

At an incident wavelength of 1.55 μm, the real part (n) and the imaginary part (k) of Ti are 3.67 and 4.61 [47], respectively. The real part of the refractive index of Ti is very close to the index of InGaAs, so there is only a very small amount (less than 0.1%) of light reflected by the Ti layer. Au is a good metal reflector and the calculated and measured reflectivity of an Au mirror to λ = 1.55 μm is ~ 0.9 [48]. The high reflectivity of Au comes from the small component of the real refractive index (0.18) [47]. The reflected

optical power from the metal structure with a round trip attenuation inside the Ti layer is calculated as:

$$\begin{aligned} P_{out} &= P_{in} \times \exp(-2 \times T_{Ti} \times \tfrac{4\pi k}{\lambda_0}) \times r_{Au} \\ &= P_{in} \times \exp(-2 \times 30nm \times \tfrac{4\pi 4.61}{1550nm}) \times 0.9, \\ &= 0.09557 P_{in} \end{aligned} \tag{6.10}$$

where r_{Au} is the reflectivity of Au, T_{Ti} is the thickness of Ti layer, the P_{in} and P_{out} are the incident optical power and the reflected optical power from the electrodes, respectively. So the effective reflectivity from the Ti/Au layer is 0.09557. The reflectivity at the metal layer is so small that only the first and second absorption passes are considered. Thus, the total absorbed optical power for illumination behind the electrodes is

$$P_{t2} = (1 - r_0) \times \frac{w}{g+w} \times [(1 - e^{-\alpha T_x}) + r_m e^{-\alpha T_x}(1 - e^{-\alpha T_x})] Popt, \tag{6.11}$$

where r_m is the effective refractive index of the Ti/Au metal electrodes (0.09557). Combining Equation (6.11), (6.7) and (6.8), the total absorbed optical power inside the absorbing layer for I-MSM PDs is

$$P_{imsm} = P_{t1} + P_{t2} = (1 - r_0) \times (1 - e^{-\alpha T_x}) \times \left[\frac{g}{g+w} \times \frac{1}{1 - r_0 e^{-\alpha T_x}} + \frac{w}{g+w} \times (1 + r_m e^{-\alpha T_x}) \right] \times P_{opt}. \tag{6.12}$$

The number of carriers collected in the electrodes is proportional to the optical absorption if the internal quantum efficiency is 100%. By substituting Equation (6.4) and (6.12) into Equation (6.2), the ratio of responsivity for I-MSMs to on-wafer MSMs can be written as:

$$\frac{R_{imsm}}{R_{omsm}} = \frac{P_{imsm}}{P_{omsm}} = \frac{\frac{g}{g+w}\left(\frac{1}{1 - r_0 e^{-\alpha T_x}}\right) + \frac{w}{g+w}\left(1 + r_m e^{-\alpha T_x}\right)}{\frac{g}{g+w}}. \tag{6.13}$$

For PDs with a thick absorbing layer, most of the optical power is absorbed during the first propagation pass through the InGaAs absorbing layer, so the reflected wave is small. In such a case, both $r_0 e^{-\alpha Tx}$ and $r_m e^{-\alpha Tx}$ are approximately zero, so Equation (6.13) can be simplified as:

$$\frac{R_{imsm}}{R_{omsm}} = \frac{g+w}{g}. \tag{6.14}$$

The responsivity correlation of I-MSM PDs (R_{imsm}) to on-wafer MSM PDs (R_{omsm}) and the prediction errors are calculated and tabulated in Table 24. The responsivities of PDs were measured under illumination at wavelength of 1.55 μm. The average correlation error is 6.24 %.

Table 24: The correlation of calculated responsivity of I-MSM PDs to measured responsivity.

Material (absorbing layer thickness)	Finger Width/ gap	On-wafer PDs (measured)	I-MSM PDs (measured)	I-MSM PDs (correlation prediction)	Correlation prediction error
109 (5000 Å)	1/1	0.1394	0.2673	0.2788	4.3%
219 (3000 Å)	1/1	0.07951	0.1524	0.15902	4.3%
	1/2	0.1006	0.1651	0.1509	8.6%
	1/3	0.1155	0.1612	0.1540	4.5%
	2/2	0.08141	0.1510	0.16282	7.8%
218 (2000 Å)	1/1	0.05859	0.1319	0.1423	7.9%
217 (1000 Å)	1/1	0.02323	0.05392	0.05734	6.3%

6.2 Correlation of AC Characteristics

The bandwidth of PDs can be obtained through Fourier transform of the impulse response from the time domain to the frequency domain. So the correlation of the AC characteristics of I-MSM PDs to on-wafer MSM PDs will focus on impulse response and capacitance.

6.2.1 Correlation of Impulse Response

The impulse response of an I-MSM PD in comparison to an on-wafer MSM PD at a bias of 9 V is shown in Figure 29. Both the on-wafer PD and I-MSM PD had an active diameter of 80 μm with finger width and spacing of 1/1 μm and 1/2 μm and were fabricated on material with a 3000 Å absorbing layer. The impulse response of the I-MSM has a wider FWHM and a longer tail than the on-wafer MSM PD.

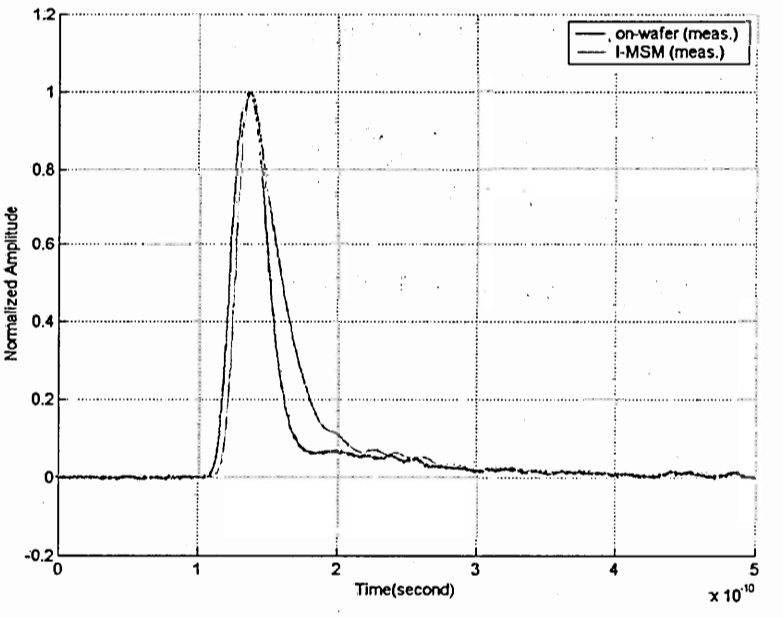

(a)

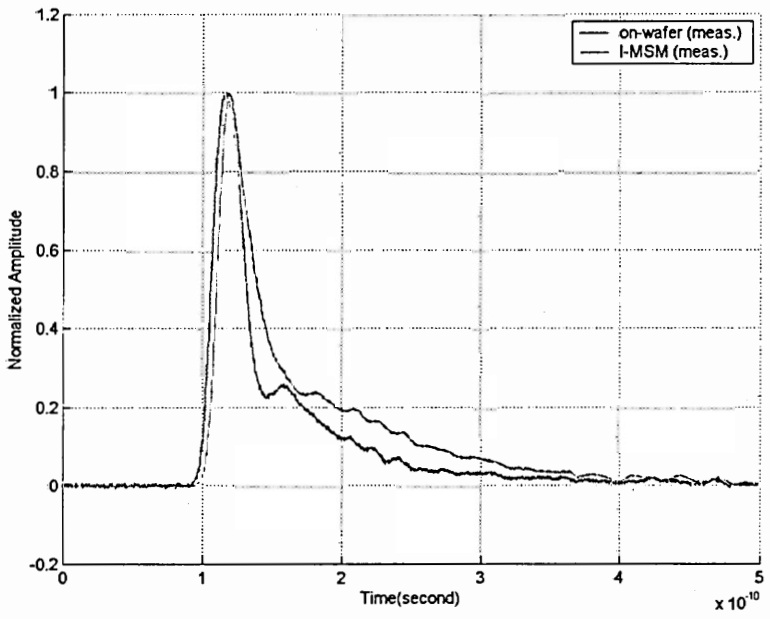

(b)

Figure 29: Impulse response of an I-MSM PDs in comparison to an on-wafer MSM PDs at a bias of 9 V with an 80 μm diameter size on material 219 with (a) of 1/1 μm finger width/spacing and (b) 2/2 μm finger width/spacing.

Figure 30 illustrates the difference of illumination on a unit cell for an on-wafer MSM PD and an I-MSM PD. The unit cell is defined as the center of the anode to the center of the cathode. The degradation of the impulse response for I-MSM PDs comes from two factors: (1) The photogenerated carriers have a higher density at Surface 1 (in both region I and region II shown in Figure 30) in the I-MSM PDs, so not only do the carriers have a longer transport path before collection, but the electric field is also weaker where the photogenerated concentration is the largest; (2) There are numerous carriers generated behind the electrodes (in region II) in I-MSM PDs. These carriers contribute to the improved responsivity of I-MSMs, but sacrifice the speed performance [49, 50]. The electric field in region II is weaker than in region I, leading to an incomplete depletion in

region II at low bias. In this case, carriers generated in region II have to diffuse into the high electrical field first, then accelerate to their saturation drift velocity. Once these carriers enter region I, they will travel following the same transit path as if they were originally generated in region I. Due the non-uniform electric field distribution in the absorbing layer, the curved equipotential contour determines whether the photogenerated carriers have to transit a curved path instead of straight path to reach the corresponding electrodes.

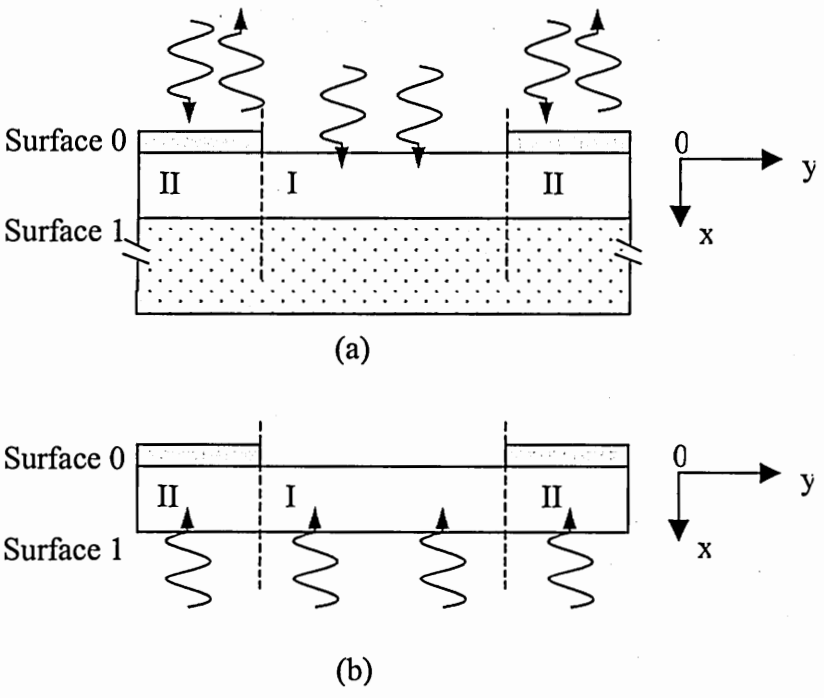

Figure 30: Diagram representing the illumination differences for (a) on-wafer MSM PDs and (b) I-MSM PDs.

Carriers generated in region I will be studied first for correlation. In this region, ignoring the space charge effect, the transit paths of carriers are the same for both I-MSM PDs and on-wafer MSM PDs if the carriers are generated at the same location inside the

absorbing layer. The space charge effect can be ignored here since it becomes significant only at higher dose of optical input power [51]. This assumption comes from the fact that the electric field distribution is very similar in the absorbing layer for both types of MSM PDs. In fact, the electric field is more tightly confined for I-MSM PDs than for on-wafer MSM PDs because some electrical energy may penetrate into the InP substrate for on-wafer MSM PDs. The absence of a substrate causes less electrical energy leakage into the air for I-MSM PDs. However, this difference for both types of MSM PDs is small since the electric field decreases quickly from the electrodes surfaces.

When the penetration depth is much less than the electrode spacing [52, 53], the curvature of the electric field lines between electrodes (in region I) is small enough so that the electric field can be approximated as constant laterally (along the y-axis shown in Figure 30), while the electric field changes dramatically in the longitudinal direction (along the x-axis shown in Figure 30). This situation is satisfied in this research since all materials in the study have absorbing layer thickness values much smaller than finger separation. The surface with the electrodes is assigned as the axis origin for both types of MSM PDs, as shown in Figure 30, and the expression for the carrier density in the absorbing layer for the on-wafer MSM PDs, $n_{omsm}(x)$, is:

$$n_{omsm}(x) = n_0 \exp(-\alpha x), \tag{6.15}$$

where n_0 is the carrier density at the illuminated surface (i.e. x = 0), and α is the absorption coefficient. The value of α is calculated from the extinction coefficient, κ, as discussed in Chapter 1:

$$\alpha = \frac{4\pi\kappa}{\lambda} = 0.002025/\text{nm} \tag{6.16}$$

The carrier density distribution for the back side illuminated I-MSM, $n_i(x)$, in the same coordinate system can be written as:

$$n_{imsm}(x) = n_0 \exp[-\alpha(T_x - x)], \tag{6.17}$$

where T_x is the absorbing layer thickness. If the absorbing layer is thin, there will be a substantial amount of optical power not absorbed in the first pass, and reflected by the semiconductor/air interface or the semiconductor/metal finger interface. Then the carrier distribution should include the first order absorption and the second order absorption. Higher orders of absorption are ignored for the calculation of the carrier distribution. In region I, the wave is reflected with a reflectivity of r_0, and in region II, the wave is reflected with a reflectivity of r_m. The modified carrier distribution is

$$\begin{cases} n_{imsm}(x) = n_0\left(e^{-\alpha(T_x-x)} + r_0 e^{-\alpha T_x} e^{-\alpha x}\right) & region \quad I \\ n_{imsm}(x) = n_0\left(e^{-\alpha(T_x-x)} + r_m e^{-\alpha T_x} e^{-\alpha x}\right) & region \quad II \end{cases} \tag{6.18}$$

It is obvious that the carriers generated closer to the x = 0 surface will be collected at an earlier time slot than carriers generated deep in the absorbing layer. The measured impulse response for an on-wafer MSM PD is an indication of the movement of the carriers in both the x and y directions. A particular electron or hole generated inside the absorbing layer of a PD will drift to the corresponding electrodes in a certain path no matter how it was created. Therefore, a carrier generated from back illumination will transit the same path as a carrier generated at the same location due to front illumination. The difference in the impulse response due to the two types of illumination purely comes from the different carrier density generated inside the absorbing layer. More carriers are generated closer to the collecting electrodes for on-wafer MSM PDs, leading to a faster collection of carriers. In other words, the impulse response will change only according to

the carrier distribution longitudinally (x-direction) inside the absorbing layer for uniform illumination across the active area. In this way, the calculation of the impulse response for I-MSM PDs from on-wafer MSM PDs becomes simply a 1D problem of solving the carrier density ratio in the x-direction since the carrier density gradient in the y-direction is the same for uniform illumination for both types of PDs. To carry on this methodology, first, the absorbing layer with thickness of T_x is divided into many sub-layers (x_0, x_1, x_2... x_n) along x-axis with

$$x_1 + x_2 + x_3 ... + x_n = T_x . \tag{6.19}$$

Also, we know that the impulse response pulse shape is determined by the number of carriers that were collected at the electrodes in each time slot on the time axis. Thus, the impulse response can be divided into many tiny small time slots (t_1, t_2, t_3...t_n). The sum of t_0 to t_n should equal to the time period of the impulse:

$$t1 + t2 + t3 + ... + tn = t_{imp} \tag{6.20}$$

where t_{imp} is the time period of the impulse response.

The carriers contributing to the impulse response at the first time slot, t_1, can be considered as generated from the absorbing sub-layer x_1, and the impulse at t_2 from InGaAs sub-layer x_2, and so on. So the impulse response in the time domain is related to the carrier distribution in the space domain. In region I, the carrier distribution of the I-MSM PDs can be compared to the distribution of the on-wafer MSM PDs as a ratio at each position along the x-direction:

$$ratio(x) = \frac{n_{imsm}(x)}{n_{omsm}(x)} = \frac{e^{-\alpha(T_x - x)} + r_0 e^{-\alpha T_x} e^{-\alpha x}}{e^{-\alpha x}} . \tag{6.21}$$

Figure 31 shows a plot for *ratio(x)* as a function of the depth inside the absorbing layer (3000Å in this case) in region I. If the impulse response is divided into same number of

sub-time slots as the number of sublayers in the absorbing layer, the ratio of the amplitude of the impulse response of the I-MSM to the on-wafer MSM will be the same as the photogenerated ratio. So the correlation of the amplitude of the impulse response (AMP) in the time domain is:

$$AMP\ of\ I\text{-}MSM\ (t_n) = AMP\ of\ On\text{-}Wafer\ MSM\ (t_n) \times ratio\ (t_x), \qquad (6.22)$$

where $ratio(t_x)$ is related to $ratio(x)$ with conversion coefficient 1. So the impulse response of the I-MSM PD can be calculated from the impulse response of the measured on-wafer MSM PDs with a multiplication of $ratio(t_x)$ as a function of time.

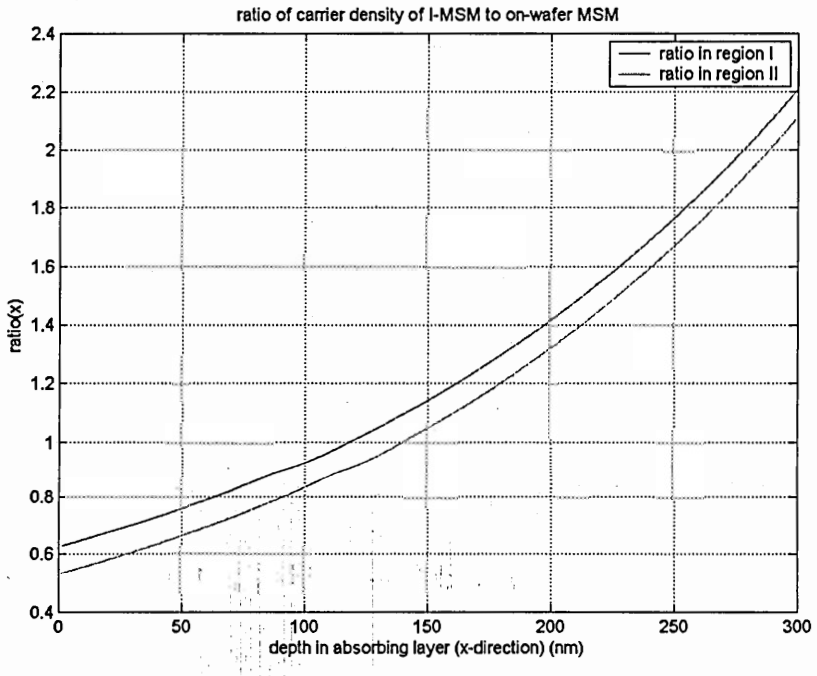

Figure 31: Ratio of carrier density for I-MSM to on-wafer MSM PDs as a function of absorbing layer depth.

The impulse response calculation for I-MSM PDs must also add the delay from carrier photogenerated in region II. For on-wafer MSM PDs, there are only a few carriers

generated in region II due to scattering under normal illumination. This is usually ignored. In this research, the correlation study is focused at high voltage bias for carrier transport the saturation velocity. For a thin absorbing layer (≤3000 Å) in region II, the electric field lines behind the electrodes are almost perpendicular to the surface [12], and this type of electric field contour forces the carriers generated in this region to have a large component of movement toward surface 1 (i.e. movement in the x-axis). Once the photogenerated carriers in region II enter the region I, they will be accelerated by the high electric field and drift in a similar manner as those carriers originally generated in region I. The bandwidth of the I-MSM is ultimately limited by the carriers having the longest transit length, which are holes generated right behind the positively charged electrodes (anodes). The longest transit path l_{long} of holes transported from region II to region I is calculated as

$$l_{long} = \sqrt{T_x^2 + (0.5w)^2} \tag{6.23}$$

where T_x is the thickness of the absorbing layer, and w is the finger width. Then, the longest delay time (transport time from region II to region I) for holes is calculated using the holes saturation velocity v_h:

$$t_d = \frac{l_{avg}}{v_h} = \frac{\sqrt{T_x^2 + (0.5w)^2}}{v_h} \tag{6.24}$$

where t_d is the delay time, and v_h is the hole saturation velocity. The calculated delay time for an I-MSM with 1 μm finger spacing on material 219 (3000 Å InGaAs) is

$$t_d = \frac{\sqrt{(0.3\mu m)^2 + (0.5\mu m)^2}}{4.8\times10^6 cm/\sec} = 12.5\times10^{-12}\sec = 12.5 ps. \tag{6.25}$$

Similarly, the delay time for devices of 2 μm finger spacing is calculated as 21.75ps.

The impulse response correlation calculation for I-MSM PDs from on-wafer MSM PDs was programmed using Matlab. The calculated results for PDs with 1/1 μm and 2/2 μm finger width/spacing are shown in Figure 32. The calculation reveals that the degradation of the impulse response of I-MSM PDs is dominantly caused from carriers generated in region II. The impulse response calculation in this work shows the I-MSM degradation trends clearly, which agrees with the qualitative analysis of the I-MSMs, as measured in Chapter 5.

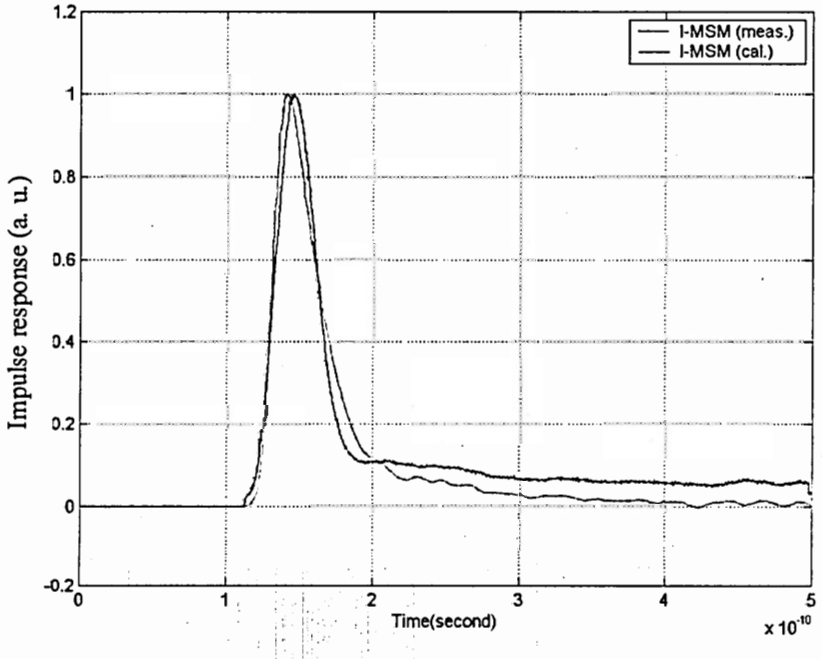

(a)

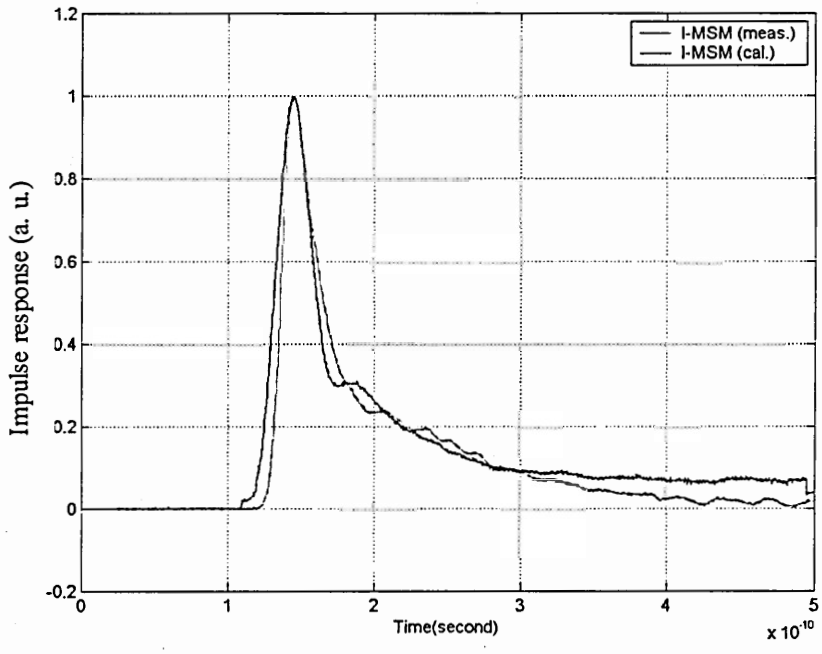

(b)

Figure 32: Impulse response correlation for I-MSM PDs to on-wafer MSM PDs with measured results and calculated results for PDs with 80 μm diameter absorbing area on material 219 (3000 Å InGaAs) with finger width/spacing of (a) 1/1 μm and (b) 2/2 μm.

6.2.2 Correlation of Capacitance

The MSM PD capacitance is determined by both the geometry and the dielectric constant of a material. The I-MSM PDs and on-wafer MSM PDs have been fabricated from the same material (InGaAs) growth, and the geometry of both types of PDs are similar. Therefore the capacitance is expected to be similar for both types of PDs. Table 25 lists a comparison of capacitance of on-wafer MSM PDs with I-MSM PDs. The average capacitance value difference of I-MSM PDs from on-wafer MSM PDs is 3.27%.

Table 25: The I-MSM capacitance in comparison to on-wafer MSM PDs.

Active area diameter/finger width/spacing	Capacitance of I-MSM PD (measured)	Capacitance of on-wafer MSM PD (measured)	Difference percentage
80/1/1 μm	199 fF	197.5 fF	0.7 %
80/2/2 μm	150 fF	160.5 fF	7%
60/1/1 μm	131.5 fF	130.3 fF	0.91%
40/1/1 μm	62.5 fF	59.7 fF	4.48%

In this Chapter, the correlation of I-MSM to on-wafer MSM PDs was analyzed for dark current, responsivity, impulse response, and capacitance. The measured dark currents of I-MSM PDs are slightly higher than the values of the on-wafer MSM PDs due to additional fabrication steps, but the trends follow the on-wafer MSM PDs. The responsivity correlation was derived in Section 6.1.2, and results reported in Equation (6.13) for thin absorbing layer MSM PDs and Equation (6.14) for thick absorbing layer MSM PDs. The prediction for I-MSM responsivity based upon the on-wafer MSM responsivity data has less than 10% error. The impulse response of the I-MSM PDs to the on-wafer MSM PDs was analyzed empirically, and results are plotted in Figure 32, which shows that the I-MSMs have a broader impulse response than the on-wafer MSMs. The capacitance correlation analysis in this Chapter shows that the capacitance of I-MSM PDs are close to the values measured for on-wafer MSM PDs. In conclusion, it is possible to predict the I-MSM characteristics from measured on-wafer MSM results.

CHAPTER 7

APPLICATIONS OF I-MSM PDS INTEGRATED ONTO PHOTORECEIVERS AND WAVEGUIDES

7.1 I-MSM PDs Integrated onto CMOS Chips.

I-MSM PDs, as one component of an integrated photoreceiver, have to meet certain system requirements. The most important requirements for this research are low capacitance, high bandwidth, and high responsivity. A circuit model for MSM PDs [54, 55, 56] is shown in Figure 33, where C_{msm} is the dark capacitance, C_{pads} is the capacitance induced by contact pads, and R_s and L_s are the series resistance and inductance, respectively.

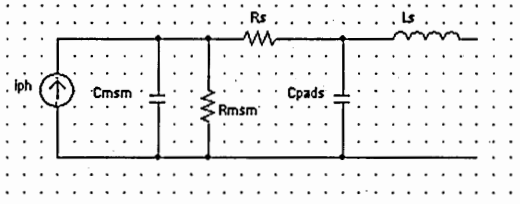

Figure 33: Equivalent circuit for a MSM PD under illumination.

The photoreceiver amplifier is, in general, not sensitive to the input components R_s, C_{pads}, and L_s of the I-MSM PDs, so they are eliminated from the photoreceiver block diagram shown in Figure 34. The I-MSM PD simplified as a capacitor (C_{msm}) connected in parallel with the amplifier, which is the input capacitance to the amplifier circuit. I_{ph} is the photocurrent generated by the MSM PD. After a photocurrent is generated, the current has to charge the C_{msm} first, which gives rise to a RC time delay to the amplifier.

The resistance of the MSM PD is usually in the range of kΩ. The circuit simulation starts with an assumption of input capacitance of 50 fF for the MSM PD, corresponding to a detector with a diameter of 50 μm. This capacitance is calculated using the conformal method outlined in Chapter 1.

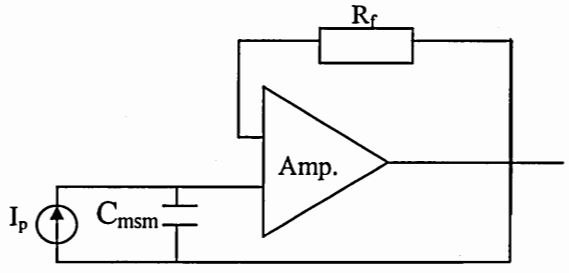

Figure 34: Block diagram of MSM PDs on photoreceiver circuits.

7.1.1 I-MSM PDs Fabrication and Integration.

The CMOS chips were designed by Prof. Martin Brooke's group and manufactured through the MOSIS foundry. The I-MSM PDs were fabricated following the process outlined in Chapter 2. The integration of I-MSM PDs onto Si CMOS integrated circuits includes the following steps:

1) Photolithography and metallization of the pad (with overglass cut) on the CMOS chips onto which the I-MSM PDs will be bonded.
2) Transferring I-MSM PDs onto the CMOS chips.
3) Spin-coating polyimide (PI2611) for adhesion enhancement.
4) Polyimide curing in an oven at 200°C for 1 hour.

5) Plasma etching using a Reactive Ion Etcher (RIE) to remove the polyimide with O_2.

The polyimide (PI2611) has a high poise viscosity of 110 ~ 135, which helps to adhere the I-MSM PDs to the bonding pads during spin-coating process. The majority of the polyimide coating was removed during the RIE process, but the small amount of polyimide residue "glues" the I-MSM PD very well to the chip.

7.1.2 I-MSM Integrated 400 Mbps CMOS Photoreceiver Chips.

I-MSM PDs have been integrated onto 400 Mbps photoreceiver chips, as shown in Figure 35. The I-MSM PD is 200 μm × 200 μm with 2 μm/2 μm finger width and gap. The MSM finger metallization is Ti (300 Å)/Pt (400 Å)/Au (2500 Å). The I-MSM PD was fabricated with Bandwidth® material, which exhibits a responsivity of 0.42 A/W at wavelength of 1.55μm. The speed of the photoreceiver is limited by the bandwidth of the circuitry.

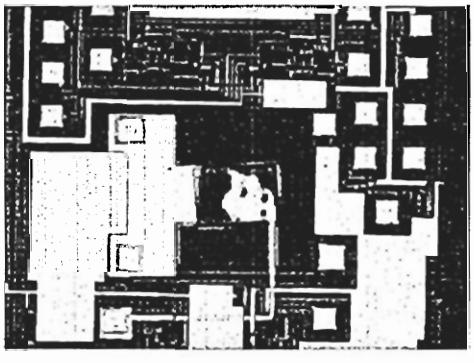

Figure 35: I-MSM PD integrated onto 400 Mbps photoreceiver.

The measured eye diagram at a signal rate of 400 Mbps is shown in Figure 36, which was tested in collaboration with Prof. Brooke's group.

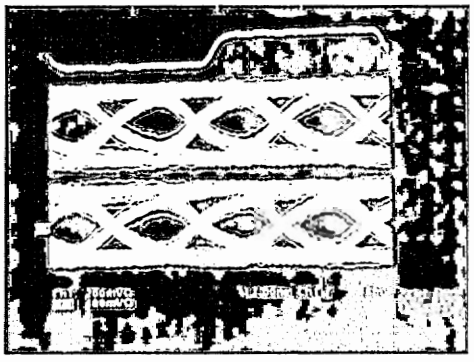

Figure 36: Eye pattern of integrated photoreceiver at a signal rate of 400 Mbps.

7.1.3 I-MSM Integrated onto 10 Gbps CMOS Photoreceiver Chips

I-MSM PDs with varied absorbing layer thickness and finger width/spacing have been integrated onto CMOS photoreceiver chips. In the first sample, an I-MSM circular PD with a 40 μm diameter and 2 μm/2 μm finger width/gap fabricated in material 217 (1000 Å InGaAs) was integrated. The capacitance of the detector was 44 fF with illumination. The electrodes of the I-MSM PD were Ti (300 Å) /Pt (400 Å)/Au (2500 Å). The metal via on the photoreceiver is Ti (300 Å)/Au (2500 Å). Figure 14 is a photomicrograph of the thin film I-MSM PD bonded to a 10 Gbps Si CMOS integrated circuit. The photocurrent and dark current of I-MSM PDs with the same structure were tested separately on probing pads, and this data is shown in Figure 38.

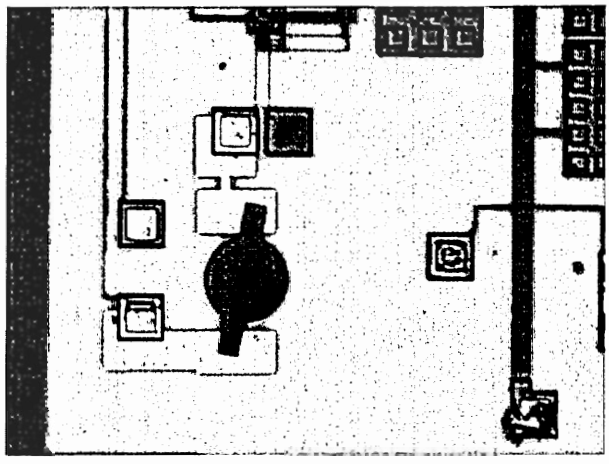

Figure 37: I-MSM PD integrated onto a 10 Gbps Si CMOS photoreceiver chip.

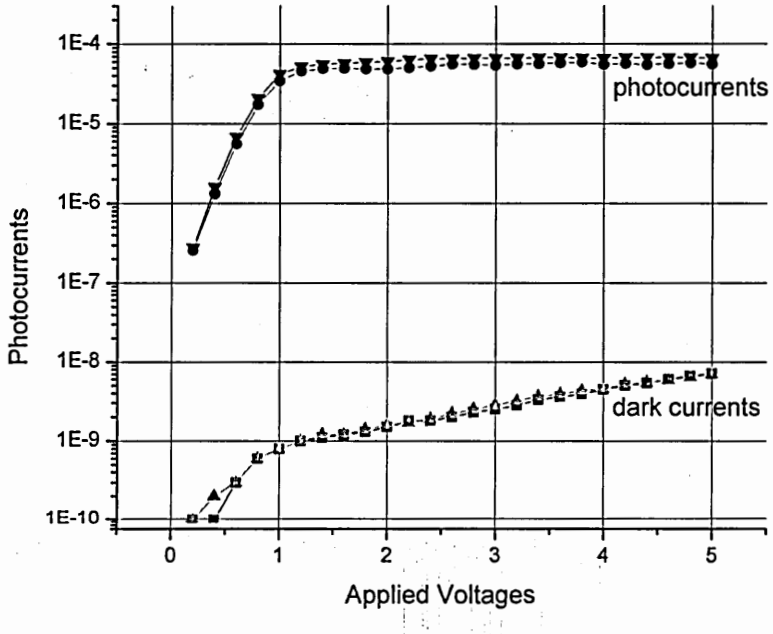

Figure 38: Dark currents and photocurrents of I-MSM PDs on probing pads.

The impulse response of the I-MSM PDs integrated onto a separate BCB coated Si/SiO_2 substrate (not the Si CMOS IC) with the same structure as that integrated onto the IC, was tested at a bias of 9 V. The impulse response is shown in Figure 39. The long tail indicates that the speed is limited by the transit time of the carriers in the PD. The

bandwidth of the photoreceiver with the integrated PD was tested successfully at 1.5 GHz. The bandwidth performance of the photoreceiver was limited by both the I-MSM PD and the circuit together.

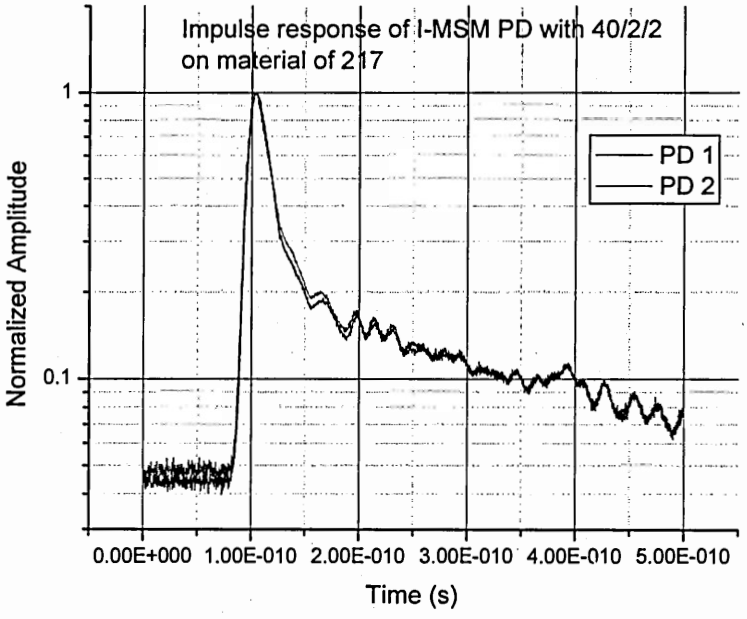

Figure 39: The impulse response of I-MSM PDs with the same structure as the PD on the CMOS photoreceiver chip.

The statistical modeling of on-wafer MSM PDs indicated that the bandwidth of the PDs is mainly limited by the finger spacing, and increasing the absorbing layer thickness from 1000 Å to 3000 Å has little effect. This was one of the results of the research in this thesis, presented in Chapter 5. Higher responsivity PDs are desirable because a larger input current to the receiver can, depending upon the receiver design, improve the speed and/or sensitivity of the OEIC. Thus, in the second integration, an I-MSM PD with a 3000 Å absorbing layer was chosen for higher responsivity. The size of the I-MSM PDs was kept at 40 μm to maintain a small input capacitance to the

differential amplifier. The finger width/spacing was designed with 1/1 μm to reduce the carrier transit time. The integrated photoreceiver with the I-MSM PD integrated onto the chip is shown in Figure 40.

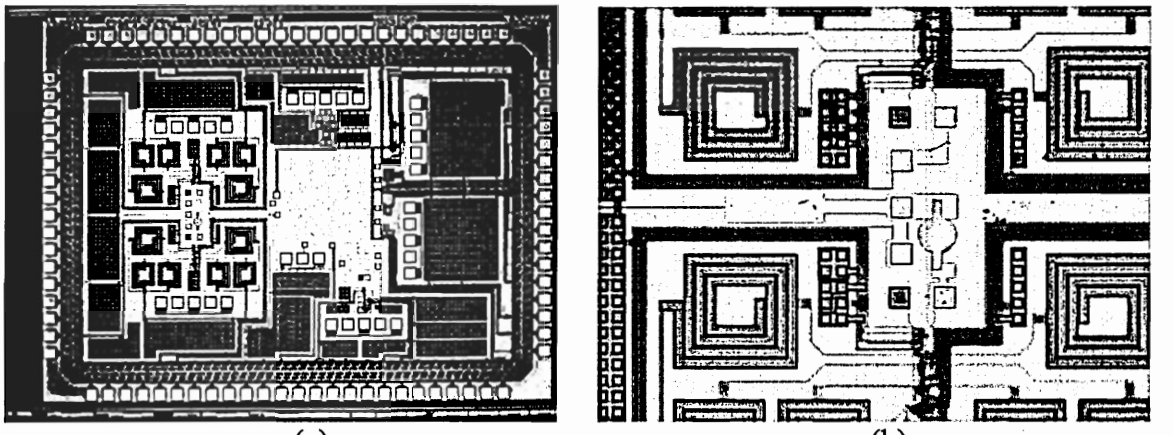

(a) (b)

Figure 40: (a) An I-MSM PD integrated onto the 10 GHz photoreceiver chip and (b) a detail picture of the I-MSM PD on the chip.

The electrodes of the I-MSM were Ti (300 Å)/Au (3000 Å) deposited using an e-beam evaporator. The metal via had a thickness of Ti (300 Å)/Au (3500 Å). The increased thickness of the via metal was designed to enhance the mechanical strength for multiple probing of the pads. The I-MSM PDs with the same structure were integrated onto a glass (SiO_2) substrate for separate measurements. The measured photocurrent and dark current are shown in Figure 41. The dark current is less than 10 nA at a bias of 5 V, and the responsivity is 0.1524 A/W at 1.55 μm wavelength illumination, which is much higher than the 0.08 A/W responsivity of the first integrated PD.

The AC performance of the I-MSM PDs on probing pads was also measured, and is shown in Figure 42. The average FWHM is 26.5 ps and tail length is 47.3 ps at a 9 V bias. The measured -3dB frequency using the HP LCA is 11.17 GHz.

The successful integration of InGaAs I-MSM PDs onto Si CMOS integrated circuits demonstrates that the I-MSM can be independently optimized and heterogeneously integrated onto Si CMOS circuitry. The large area, 200 μm × 200 μm I-MSM PD bonded to the 400 MHz Si CMOS chip and the 40 μm diameter PD bonded to the 10 GHz Si CMOS chip are large area detectors for the capacitance and speed that they exhibit, and thus offer alignment advantages for assembly packaging.

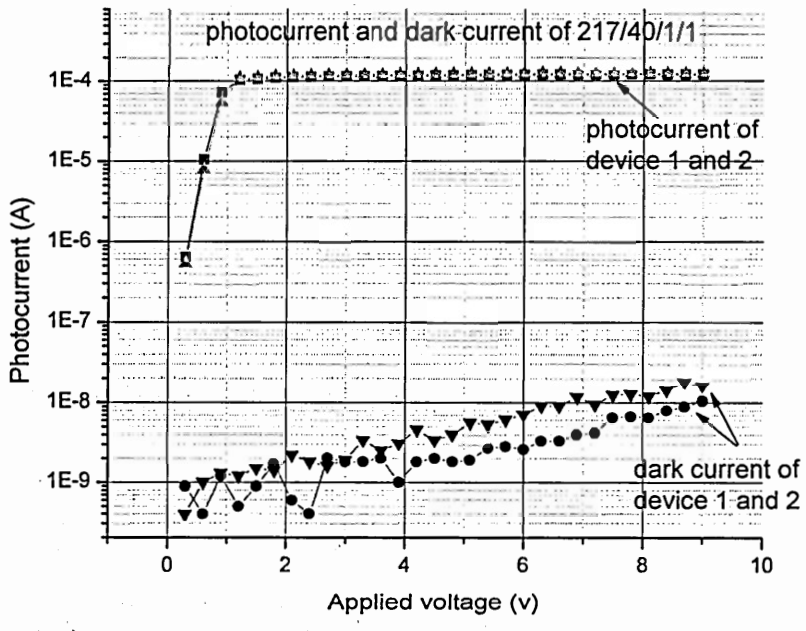

Figure 41: Photocurrents and dark currents of I-MSM PDs on probing pads with the same structure as the PD on the CMOS chip.

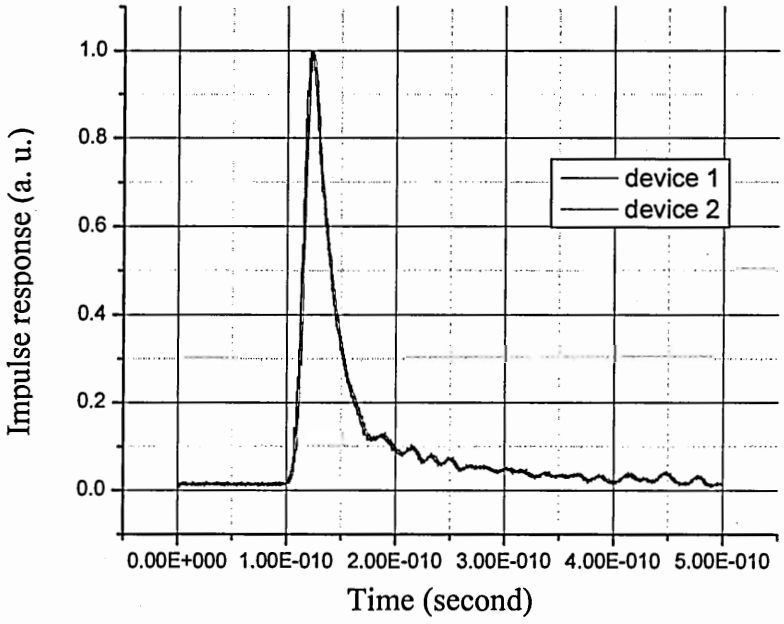

Figure 42: Impulse response of I-MSM PDs on probing pads with the same structure as the PD on the CMOS chip.

7.2 I-MSM Integrated onto Waveguides as Optical Interconnects.

MSM PDs embedded in polymer waveguides are a promising solution for chip to chip optical interconnections. Figure 43 shows a schematic diagram of this optical interconnection. A high speed optical signal is coupled into a waveguide, and the guided optical signals propagate along the core of the channel waveguide, and evanescently couple into the I-MSM PD embedded inside the cladding layer of the waveguide. The coupling efficiency is determined by the refractive index of the core and the cladding, the length of the MSM PD along the waveguide, the distance from core layer of the waveguide to the top of I-MSM, and the responsivity of the MSM PD. The bandwidth of this interconnection is primarily limited by the photodetector.

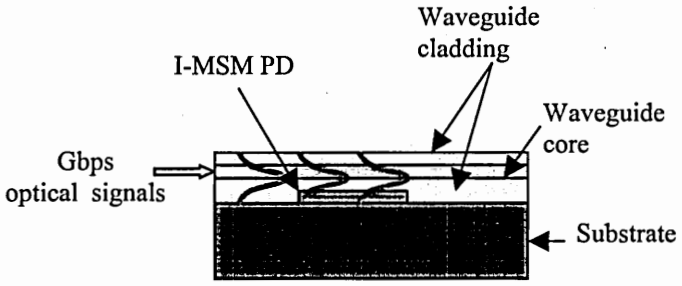

Figure 43: Schematic diagram of optical interconnect with I-MSM embedded in a waveguide.

To explore embedded PDs in waveguides, a collaborative project with Kyocera was undertaken. Georgia Tech integrated the thin film PDs onto Kyocera ceramic and Si/SiO2 substrates, and then Kyocera applied the waveguide and tested the samples. A thin film I-MSM PD can be transferred to a host substrate after it is independently fabricated and optimized. A thermal process (anneal) usually follows the device transferring and bonding to enhance the adhesion of the I-MSM PD to the host substrate. Different anneal temperatures after integration of the I-MSM PDs to the waveguide host substrate have been investigated. Results show that the adhesion can be significantly improved for a cure between 200 °C and 270 °C for 30 minutes or longer. The host substrates are prepared by Ti/Au or Cr/Au metal pads on either Si/SiO_2 or ceramic (Alumina: Al_2O_3) by Kyocera. Next, thin film I-MSMs were bonded to the pads, and then a thick siloxane (refractive index: 1.450) cladding material was spin-coated onto the substrate and cured in a N_2 flow environment by Kyocera. This undercladding layer was then etched back to approximately 1.5 μm thick, followed by a 7 um wide TiO_2-doped siloxane oligomer core (refractive index: 1.455) for the channel waveguide. Finally, a siloxane oligomer upper cladding was deposited on the top. The fabrication of this siloxane waveguide was carried out by Kyocera.

7.2.1 I-MSM PDs Embedded into Waveguides at 1G bps.

A 1 Gbps optical interconnection has been demonstrated and published in a paper as a result of this collaborative work. The MSM PDs had a size of 200 μm × 200 μm with finger width and spacing of 2 μm/2 μm, and was fabricated from Bandwidth material (InGaAs 7400Å). The metallization of the MSM PDs were Ti (300 Å)/Pt (400 Å)/Au (2500 Å), where Pt was a diffusion barrier layer for Au atoms in the later waveguide process (the high temperature (270 °C) curing of the polymers). Figure 44 shows a photomicrograph of the I-MSM PDs embedded in waveguides on ceramic and silicon substrates.

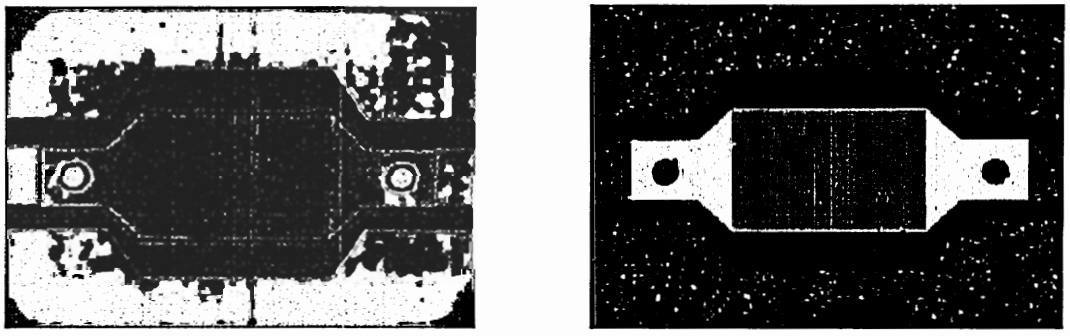

(a) (b)

Figure 44: Photos of I-MSM PDs embedded in waveguides on (a) ceramic and (b) silicon substrates.

Since MSMs are Schottky contact devices, they are sensitive to thermal processes such as those used to cure the waveguide into which the I-MSM was embedded. I-MSM PD dark current measurements are shown in Figure 45 for a bias from 0 to 5.2 V, which are conducted on I-MSMs that were annealed for 3 hours at 270 °C (the same as the

siloxane waveguide fabrication process). The dark current rises significantly after the first hour of anneal, with a continuous bake for another hour, the dark current decreases, and then rises again to 34.2 nA at 5 V after the third hour of anneal (for a 3 hour anneal). These results are consistent with I-MSM dark currents measured in embedded waveguides, which, for the same device runs for the data above, resulted in an embedded PD dark current of 42.8 nA. Although it has not been demonstrated in this research, the metallization for I-MSMs can be designed to produce lower dark current with another Pt layer deposited prior the Ti [57]. This additional Pt layer can stop the diffusion of Ti atoms into the semiconductor that will lower the Schottky barrier height. The Pt has a high melting temperature, and this leads to overheating of the photoresist during deposition in the e-beam evaporator, which degrades the photoresist for the lift-off process. Therefore, the first Pt layer is eliminated as a compromise to increase the process yield, but sacrifices the dark current. The photocurrents and dark currents during the annealing process are shown in Figure 45.

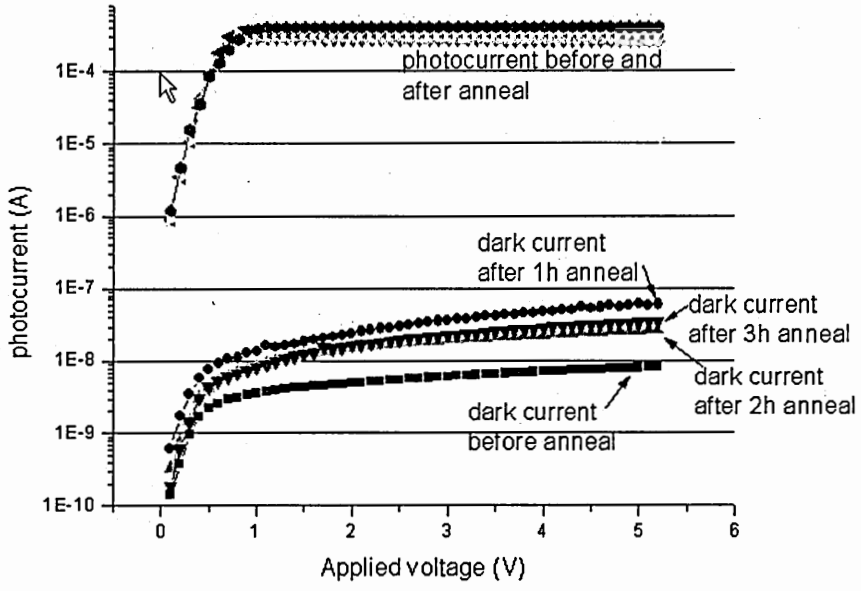

Figure 45: The dark currents and photocurrents as a function of anneal process for I-MSM PDs on a waveguide substrate.

The optical signal is evanescently coupled from the waveguide into the embedded PD. The refractive index of the siloxane waveguide core and cladding are 1.455 and 1.450, respectively. Using a 3D beam propagation (BPM) simulation, the coupling efficiency from the waveguide to the I-MSM is theoretically calculated to be 7%. The coupling efficiency has also been roughly estimated through measurement. To measure the coupling into the embedded I-MSM, a DFB laser at a wavelength of 1310 nm was coupled into a single mode fiber (core diameter 9.5 μm) and aligned to one end of the waveguide. The I-MSM photocurrent was monitored to optimize the fiber to waveguide endface alignment. When the mode was guided, a sharp photocurrent peak was observed, whereas side cladding modes had multiple soft peaks as the fiber was scanned across the waveguide endface. At 1 Gbps, the average input power from the fiber was 0.40 mW, producing 0.80 μA of output current from the I-MSM. The estimated coupling from the

fiber to the waveguide is 90%, however, the waveguide loss in this experiment was unusually (for this material) high, resulting in a total (coupling and propagation loss) of 8 dB from the fiber to the I-MSM. Thus, the incident optical power on the I-MSM was 64.6 μW. Using the 0.42 A/W I-MSM responsivity, and ignoring reflections, a worst-case estimate of the evanescent coupling efficiency is approximately 2.9%. The measurement of coupling efficiency was done by Kyocera. The optical interconnection is packaged on Si/SiO_2 and ceramic substrates, and both of them demonstrated signal transport rate at 1 Gbps. Figure 36 shows an eye pattern at 1 Gbps for PRBS 2^7-1 for an I-MSM waveguide embedded optical interconnection on ceramic and silicon substrates. The better bit error rate on ceramic substrate indicates that the substrates also limits the bandwidth as well as the I-MSM PDs.

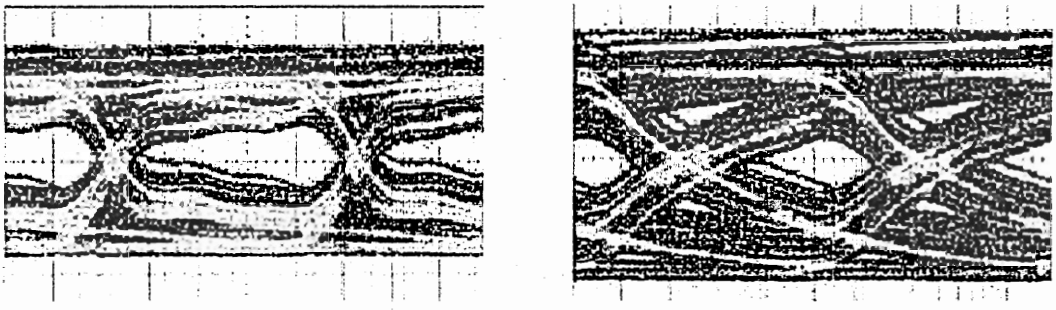

(a) (b)

Figure 46: Eye pattern of I-MSM PDs embedded in waveguides on: (a) ceramic and (b) silicon substrates at a PRBS of 2^7-1.

7.2.2 I-MSM PDs Embedded in Waveguides at 10G bps.

There are two concerns in optimizing I-MSM PDs for high bandwidth optical interconnections. First, the I-MSM PD has to have a small capacitance and fast carrier

transit time to achieve high bandwidth. Second, the I-MSM PD has to have sufficient responsivity and coupling area to have good coupling efficiency from the waveguide to the photodetector. The waveguide designed in this project is a channel waveguide with a 7 μm/7 μm cross sectional core area. In order to optimize for the best coupling efficiency, a rectangular MSM PD matched in width to the waveguide core was designed. To physically realize the transfer of I-MSMs to these host substrates, and to precisely define the waveguide channel on the top of the active area of the I-MSM, MSM PDs with a 20 μm width (finger length) were chosen. The coupling efficiency from the waveguide to the PD increases with the length of the overlapping area, and saturates at 40 μm to 50 μm [6]. Thus, a rectangular MSM PD was designed to have a length of 50 μm, which is much smaller than the length of 200 μm for the 1 Gbps optical links. To keep the parasitic capacitance low, contact pads for smaller I-MSM PDs were designed as shown in Figure 47 (a), in comparison to the large contact pads designed for the 1 Gbps links shown in Figure 47 (b). However, large contact area MSM PDs enhance the adhesion of the metal to metal bond for integration. The compromise between the adhesion and the bandwidth results in a design of two stubs on both sides of the I-MSM PD for the electrical contacts.

Besides the optimized shape designed for high bandwidth, the material thickness and finger width/spacing also affects the speed performance. From the DOE model and correlation analysis of I-MSM PDs in this thesis, it is clear that the finger spacing is the determining factor for multi gigahertz operation, whereas the absorbing layer thickness is not critical. An I-MSM PD with finger width and spacing of 1/1 μm and an absorbing layer of 2000 Å was fabricated for waveguide applications at 10 Gbps. The I-MSM PD

has an active area size of 20 μm × 50 μm, which gives a capacitance of 50 fF calculated with the conformal mapping technique.

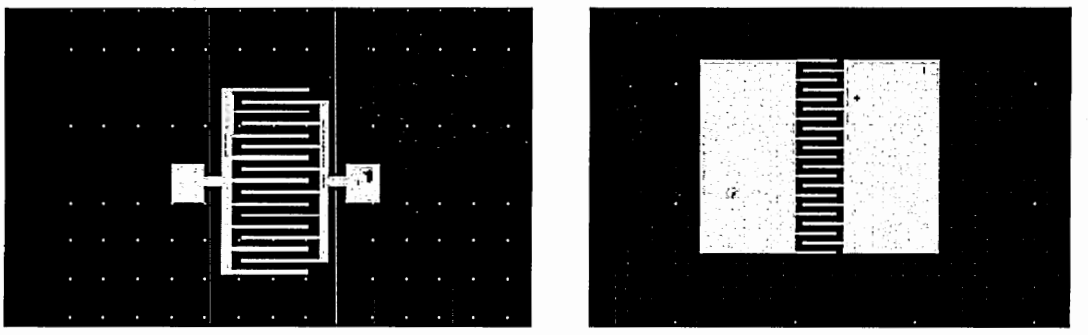

(a) (b)

Figure 47: (a) Reduced parasitic capacitance contact pads, in comparison with (b) previous designs, with larger contact pads.

The new integration for 10 Gbps optical links included a total of four I-MSM PDs bonded to ceramic substrates, and has shipped to Kyocera. Two of them were further adhesion enhanced with polyimide "glue" and another two were cured at 150 °C for half an hour for metal to metal bonding enhancement. A picture is shown for the rectangular MSM PD on a ceramic substrate in Figure 48. The photocurrents and dark currents of the I-MSM PDs bonded onto the ceramic substrates were measured, and are shown in Figure 49. The average dark current was 6.6 nA and the average responsivity at λ = 1.3 μm illumination was 0.13 A/W. The maximum dark current was 12.7 nA. These samples are currently in the waveguide fabrication process at Kyocera.

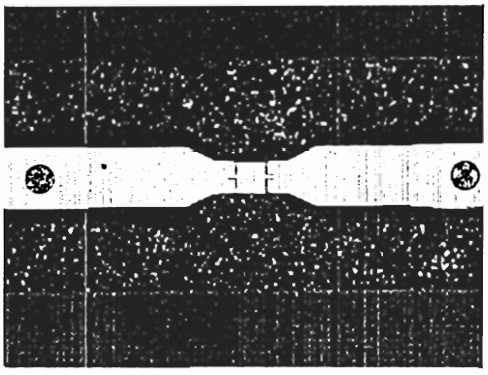

Figure 48: I-MSM PD bonded on ceramic substrate.

A separately fabricated InGaAs I-MSM PD was tested for comparison to the I-MSM PD embedded into the polymer waveguide, and showed no degradation between the embedded and separately tested I-MSM. The successful integration of I-MSM PD onto waveguide substrate, demonstrating GHz bandwidth, shows that the I-MSM PDs embedded into polymer waveguides is an effective way to realize high bandwidth planar optical interconnects. With optimized design, the optical interconnects of I-MSM embedded into waveguide will achieve multi gigahertz bandwidth, with good coupling efficiency, and high mechanical reliability.

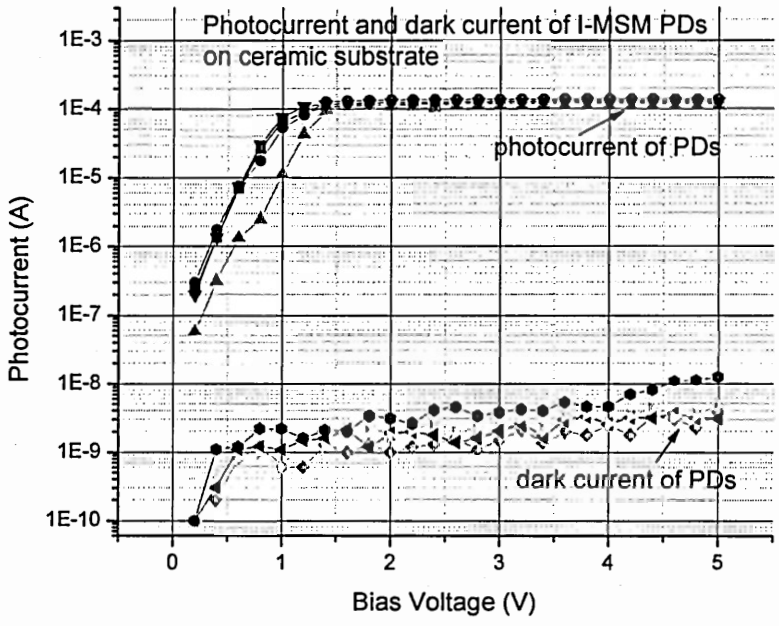

Figure 49: Photocurrents and dark currents of integrated I-MSM PDs onto ceramic substrates for 10 Gbps optical interconnections.

CHAPTER 8

CONCLUSIONS AND RECOMMENDATIONS

8.1 Conclusions

In this work, on-wafer MSM PDs arrays were fabricated and the dark current, responsivity, impulse response, bandwidth, and capacitance were studied. Photosensitive BCB was explored as a new isolation material that demonstrated excellent parasitic capacitance decoupling capability for metal to semiconductor probe pads, as well as excellent process compatibility with on-wafer MSMs. Numerous samples were fabricated and the responsivity, bandwidth, and capacitance were measured for DOE modeling. The responsivity of on-wafer MSM PDs is modeled as

$$\begin{aligned}\hat{R} = &-0.0174 - 0.02248 \times FW + 0.0227 \times F + 0.4269 \times MT \\ &+ (0.0146 \times FW - 0.022) \times (5 \times MT - 0.6667)\end{aligned}, \qquad (8.1)$$

with a prediction error of 10.35%. The bandwidth model for on-wafer MSM PDs is

$$\begin{aligned}\hat{BW} = &17.0247 - 0.0888 \times FW - 3.8063 \times FG - 0.0399 \times S \\ &-1.8906 \times MT + (0.15625 \times FG - 0.390625) \times (0.1S - 5) \\ &-(0.19125 \times FG - 0.478125) \times (5 \times MT - 0.6667)\end{aligned}, \qquad (8.2)$$

with a prediction error of 3.31%. The bandwidth model showed that the finger spacing is the most critical factor for determining the speed of the MSM PDs, while the active area size, material thickness, and finger width have minor effects. The capacitance of on-wafer MSM PDs is modeled as

$$\begin{aligned}\hat{cap} = &-7.425 + 7.5FW - 23.15FG - (0.25FW - 0.375)(FG - 5) \\ &+ (8.1FW - 12.15)(0.05S - 3) - (0.37S - 22.125)(2FG - 5)\end{aligned}, \qquad (8.3)$$

with a prediction error of 11.09%. The optimization of on-wafer MSM PDs can be realized with a thick absorbing layer for higher responsivity and 1 μm finger spacing for fast transit time using standard photolithography fabrication. The I-MSM PDs could also have large active areas for ease of alignment for applications where the PD capacitance is not important.

I-MSM PDs with various active area size and finger width/spacing on different materials were also fabricated and tested. The testing results were reported in Chapter 5. The measured results further confirm that the I-MSM PDs in this thesis are transit time limited, so the bandwidth increases with the increase of voltage bias and the reduction of finger spacing. Optimized bandwidth results were achieved at finger widths and spacings of 1/1 μm at biases over 7 V on material with 3000 Å and 5000 Å absorbing layer thicknesses. Although the size of the active area for the I-MSM PDs does play an important role in determining the capacitance, it is not a critical factor in determining the bandwidth.

The correlation of I-MSM PDs with on-wafer MSM PDs was also investigated in this work. As discussed in Chapter 6, the I-MSM PDs have moderate degradation in speed performance but significant enhancement of responsivity with complete elimination of finger shadowing to optical illumination.

Based on the MSM PD research, thin film I-MSM PDs were used in photoreceiver and waveguide optical link applications. The CMOS photoreceiver chips were design by Prof. Martin Brooke's group for bandwidth of 400 Mbps and 10 Gbps. The integration of I-MSM PDs onto the 400 Mbps photoreceiver resulted in a good eye diagram with the bandwidth limitation cause by the CMOS circuit. An I-MSM PD with

40 μm active area and 1/1 μm finger width/spacing fabricated on 3000 Å InGaAs absorbing material was also integrated onto a 10 Gbps photoreceiver chip. The same I-MSM PD separately integrated onto a glass substrate showed a measured responsivity of 0.1517 A/W and a bandwidth of 11.57 GHz.

Thin film I-MSM PDs were also integrated onto Si/SiO_2 and ceramic substrate for waveguide optical links. For a 1 GHz optical link, I-MSM PDs with a responsivity of 0.42 A/W were embedded in a waveguide and had a good eye opening with 2.9% coupling efficiency from the waveguide to the detector. To further improve the bandwidth of the optical link, the I-MSM PDs (optimized for bandwidth and coupling efficiency) were designed with a rectangular shape of 50 μm/20 μm and integrated onto ceramic substrates. These I-MSM PDs had an average dark current of 6.6 nA and responsivity of 0.13 A/W at wavelength of 1.3 μm. They are expected to have a bandwidth over 10 GHz. This is collaborative work with Kyocera, and the optical links with I-MSM PDs embedded in the waveguides are under evaluation at Kyocera now.

Thin film I-MSM PDs demonstrate high responsivity compared to conventional MSM PDs, with moderate degradation in bandwidth. The low capacitance per area makes them good candidates for integration onto alignment tolerant photoreceivers. The inverted MSM PDs embedded in waveguides offer a good architectural option for waveguide chip to chip optical links. In both the photoreceiver and waveguides applications, integrated InGaAs I-MSM PDs demonstrated multi gigahertz bandwidth operation.

8.2 Recommendations

In this work, the study of impulse response and bandwidth suggests that the finger spacing is the most dominant factor, whereas the material thickness and PD size are not critical factors. The 1 μm finger spacing devices, even on thicker material (5000 Å absorbing layer thickness), have much better performance than 2 μm finger spacing devices either fabricated from thin absorbing layer thickness material (1000 Å) or small detection area (20 μm diameter). My recommendation for future work therefore is to optimize the devices with thicker absorbing layer for higher responsivity. I expected that the transit time delay of carriers with absorbing layer thickness from 5000 Å to 1 μm with 1 μm finger width would be comparable with the time constant due to the capacitance of the PDs.

REFERENCES

1 "International Technology Roadmap for Semiconductors 1999 Edition," Semiconductor Industry Association (SIA), www.semichips.com, 1999.

2 M. Vrazel, Jae Joon Chang, In-Dal Song, KeeShik Chung; M. Brooke, N. M. Jokerst, A. Brown, D.S. Wills, "Highly alignment tolerant InGaAs inverted MSM photodetector heterogeneously integrated on a differential Si CMOS receiver operating at 1 Gbps", ECTC, 2001. Proceedings, 51st, pp 8 –13, 2001.

3 D.A.B. Miller, "Rationale and challenges for optical interconnects to electronic chips," Proceedings of the IEEE, Vol. 88, No. 6, pp 728-749, 2000.

4 C.L. Callender, L. Robitaille, J.P. Noad, F. Gouin, C.A. Almeida, "Optical signal distribution to MSM photodetector arrays via integrated polyimide waveguides", Journal of Lightwave Technology, Vol. 15, No. 9, pp. 1700 –1707, 1997.

5 R.T. Chen, L. Lin, C. Choi, Y.J. Liu, B. Bihari, L. Wu, S. Tang, R. Wickman, B. Picor, M. K. Hibb-Brenner, J. Bristow, Y.S. Liu, "Fully embedded board-level guided-wave optoelectronic interconnects," Proceedings of the IEEE, Vol. 88, No. 6, pp. 780 –793, 2000.

6 M. Siegert, M. Loken, C. Buchal, "Efficient optical coupling between a polymeric waveguide and an ultrafast silicon MSM photodiode" IEEE Journal of Selected Topics in Quantum Electronics, Vol. 4, No. 6, pp. 970-974, 1998.

7 Kevin F. Brennan, *The physics of semiconductors with applications to optoelectronic devices*, Cambridge University Press, 1999.

8 Hergo-Heinrich Wehmann, Guang-Ping Tang, Ralf Klockenbrink, and Andreas Schlachetzki, "Dark-current Analysis of InGaAs-MSM-Photodetectors on silicon substrates" IEEE Trans. on Elec. Devices. pp. 1505-1509, 1996.

9 S. Averine, Y.C. Chan, and Y.L. Lam, "Evaluation of Schottky contact parameters in metal-semiconductor-metal photodiode structures", Appl. Phys. Lett. Vol. 77, No.2, pp274-276, 2000.

10 Pallab Bhattacharya, *Properties of lattice-matched and strained indium Gallium arsenide,* Chapter 6, INSPEC, 1993.

11 Liann-Chern Liou, and Bahram Nabet, "Simple analytical model of bias dependence of the photocurrent of metal-semiconductor-metal photodetectors", Applied Optics, Vol. 35, No. 1, pp15-23, 1996.

12 Marian Hargis, Stephen Ralph, Jerry Woodall, and Dave Mclnturff, "Hole dominated transport in InGaAs metal semiconductor metal photodetectors", Appl. Phys. Lett. 67, pp 413-415, 1995.

13 S. Averin, R. Sachot, J. Hugi, M. Fays and M. Ilegems, "Time response analysis of GaInAs MSM photodiode structures", SPIE Vol. 2799, pp 414-412, 1995.

14 P. Hill, J. Schlafer, W. Powazinik, M. Urban, E. Elchen, and R. Olshansky, "Measurment of hole velocity in n-type InGaAs", Appl. Phys. Lett. 50(18), pp 1260-1262, May 1987.

15 S. Averin, R. Sachot, J. Hugi, M. Fays, and M. llegems, "Two-dimensional device modeling and analysis of GaInAs metal-semicondcutor-metal photodiode structures", J. Appl. Phys. 80, pp. 1553-1558, 1996.

16 Yu Chin Lim, and Robert Moore, "Properties of alternately charged coplanar parallel strips by comformal mappings", IEEE Trans. on Elec. Dev. Vol. ED-15, No. 3, pp. 173-180, 1968.

17 Stephen Chou, mark Liu, "Nanoscale tera-hertz metal-semiconductor-metal photodectors" IEEE J. of Quantum Elec. Vol.28. No. 10, Oct. 1992.

18 Z. Yu, S. Schablitsky, and S. Chou "Nanoscale GaAs metal-semiconductor-metal photodetectors fabricated using nanoimprint lithography" Appl. Phys. Lett. Vol.74, pp. 2381-2383, 1999.

19 Rong-heng Yuang, Jia-Lin Shieh, Jen-Inn Chyi, and Jyh-Shin Chen, "Overall performance improvement in GaAs MSM photodetectors by using recessed-cathode structure" IEEE Photo. Technol. Lett. Vol. 9, pp. 226-228, 1997.

20 L. F. Lester, K. C. Hwang, P. Ho, J. Mazurowski, J. M. Ballingall, John Sutliff, S. Gupta, J. Whitaker, and S. L. Williamson, "Ultrafast long-wavelength photodetectors fabricated on low-temperature InGaAs on GaAs" IEEE Photonic. Tech. Lett., Vol. 5, No. 5, 1993.

21 P. Kordos, A. Forster, M. Marso and F. Ruders, "550 GHz bandwidth photodetector on low-temperature grown molecular-beam epitaxial GaAs" Elec. Lett. Vol. 34, pp.119-120, 1998.

22 M. Klingenstein, J. Kuhl, R. Notzel, and K. Ploog, "Ultrafast metal-semiconductor-metal photodiodes fabricated on low-temperature GaAs" Appl. Phys. Lett. 60 (5), pp. 627-630, 1992.

23 M. Rao, S. Gulwadi, W-P. Hong, C. Caneau, G. K. Chang, and N. Papanicolaou, "Metal-semicondutor-metal photodetector using Fe-implanted In0.53Ga0.47As" Elec. Lett. Vol. 28 No.1, pp. 46-47, Jan. 1992.

24 E. H. Bottcher, E. Droge and D. Bimberg, "Ultrafast ion-implanted InGaAs metal-semiconductor-metal photodetectors" IEEE LEOS'97 1996.

25 W. A. Wohlmuth, "High-speed InGaAs metal-semiconductor-metal photodetectors with thin absorption layers" IEEE photonic. Tech. Lett. Vol. 9, 1997.

26 Shantanu Gupta, John Whitaker, and Gerard Mourou, "Ultrafast carrier dynamics in III-V semiconductors grown by molecular-beam epitaxy at very low substrate temperatures." IEEE. J. of Quan. Elec. Vol. 28, No. 10, pp. 2464-2472, 1992.

27 Jae Kim, H. Torsten Griem, Robert, Friedman, Eric Chan and Sankar Ray, "High-performance back-illuminated InGAAs/InAlAs MSM photodetector with a record responsivity of 0.96 A/W", IEEE Photo. Tech. Lett. Vol. 4, No. 11, pp1241-1243. 1992.

28 Olivier Vendier, Nan Jokerst, and Richard Leavitt, "Thin-film inverted MSM photodetectors", IEEE Photo. Tech. Lett. Vol. 8, pp. 266-268, 1996.

29 S. R. Schmidt and R. G. Launsby, *Understanding Industrial Designed Experiments*, 4th ed., Air Academy Press, Colorado Springs, CO, 1994.

30 D. Staiculescu, "Design rule development for microwave fillip-chip applications," IEEE transactions on microwave theory and techniques, VOL. 48, No. 9, Sept 2000.

31 M.F. Davis, R.J. Pratap, S. Pinel, U. Jalan, D.K. Kim, J. Laskar, G.S. May, "Design rule development for lectrical modeling of RF multiplayer packaging inductors", Electronic Components and Technology Conference, 2003. Proceedings. 53rd , May 27-30, Page(s): 1498 –1502, 2003.

32 Seogoo Lee, Jongseong Choi, Gary May, and Ilgu Yun, "Modeling and analysis of 3-D solenoid embedded inductors", IEEE Transactions on Electronics Packaging Manufacturing, Vol. 25, No.1, January 2002.

33 Patrick Zilaro, Paul Giotta, doug Hawks, Carlos macias, "Application of design of experiments methodology to model te effect of multiple parameters on simultaneous switching noise", Electronic components and Technology Conference, pp79-85, 2002.

34 J.S. Wang, C.C. Teng, J.R. Middleton, and M. Feng, "Process integration and optimization of GaAs MESFET and MSM based opto-electronics integrated circuit (OEIC) using statistical experimental design techniques", IEEE/CPMT Int'l electronics Manufacturing Technology Symposium, pp471-479, 1995.

35 Kathleen Virga and Robert Engelhardt, "Efficient statistical analysis of microwave circuit performance using design of experiments", Microwave Symposium Digest, IEEE MTT-S Int'l, pp123-126, vol.1, 2003.

36 J. H. Burroughes and M. Hargis, "1.3 μm InGaAs MSM photodetector with abrupt InGaAs/AlInAs interface", IEEE Photo. Tech. Lett. Vol. 3, No. 6, pp 532-534, 1991.

37 O. Wada, H. Nobuhara, H. Hamaguchi, T. Mikawa, A. Tacheuchi, and T. Fujii, "Very high speed GaInAs metal-semiconductor-metal photodiode incorporating an AlInAs/GaInAs graded super lattice", Appl. Phys, Lett., Vol. 54, pp. 16-17, 1989.

38 N. Matine, M. Dvorak, J. Pelouard, F. Pardo, and C. Bolognesi, "InP in HBTs by vertical and lateral wet etching", 10th Intern. Conf. On Indium Phosphide and Related Materials, pp. 11-15, 1998.

39 Aicha A. R. Elshabini-Riad and Fred D. Barlow III, *Thin Film Technologoy Handbook*, McGraw-Hill, Chapter 3, 1997.

40 Luc Martens, *High-Frequency Characterization of Electronic Packaging*, Kluwer Academic, 1998.

41 http://www.isixsigma.com

42 RS/Discover User's Guide, BBN Software Products, 1995.

43 D. V. Morgan, H. Ohno, C.E.C. Wood, W.J. Schaff, K. Board, L.F. Eastman, IEEE Proc. (USA) vol. 128, pp141-3, 1981.

44 S.R. Bahl, M.H. Leary, J. A. del Alamo, IEEE Trans. Electron Devices (USA), vol. 39, pp2034-2043, 1992.

45 J. E. Bowers and C. A. Burrus, "Ultra-wide-band long-wavelength PIN photodetectors," J. Lightwave Technol., vol. 5, pp. 1339-50, 1987.

46 Marian Hargis, Stephen Ralph, Jerry Woodall, Dave McInturff, Alfred Negri, and Paul Haugsjaa, "Temporal and spectral characteristics of back-illuminated InGaAs metal-semiconductor-metal photodetectors". IEEE Photo. Tech. Lett. Vol. 8, No.1, pp110-112, 1996.

47 M.A. Ordal, L. L. Long, R. J. Bell, S.E. Bell, R.R. Bell, R. W. Alexander and C.A. Ward, "Optical properties of the metals Al, Co, Cu, Au, Fe, Pb, Ni, Pd, Pt, Ag, Ti, and W in the infrared and far infrared." Applied Optics, vol. 22, No. 7, pp 1099-1119, 1983.

48 Chong-Long Ho, Wen-Jeng Ho, Meng-chiyi Wu and Jy-Wang Liaw, "Comparison of InGaAs pin photodiodes with Ti/Pt/Au and Au reflectors". Electronics Letters, Vol. 35, No. 20, pp 1767-1768, 1999.

49 Walter Wohlmuth, Mohamed Arafa, Patrick Fay, and Llesanmi Adesida, "InGaAs metal-semiconductor-metal photodetectors with a hybrid combination of transparent and opaque electodes", Appl. Phys. Lett. 70(22), pp3026-3028, June 1997.

50 Christian Beaulieu, Francois Gouin, Julian Noad, William Hartman, Eva Lisicka-Skrzek, Karen Vineberg and Ezio Berolo, "Design, fabrication and modeling of high-speed metal-semiconductor-metal (MSM) photodetectors with indium-tin-oxide (ITO) and Ti/PT/Au contacts", SPIE Vol. 2397, pp534-542, 1996.

51 Detlef Kuhl, Frank Hieronymi, E. Holger Bottcher, Torsten Wolf, dieter bimberg, Jurgen Kuhl, and Markus Klingenstein, "Influence of space charges on the impulse response of InGaAs metal-semiconductor-metal photodetectors", J. of Lightwave Tech. Vol. 10, No. 6, pp753-759, June 1992.

52 Jau-Wen Chen, Dae-Kaen Kim, and Mukunda, Das, "Transit-time limited high-frequency response characteristics of MSM photodetectors", IEEE Trans. on Elec. Devices, Vol. 43, No. 11, pp1838-1843, 1996.

53 Anthony W. Sarto and Bart J. Van Zegbroeck, "Photocurrents in a metal-semiconductor-metal photodetector", IEEE J. of Quan. Elec. Vol. 33, No. 12, pp 2188-2194, 1997.

54 Eiichi Sano, "A device model for metal-semiconductor-metal photodetectors and its applications to optoelectronic integrated circuit simulation", IEEE Trans. on Elec. Devices, Vol. 37, No. 9, pp 1964-1968, 1990.

55 D. Kuhl, F. Hieronymi, E. H. Bottcher, and D. Bimberg, "High-speed metal-semiconductor-metal photodetectors on InP:Fe", IEEE Photon. Tech. Lett. Vol. 2, No. 8, pp574-576, 1990.

56 Andrew Xiang, Walter Wohlmuth, Patrick Fay, Sung-Mo Kang and Ilesanmi Adesida, " Modeling of InGAAs MSM photodetector for circuit-level simulation", J. of Lightwave Tech. Vol. 14, No.5, pp716-723, 1996.

57 S.Y. Cho, N.M. Jokerst, "Embedded detector optical interconnections for board-level electronic interconnection substrates" Lasers and Electro-Optics Society 2002 Annual Meeting, Pages 161-162. . LEOS 2002.